© Copyright by Nikhil Walani 2015
All Rights Reserved

Mechanics of Cellular Transport

A Dissertation

Presented to

the Faculty of the Department of Mechanical Engineering

University of Houston

In Partial Fulfillment

of the Requirements for the Degree

Doctor of Philosophy

in Mechanical Engineering

by

Nikhil Walani

December 2015

Mechanics of Cellular Transport

Nikhil Walani

Approved:

Chair of the Committee
Ashutosh Agrawal, Assistant Professor,
Mechanical Engineering

Committee Members:

Yi-Chao Chen, Professor,
Mechanical Engineering

Kaspar Willam, Professor,
Civil and Environmental Engineering

Dong Liu, Associate Professor,
Mechanical Engineering

Gemunu Gunaratne, Professor,
Physics

Suresh K. Khator, Associate Dean,
Cullen College of Engineering

Pradeep Sharma, Department Chair,
Mechanical Engineering

Acknowledgements

This thesis is dedicated to my parents. Their love and support has allowed me to pursue science without having to worry about taking care of family duties. I am also highly indebted to my teachers who have instilled in me values to pursue my interests. In particular, I would like to thank Prof. Anurag Gupta and Prof. Durgesh C. Rai at IIT Kanpur, who motivated me towards mechanics.

I am thankful to my adviser, Prof. Ashutosh Agrawal, who has guided me throughout my stay here and introduced me to the wonderful world of biophysics. This thesis has immense contribution from him both in terms of time and substance. Needless to say that the shortcomings, if any, are because of me and I would try to improve on them. I am also grateful for his patience in allowing me to explore nuances of continuum mechanics which at times falls beyond the realm of my research on cellular biology. Through this, I gained a leverage which not other graduate students can have when their adviser is on a tenure track. I would further like to acknowledge the support of Prof. Yi-Chao Chen and for his courses on Finite Elasticity and Variational Methods in Mechanics. Also, for the numerous instances when he has guided and helped me with my research. Through the help of Prof. Gemunu Gunaratne, I have gained insights into critical phenomenon and phase transitions, and would cherish to use the theoretical framework to understand the behavior of lipid membranes. I would also like to thank Prof. Kaspar Willam and Prof. Dong Liu for reviewing my dissertation. Prof. Pradeep Sharma has been a great mentor and is always around to help the students. I thank him for constantly guiding me through the technical and non technical aspects of being a good researcher in today's academia.

I have been lucky to have friends here who have molded me not only as a researcher but also as a person. The list is so big that I cannot accommodate all

of them here. Special thanks to Vaibhav and Vikash for guiding me through various phases of my research. Discussions with them have always been insightful and thought provoking. From Dengke and Fatemeh, I have learned a lot about statistical physics of interfaces. I have relished the discussions with Qian Deng on micro-polar continuum, Cosserat surfaces and material symmetry aspects of modeling continuum bodies. I would also like to thank my lab mates Shengjie, Xin Yan, Xiao Bao, Yuranan, Shuyin, Himani, Mehdi, Ehsan, Dajla, Farah, Amit, Sana and Tarek for making my stay cherishable. Last but not the least, I would like to thank Ms. Laura Mora for providing me with a homely environment here in Houston.

Mechanics of Cellular Transport

An Abstract

of a

Dissertation

Presented to

the Faculty of the Department of Mechanical Engineering

University of Houston

In Partial Fulfillment

of the Requirements for the Degree

Doctor of Philosophy

in Mechanical Engineering

by

Nikhil Walani

December 2015

Abstract

Lipid membranes are versatile structures that interact with various kinds of proteins to maintain the shape and functionality of cells and their organelles. For example, they are actively involved in the transport of various proteins and other nutrients in and out of cells. The transport of macromolecules, which cannot diffuse through these bilayer membranes occur through an extensive remodeling of plasma membrane. This is executed by a designated set of membrane-deforming proteins, which supply the energy and drive membrane remodeling leading to formation of cargo-carrying vesicles.

In our study, we focus on the most commonly used transport pathway termed "Clathrin Mediated Endocytosis". We use continuum mechanics to study the equilibrium of lipid bilayers in the presence of three key membrane-deforming proteins, namely, clathrin, BAR and actin filaments.To the end, we generalize the theory of lipid membranes to incorporate the anisotropic curvatures generated by proteins. Our study reveals a protein-induced "Snap-through Instability" that offsets tension in the lipid membrane and drives vesicle growth. It disentangles the individual role of key proteins and provides mechanistic insights into fundamental debates in the field of cellular transport. Since these proteins (actin and BAR proteins) are involved in other interfacial rearrangements in cells, our work could provide new insights into biological processes in cells at-large. Motivated by the observed instability, we derive the generalized stability conditions for heterogeneous lipid membranes. These theories, in the future, can provide physical insights into the observed instability.

Table of Contents

List of Figures

List of Tables

Chapter 1 Introduction

1.1 Motivation

Evolution of life remains the biggest mystery since the beginning of scientific pursuit by humans. Although the information of life is coded and stored in nucleic acids, development and evolution of cells and organelles could not have proceeded with the essential role of cellular membranes. This is evident in the fact that the most primitive prokaryotic cells, bacteria and archaea have membranes enclosing the cytoplasm, and the more evolved eukaryotic cells have organelles and cells bounded by membranes (see Fig. 1.1).

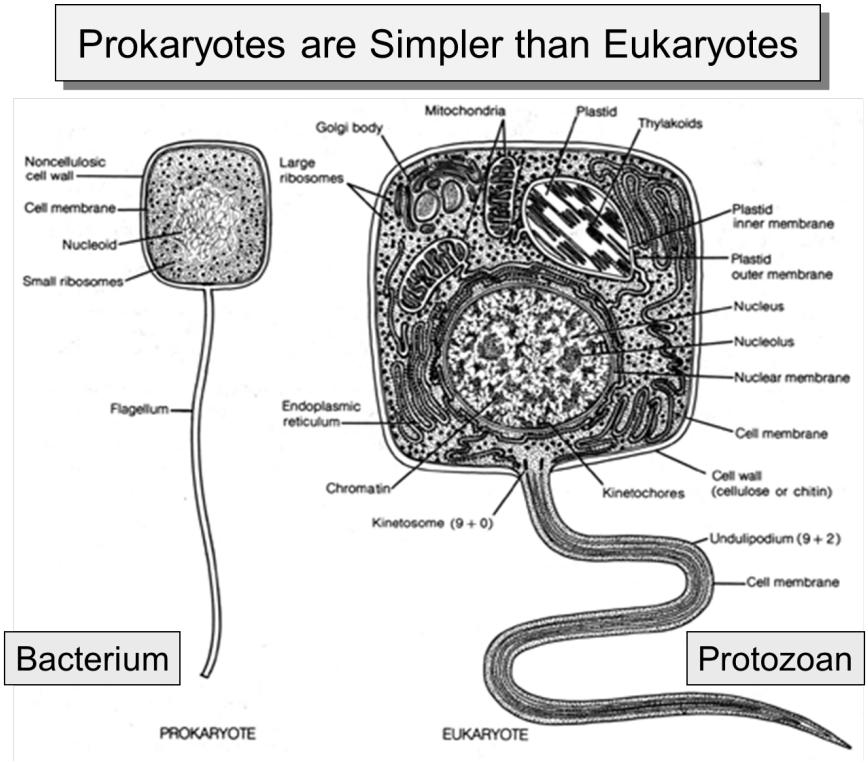

Figure 1.1: Schematic of a Prokaryote and a Protozoan, depicting how eukaryotic cells have evolved to compartmentalize various cellular functions through organelles bound by membranes. Figure obtained from [1].

Cellular membranes, bounding the organelles and the cells are made up of amphipathic molecules called lipids. In a typical biological cell, the membranes are composed of a wide variety of lipids and proteins.. Despite the heterogeneity, all these lipid molecules have a common structure, a polar head (hydrophilic) and non-polar (hydrophobic) core. Structure of a commonly observed phospholipid is shown in Fig. 1.2. As with other amphipathic molecules, these are arranged in various ways so as to shield their hydrophobic core from the polar solvent they are present in, depending on the concentration of these molecules with respect to the solvent. These lipids can arrange in unilamellar structures such as micelles or multiple layer stacked on top of each other such as in liposomes or lipid bilayers as shown in Fig. (1.3). These bilayers have a relatively small thickness of 3-5 nm and were only imaged after the successful usage of electron microscopes in the late 1950s.

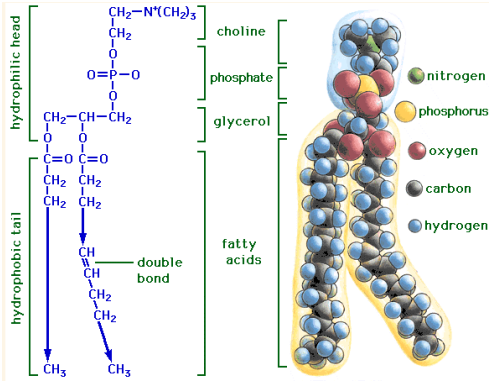

Figure 1.2: Structure of a typical phospholipid with polar choline and phosphate groups at the head fatty acyl chain in the tail. Obtained from website of D. Chynoweth, University of Florida.

One of the basic function of a cell is to regulate the synthesis and transport of proteins within the various organelles. Along with this, the cell controls the absorption and release of cargo, including proteins, oxygen, water molecules, charges (ferric, sodium, potassium, calcium, etc.) and other molecules so as to

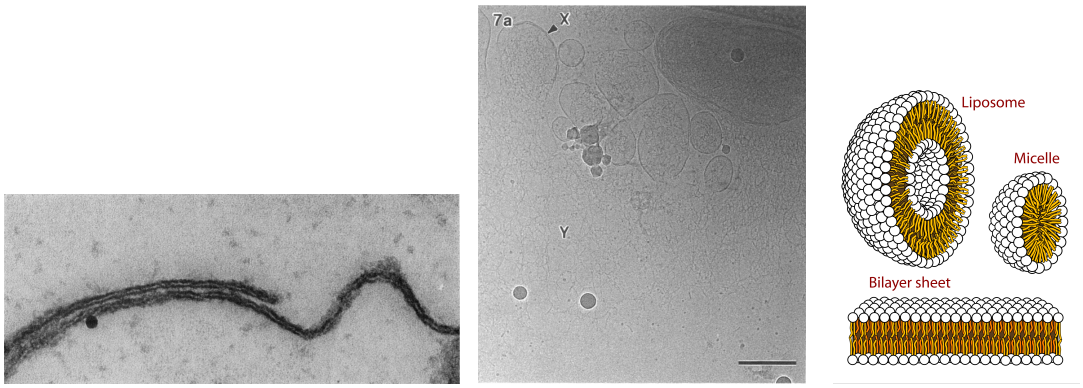

(a) (b) (c)

Figure 1.3: (a) Electron micrograph of lipid bilayer [2], (b) TEM of coexisting vesicles and micelles [3] (c) Schematic of Liposomes, Micelles and Sheets (source: Wikipedia)

maintain the concentration gradient of various molecules across the cell ([4, 5]). Transport of these molecules through the cell and other organelles, invariably, has to occur through the lipid membrane.

While some of the molecules like oxygen are small enough to diffuse through the bilayer and transport of charges such as sodium, potassium and calcium occurs via transmembrane proteins (ion channels) embedded in the lipid bilayer, bigger molecules like ferric charges bound to proteins called transferrin, low density lipoprotein (LDL) or the proteins synthesized in the Endoplasmic Reticulum of the cell, to name a few, cannot penetrate the lipid bilayer. Their transport is achieved through extreme remodeling of the lipid bilayer, which leads to the formation of a bud, and ends up in a cargo-carrying vesicle that detaches from the parent lipid bilayer that delivers cargo inside the cytoplasm , as shown in Fig. 1.4. This process is called endocytosis. A reverse process, called exocytosis, involves fusion of vesicles with the cell membrane and is used to deliver cargo out of the cells.

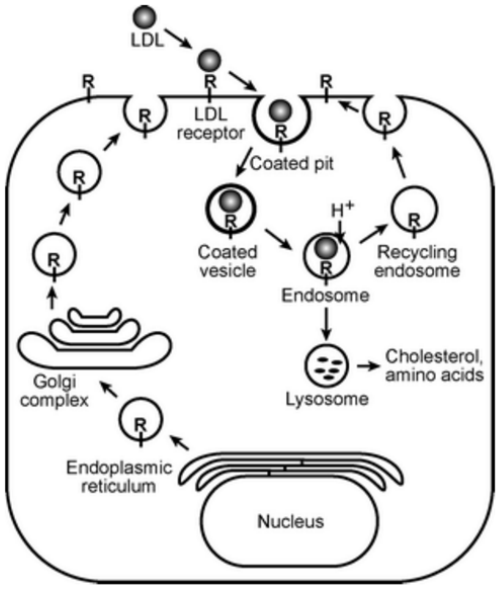

Figure 1.4: Schematic for endocytic and exocytic pathways inside a typical mammalian cell, 'R' is used to represent the receptor. [6]

1.2 Clathrin Mediated Endocytosis (CME)

The focus of the current study is on gaining mechanistic insights into endocytosis. Endocytosis, itself can be of various types namely, Clathrin Mediated Endocytosis (CME), Caveoli, Macropinocytosis or the Phagocytosis. This classification is based on the type of cargo transported and the type of proteins involved during transport (Fig. 1.5). CME remains the most widely observed pathway with clathrin as the key protein involved in driving the invagination from an almost lipid bilayer to a detached vesicle. In mammalian cells, clathrin trimers attach from the cytoplasmic side and generate spherical vesicles with diameters ranging from 70 nm to 350 nm. In contrast, in yeast cells, proteins form tubular invaginations which eventually turn into elliptical vesicles with their longest axes around 50 nm in length [7].

CME involves collaborative efforts of more than 60 proteins at a particular endocytic site. Moreover, most of the key proteins are conserved or have homo-

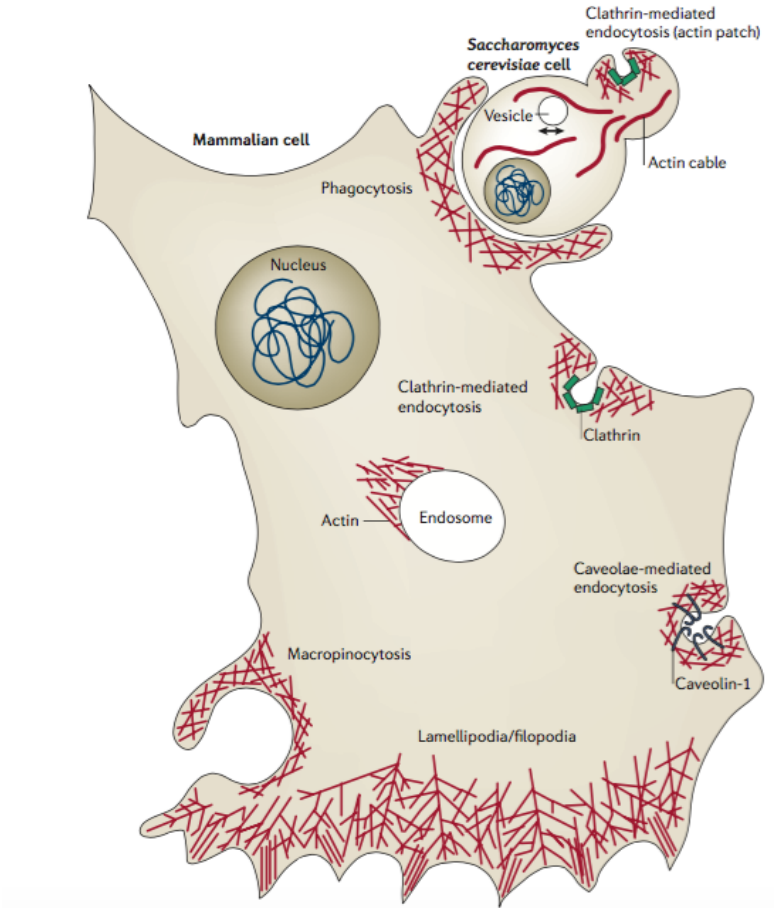

Figure 1.5: Schematic of various endocytic pathways in a mammalian cell which is phagocytosing a budding yeast cell, S.Cerevisiae. Figure obtained from [8]

logues across all the eukaryotes, thus it is expected that the basic roles of these proteins are also conserved across various species. Since the genomic structure of yeast is fully mapped and homologous proteins are involved in mammalian CME, studies concerning the roles of proteins in yeast CME are used to gain insights into mammalian CME. To study the role or function of a specific protein involved, cells are genetically mutated so that the concerned protein is knocked out. Furthermore, colored fluorescence microscopy is used to measure the concentration and involvement of each protein at a particular stage of CME. Sections of cells with endocytic site are viewed under electron microscope to view the lipid

membrane profile. Correlation between the fluorescence microscopy and the electron microscopy yields the temporal and the spatial insights into the role of each labelled protein.

CME can be broadly classified into the following four stages:

- Site selection
- Binding of cargo to the receptor on the surface lipid bilayer and that of receptor to the clathrin coat.
- Budding and maturation of the endocytic vesicle attached to the parent lipid bilayer via a neck.
- Pinching off of the matured vesicle by proteins responsible for scission.

In the initial stages, proteins like ubiquitin binding protein (Ede1p in yeast or Epsin, Eps15 in mammalian cells) are suspected to break the symmetry of the bilayer by wedge like insertions which initiates the formation of small buds allowing the other membrane remodeling proteins such as clathrin to bind on [9]. Thereafter, binding of cargo to the receptors on the extracellular side,, triggers the assembly of clathrin and adapter proteins (APs) from the cytoplasmic side of the lipid bilayer. Clathrin coat (comprising of clathrin, adapter proteins and other coat molecules) in mammalian cells deforms the lipid bilayer to reach the maturation stage as its concentration at the endocytic cite increases. In contrast, the bilayer remains almost flat in yeast cells even when the clathrin coat has completely adhered to the lipid bilayer (Fig 1.6). This difference is attributed to the difference in the tension in the lipid bilayer for the two species. This was proved by Ayscough and coworkers in a seminal study [10]. The study revealed that the addition of sorbitol, which lowers the pressure across the cell membrane and hence lowers the surface tension, allows the clathrin coat to form partial vesicles.

In a recent study, Kirchchausen and coworkers showed that clathrin coat is unable to form mature vesicles in mammalian cells when subjected to increased tension either via external stretching or osmotic shock [11].

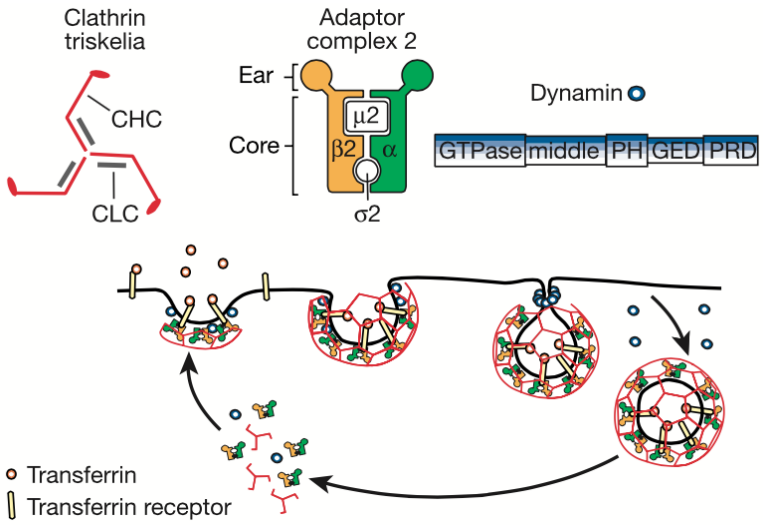

(a)

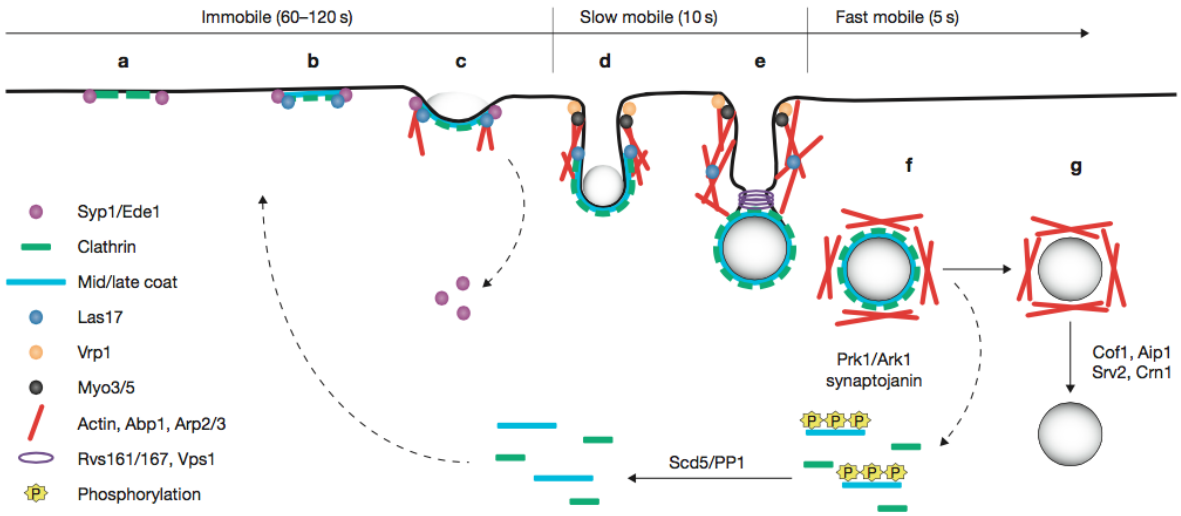

(b)

Figure 1.6: Schematics of endocytosis in (a) mammalian cells [12] , (b) yeast cells [13]. Clathrin coat along with adapter proteins is able to form the vesicle in mammalian cells but unable to do the same in yeast cells.

The estimates of membrane tension in mammalian cells range from $(0.01 -$

0.1) mN/m. The high end of this range is achieved for polarized cells where parts of plasma membrane are stretched. In yeast cells, tension in the lipid membrane is estimated to be greater than 0.5 mN/m. But cells are robust entities that adapt to various environments to ensure uninterrupted transport. For overcoming the inability of clathrin coat, actin filaments polymerize at the endocytic cite and drive invagination. Actin involvement in stretched mammalian cells and yeast endocytosis has been well established by experimental studies ([11, 14]).

After the vesicle has matured and is attached to the parent lipid bilayer via a neck, specific scission proteins work with actin to pinch off the vesicle. In mammalian cells, dynamin polymerizes in a helical manner and squeezes the neck to induce fission [15]. In yeast cells, scission is believed to require a collaborative effort of actin, rod shaped BAR proteins (Rvs 161/167) and dynamin-like protein Vps1.

There have been various attempts to classify the roles of individual proteins for yeast studies. Since disruption of actin does not even lead to budding, it's role in scission events cannot be directly predicted. However, mutant studies of BAR proteins have been used to determine the role of actin in scission. BAR mutant studies have shown vesicle formation as well as stalling of invaginated vesicles midway in equal proportions [16]. Only recently, Briggs and coworkers have used cryogenic tomography studies to reveal that in BAR mutant cells, shallow vesicles form but they undergo an unexpected rapid transition to form detached vesicles. Their inability to observe the intermediate stage raises important questions about the shape transition pathway during CME as a vesicle with a constricted neck is required to have non-leaky transport.

This forms the basis of our study as we try to combine these experimental findings from mammalian and yeast cells to shed light on mechanics of CME. In the subsequent chapters we have tried to elucidate the mechanical role of the

three key proteins - clathrin coat, BAR and actin filaments in countering tension in the lipid bilayer to form vesicles during CME. We have not explicitly modeled the scission but have tried to give insights into it based on the in-plane stresses with the bilayer. We have used continuum mechanics and modeled lipid bilayer as a two-dimensional surface embedded in 3 dimensional Euclidean space. This is because lipid bilayer is only 3-5 nm thick and endocytosis involves simulating the remodeling of lipid bilayer patch of more than 16000 nm^2 of lipid bilayer for a duration of around 2 minutes, a computationally expensive task for molecular dynamics.

A brief outline of the following chapters is as follows. In the second chapter we will expand on the differential geometry and the mechanics of lipid membranes. The following chapter deals with proposing a mechanical model for mechanics of lipid membranes interacting with orthotropic rod like BAR proteins. The fourth chapter will aim at bridging the gap between clathrin mediated endocytosis in mammalian and yeast cells. The mathematical models developed would be put to use to explain the differences in the roles of clathrin coat, BAR and actin filaments and how they are coupled to the tension in the lipid membrane. The fifth chapter deals with the stability of lipid bilayer membranes and is followed by conclusion and scope of improvement.

Chapter 2 Differential Geometry of Surfaces and Mechanics of Lipid Membranes

For the subsequent analysis in this document, we will assume that a two molecule thick membrane can be considered as thin enough to be represented by a surface. The natural choice for this surface is the mid-surface, i.e., the interface between two monolayers. Following the principle of continuum mechanics, which is based on the assumption that each material point represents a large collection of atoms, we assume that each material point on the surface of a lipid bilayer represents a large number of atoms. At physiological temperatures bilayers are fluidic in nature and the in-plane motion of the lipid molecules entails no energetic cost. The principles of liquid crystal theory can be used to penalize the relative mis-orientations of lipid molecules to define the strain energy for a bilayer. Such a surface can also be considered as a fluid Cosserat shell. [17, 18, 19]. A general theory of lipid bilayers can be developed based on the following simplifying assumptions

- Lipid molecules are always aligned with the surface normal because of the packing constraints.
- Director ($\mathbf{d}$) at each point is represented by joining the heads of lipid molecules from bottom monolayer to the top monolayer.
- The thickness of the lipid bilayer is constant.
- Area of the lipid membrane is assumed to be constant. This is based on the experiments which reveal that lipid membranes cannot stretch by more than

2-3% [20].

These assumptions allow a Cosserat shell to be considered as a Kirchoff Love Shell, whose equivalence has been proved under the assumptions that the director field is aligned with the surface normal and is inextensible [21]. Further, it is assumed that the lipid bilayer is a hyper-elastic material. This means that there exists a scalar potential that represents the energy stored in the lipid bilayer, which is dependent only on its current state and not the history of deformed states that led to the current state. We now review the differential geometry of surfaces that is needed to describe the energy and the equilibrium conditions of a bilayer.

2.1 Differential Geometry of Surfaces

The surface is considered to be a two dimensional Riemannian manifold embedded in a 3 dimensional Euclidean space. Let (θ^1, θ^2) be the parameters describing the surface. Subsequently we will represent the parameter space by (θ^α). Here and henceforth, Greek indices represent values $\{1,2\}$ and Einstein's indicial notation is used. This means that any index, if repeated twice, has to be summed over the possible values in its set. The notations for symbols used in the text are mentioned in Table 2.1.

Let the position of each material point on the surface be given by the map from the parameter space $\mathbf{r}(\theta^\alpha)$. The tangent vectors for such a parameterization are given by

$$\mathbf{a}_\alpha = \mathbf{r}_{,\alpha}. \tag{2.1}$$

Above and henceforth, subscripted comma is used to denote the derivative with respect to parameterizing variables θ^α. This map is associated with a metric at each point on the surface, whose components are given by,

$$a_{\alpha\beta} = \mathbf{a}_\alpha \cdot \mathbf{a}_\beta. \tag{2.2}$$

We note here that the components of metric are symmetric.

Further, the vectors in the cotangent space to the surface are chosen such that they map the tangent vectors to the real space and

$$\mathbf{a}^{\alpha} \cdot \mathbf{a}_{\beta} = \delta^{\alpha}_{\beta}. \tag{2.3}$$

Here, δ represents the Kronecker's delta function. Thus, using vectors in cotangent space, we get the metric which is inverse to the metric obtained from vectors in the tangent space and its components are given by,

$$a^{\alpha\beta} = \mathbf{a}^{\alpha} \cdot \mathbf{a}^{\beta}. \tag{2.4}$$

The normal to the surface at any material point is given by,

$$\mathbf{n} = \frac{1}{2}\varepsilon^{\alpha\beta}\mathbf{a}_{\alpha} \times \mathbf{a}_{\beta}, \tag{2.5}$$

where, $\varepsilon^{\alpha\beta} = e^{\alpha\beta}/\sqrt{a}$ with $e^{\alpha\beta}$ representing the permutation tensor such that $e^{11} = e^{22} = 0$, $e^{12} = -e^{21} = 1$ and a = det($a_{\alpha\beta}$). Similarly, $\varepsilon_{\alpha\beta} = e_{\alpha\beta}\sqrt{a}$ and $e_{\alpha\beta} = e^{\alpha\beta}$.

For doing calculus on the surface, we need to define the derivatives on the surface. For any given scalar field $\phi(\theta^{\alpha})$ defined on the surface, the change in ϕ along any curve in the surface is

$$d\phi = (\nabla\phi) \cdot d\mathbf{r} = \phi_{,\alpha} d\theta^{\alpha}, \quad \text{where} \quad d\mathbf{r} = \mathbf{a}_{\gamma} d\theta^{\gamma}. \tag{2.6}$$

Thus, the gradient of scalar field ϕ is

$$\nabla\phi = \phi_{,\alpha}\mathbf{a}^{\alpha}. \tag{2.7}$$

Similarly, change in a vectorial field $\mathbf{v}(\theta^{\alpha})$, defined on the surface along a particular curve is

$$d\mathbf{v} = (\nabla\mathbf{v})d\mathbf{r} = \mathbf{v}_{,\gamma} d\theta^{\gamma}. \tag{2.8}$$

Thus, gradient of a vector field, $\mathbf{v}(\theta^\alpha)$, defined on the surface is

$$\nabla \mathbf{v} = \mathbf{v}_{,\beta} \otimes \mathbf{a}^\beta. \tag{2.9}$$

Here and henceforth, $\otimes$ is used to represent the tensor product. Since tangent vectors $\mathbf{a}_\alpha$ and $\mathbf{n}$ form a basis that spans the 3 dimensional Euclidean space, we can write,

$$\mathbf{v} = (\mathbf{v} \cdot \mathbf{a}^\alpha)\mathbf{a}_\alpha + (\mathbf{v} \cdot \mathbf{n})\mathbf{n} = v^\alpha \mathbf{a}_\alpha + v\mathbf{n}. \tag{2.10}$$

Using the above equation and substituting it in (2.9), we obtain

$$\nabla \mathbf{v} = \left\{ v^\alpha_{,\beta} \mathbf{a}_\alpha + v^\alpha \mathbf{a}_{\alpha,\beta} + v_{,\beta}\mathbf{n} + v\mathbf{n}_{,\beta} \right\} \otimes \mathbf{a}^\beta. \tag{2.11}$$

Directional derivative of the tangent vector can be written as

$$\mathbf{a}_{\alpha,\beta} = (\mathbf{a}_{\alpha,\beta} \cdot \mathbf{a}^\gamma)\mathbf{a}_\gamma + (\mathbf{a}_{\alpha,\beta} \cdot \mathbf{n})\mathbf{n} = \Gamma^\gamma_{\alpha\beta}\mathbf{a}_\gamma + b_{\alpha\beta}\mathbf{n}, \tag{2.12}$$

where,

$$\Gamma^\gamma_{\alpha\beta} = \mathbf{a}^\gamma \cdot \mathbf{a}_{\alpha,\beta} \text{ and } b_{\alpha\beta} = \mathbf{a}_{\alpha,\beta} \cdot \mathbf{n}. \tag{2.13}$$

$\Gamma^\gamma_{\alpha\beta}$ represent the Christoffel symbols and $b_{\alpha\beta}$ are the components of the second fundamental form. To evaluate $\mathbf{n}_{,\beta}$, we note that

$$\begin{aligned} &\mathbf{n} \cdot \mathbf{n} = 1, \text{ thus} \\ &\mathbf{n}_{,\beta} \cdot \mathbf{n} = 0. \end{aligned} \tag{2.14}$$

This means that $\mathbf{n}_{,\beta}$ lies in the tangent plane at any given material point and that it can be written as

$$\mathbf{n}_{,\beta} = (\mathbf{n}_{,\beta} \cdot \mathbf{a}^\alpha)\mathbf{a}_\alpha = -(\mathbf{n} \cdot \mathbf{a}^\alpha_{,\beta})\mathbf{a}_\alpha \qquad \because (\mathbf{n} \cdot \mathbf{a}_\alpha = 0). \tag{2.15}$$

These yield the equations of Weingarten, where,

$$\mathbf{n}_{,\beta} = -b^\alpha_\beta \mathbf{a}_\alpha. \tag{2.16}$$

Using (2.12) and (2.16), we can rewrite (2.11) as

$$\begin{aligned}\nabla \mathbf{v} &= (v^{\alpha}_{,\beta} + v^{\lambda}\Gamma^{\alpha}_{\lambda\beta} - vb^{\alpha}_{\beta})\mathbf{a}_{\alpha} \otimes \mathbf{a}^{\beta} + (v_{,\beta} + v^{\alpha}b_{\alpha\beta})\mathbf{n} \otimes \mathbf{a}^{\beta} \\ &= (v^{\alpha}_{;\beta} - vb^{\alpha}_{\beta})\mathbf{a}_{\alpha} \otimes \mathbf{a}^{\beta} + (v_{,\beta} + v^{\alpha}b_{\alpha\beta})\mathbf{n} \otimes \mathbf{a}^{\beta}.\end{aligned} \tag{2.17}$$

Here we note that the subscripted semi colon $()_{;\alpha}$ is used to denote the covariant derivative of the quantity within parenthesis, i.e., the derivative with respect to the metric $a_{\alpha\beta}$. Thus, $a_{\alpha\beta;\gamma} = 0$. For a scalar field the covariant derivative is same as the directional derivative. Covariant derivatives of a co-vector is given by,

$$v_{\alpha;\beta} = v_{\alpha,\beta} - v_{\lambda}\Gamma^{\lambda}_{\alpha\beta}, \tag{2.18}$$

a covariant second order tensor is given by,

$$A_{\alpha\gamma;\beta} = A_{\alpha\gamma,\beta} - A_{\alpha\lambda}\Gamma^{\lambda}_{\gamma\beta} - A_{\lambda\gamma}\Gamma^{\lambda}_{\alpha\beta}, \tag{2.19}$$

and a contravariant second order tensor is given by

$$A^{\alpha\gamma}_{;\beta} = A^{\alpha\gamma}_{,\beta} + A^{\alpha\lambda}\Gamma^{\gamma}_{\lambda\beta} + A^{\lambda\gamma}\Gamma^{\alpha}_{\lambda\beta}. \tag{2.20}$$

Further, the surface Laplacian of a scalar $\phi(\theta^{\alpha})$ on the surface is given by

$$\Delta\phi = \mathrm{tr}(\nabla\nabla\phi) = \mathrm{tr}([\phi_{,\alpha\beta} - \phi_{,\gamma}\Gamma^{\gamma}_{\alpha\beta}]\mathbf{a}^{\alpha} \otimes \mathbf{a}^{\beta}). \tag{2.21}$$

Since, $\phi_{;\alpha\beta} = (\phi_{,\alpha})_{;\beta}$, we obtain that

$$\Delta\phi = \phi_{;\alpha\beta}a^{\alpha\beta}. \tag{2.22}$$

Surface divergence of the vector field $\mathbf{v}$ defined on the surface can be written as (using (2.17))

$$\nabla \cdot \mathbf{v} = \mathrm{tr}(\nabla\mathbf{v}) = v^{\alpha}_{;\alpha} - vb^{\alpha}_{\alpha}. \tag{2.23}$$

Curvature tensor ($\mathbf{b}$) at any material point is defined as the negative of surface gradient of the normal. Thus,

$$\mathbf{b} = -\mathbf{n}_{,\alpha} \otimes \mathbf{a}^{\alpha}, \tag{2.24}$$

which can be written using second fundamental form as,

$$\mathbf{b} = b_{\alpha\beta}\mathbf{a}^{\alpha} \otimes \mathbf{a}^{\beta}. \tag{2.25}$$

Similar to the metric tensor, components of the second fundamental form are symmetric. The invariants of the curvature tensor are mean (H) and Gaussian curvature (K) defined as

$$H = \frac{1}{2}\text{tr } \mathbf{b} = \frac{1}{2}b_{\alpha\beta}a^{\alpha\beta} \qquad K = \det \mathbf{b} = \frac{1}{2}\varepsilon^{\alpha\gamma}\varepsilon^{\beta\lambda}b_{\alpha\beta}b_{\gamma\lambda}. \tag{2.26}$$

2.1.1 Compatibility Conditions

We note that,

$$\mathbf{r}_{,\alpha\beta} = \mathbf{a}_{\alpha,\beta} = \Gamma^{\gamma}_{\alpha\beta}\mathbf{a}_{\gamma} + b_{\alpha\beta}\mathbf{n}. \tag{2.27}$$

From equation (2.27) we note that we cannot choose $a_{\alpha\beta}$ and $b_{\alpha\beta}$ arbitrarily at each point on the surface as there are 9 equations with 6 variables (3 each for $a_{\alpha\beta}$ and $b_{\alpha\beta}$). Thus, the components of metric tensor and curvature tensor have to satisfy certain compatibility constraints. The compatibility constraints arise from the fact that,

$$\mathbf{n}_{,\alpha\beta} = \mathbf{n}_{,\beta\alpha}. \tag{2.28}$$

Using the (2.16), we obtain,

$$\begin{aligned}\mathbf{n}_{,\alpha\beta} &= -(b_{\alpha\gamma}\mathbf{a}^{\gamma})_{,\beta} = -(b_{\alpha\gamma,\beta}\mathbf{a}^{\gamma} + b_{\alpha\gamma}(\mathbf{a}^{\gamma}_{,\beta}\cdot\mathbf{a}_{\lambda})\mathbf{a}^{\lambda}) - b_{\alpha\gamma}(\mathbf{a}^{\gamma}_{,\beta}\cdot\mathbf{n})\mathbf{n} \\ &= -(b_{\alpha\gamma,\beta} - b_{\alpha\lambda}\Gamma^{\lambda}_{\gamma\beta})\mathbf{a}^{\gamma} - b_{\alpha\gamma}b^{\gamma}_{\beta}\mathbf{n},\end{aligned} \tag{2.29}$$

and that,

$$\mathbf{n}_{,\beta\alpha} = -(b_{\beta\gamma,\alpha} - b_{\beta\lambda}\Gamma^{\lambda}_{\gamma\alpha})\mathbf{a}^{\gamma} - b_{\beta\gamma}b^{\gamma}_{\alpha}\mathbf{n}. \tag{2.30}$$

From (2.28), (2.29) and (2.30) and equating components along $\mathbf{a}^{\gamma}$, we obtain

$$b_{\alpha\gamma,\beta} - b_{\alpha\lambda}\Gamma^{\lambda}_{\gamma\beta} = b_{\beta\gamma,\alpha} - b_{\beta\lambda}\Gamma^{\lambda}_{\gamma\alpha}. \tag{2.31}$$

Subtracting $b_{\lambda\gamma}\Gamma^{\lambda}_{\alpha\beta}$ from both sides in above equation, we obtain

$$\begin{aligned} &b_{\alpha\gamma,\beta} - b_{\alpha\lambda}\Gamma^{\lambda}_{\gamma\beta} - b_{\lambda\gamma}\Gamma^{\lambda}_{\alpha\beta} = b_{\beta\gamma,\alpha} - b_{\lambda\gamma}\Gamma^{\lambda}_{\alpha\beta} - b_{\beta\lambda}\Gamma^{\lambda}_{\gamma\alpha}, \text{ hence,} \\ &b_{\alpha\gamma;\beta} = b_{\beta\gamma;\beta}. \end{aligned} \tag{2.32}$$

These are called the Mainardi-Codazzi equations. Further equating the components along the normal direction, obtained from (2.29) and (2.30), we get

$$b_{\alpha\gamma}b^{\gamma}_{\beta} = b_{\beta\gamma}b^{\gamma}_{\alpha}. \tag{2.33}$$

Along with (2.28), compatibility conditions also require that

$$\mathbf{a}_{\alpha,\beta\gamma} = \mathbf{a}_{\alpha,\gamma\beta}, \tag{2.34}$$

where,

$$\begin{aligned} \mathbf{a}_{\alpha,\beta\gamma} &= (\Gamma^{\lambda}_{\alpha\beta}\mathbf{a}_{\lambda} + b_{\alpha\beta}\mathbf{n})_{,\gamma} \\ &= (\Gamma^{\lambda}_{\alpha\beta,\gamma} + \Gamma^{\lambda}_{\mu\gamma}\Gamma^{\mu}_{\alpha\beta})\mathbf{a}_{\lambda} + (b_{\alpha\beta,\gamma} + \Gamma^{\lambda}_{\alpha\beta}b_{\lambda\gamma})\mathbf{n} - b_{\alpha\beta}b^{\lambda}_{\gamma}\mathbf{a}_{\lambda}. \end{aligned} \tag{2.35}$$

Using similar operations as above, we obtain

$$\mathbf{a}_{\alpha,\gamma\beta} = (\Gamma^{\lambda}_{\alpha\gamma,\beta} + \Gamma^{\lambda}_{\mu\beta}\Gamma^{\mu}_{\alpha\gamma})\mathbf{a}_{\lambda} + (b_{\alpha\gamma,\beta} + \Gamma^{\lambda}_{\alpha\gamma}b_{\lambda\beta})\mathbf{n} - b_{\alpha\gamma}b^{\lambda}_{\beta}\mathbf{a}_{\lambda}. \tag{2.36}$$

Equating coefficients of $\mathbf{a}_{\lambda}$ in (2.35) and (2.36), we obtain

$$R^{\lambda}_{\alpha\beta\gamma} = b_{\alpha\gamma}b^{\lambda}_{\beta} - b_{\alpha\beta}b^{\lambda}_{\gamma}, \tag{2.37}$$

where,

$$R^{\lambda}_{\alpha\beta\gamma} = \Gamma^{\lambda}_{\alpha\gamma,\beta} - \Gamma^{\lambda}_{\alpha\beta,\gamma} + \Gamma^{\lambda}_{\mu\beta}\Gamma^{\mu}_{\alpha\gamma} - \Gamma^{\lambda}_{\mu\gamma}\Gamma^{\mu}_{\alpha\beta} \tag{2.38}$$

is the Riemann tensor. By equating the normal components of (2.35) and (2.36), we recover the Mainardi-Codazzi equations. Riemann tensor can be used to write

$$\begin{aligned} R^{\lambda}_{\alpha\beta\gamma} &= a^{\lambda\eta}(a_{\beta\mu}a_{\gamma\lambda} - a_{\beta\lambda}a_{\gamma\mu})b^{\lambda}_{\alpha}b^{\mu}_{\eta} \\ &= a^{\lambda\eta}\varepsilon_{\beta\gamma}\varepsilon_{\mu\lambda}b^{\lambda}_{\alpha}b^{\mu}_{\eta} \\ &= a^{\lambda\eta}K\varepsilon_{\eta\alpha}\varepsilon_{\beta\gamma}. \end{aligned} \tag{2.39}$$

Hence, the Gaussian curvature 'K' can be completely described by the metric tensor $a_{\alpha\beta}$. The above equation is called as 'Theorem Egregium' and states that the Gaussian curvature cannot be changed without changing the components of the metric tensor, i.e., straining the surface.

The contravariant adjugate of $b_{\alpha\beta}$ can be written as

$$\tilde{b}^{\alpha\beta} = (a^{\alpha\beta}a^{\lambda\gamma} - a^{\alpha\gamma}a^{\lambda\beta})b_{\lambda\gamma} = \varepsilon^{\alpha\lambda}\varepsilon^{\beta\gamma}b_{\lambda\gamma}. \tag{2.40}$$

Thus, $K = \tilde{b}^{\alpha\beta}b_{\alpha\beta}$. This can be used to write the Cayley-Hamilton theorem in the form

$$\tilde{b}^{\alpha\beta} = 2Ha^{\alpha\beta} - b^{\alpha\beta}. \tag{2.41}$$

2.1.2 Green-Stoke's Theorem

Another useful entity that we will use in the remaining chapters is the Green - Stokes Theorem, which states that for a surface ω bounded by the curve $\partial\omega$ and vector field $\mathbf{v}(\theta^\alpha)$,

$$\int_\omega (\nabla \times \mathbf{v}) \cdot \mathbf{n}\, da = \int_{\partial\omega} \mathbf{v} \cdot d\mathbf{r}. \tag{2.42}$$

Curl of a vector field $\mathbf{v} = v_\gamma \mathbf{a}^\gamma + v\mathbf{n}$ on a surface is,

$$\nabla \times \mathbf{v} = \mathbf{a}^\alpha \times \mathbf{v}_{,\alpha} = \mathbf{a}^\alpha \times [(v_{\gamma;\alpha} - vb_{\gamma\alpha})\mathbf{a}^\gamma + (v_{,\alpha} + v_\gamma b^\gamma_\alpha)\mathbf{n}]. \tag{2.43}$$

Thus, the component along normal direction of the curl of vector field is,

$$(\nabla \times \mathbf{v}) \cdot \mathbf{n} = \mathbf{n} \cdot (\mathbf{a}^\alpha \times \mathbf{a}^\gamma)(v_{\gamma;\alpha} - vb_{\gamma\alpha}) = \varepsilon^{\alpha\gamma}v_{\gamma;\alpha} = (\varepsilon^{\alpha\gamma}v_\gamma)_{;\alpha}. \tag{2.44}$$

Assuming that the boundary to the surface $\partial\omega$ can be parameterized with arc length 's', we can write $d\mathbf{r} = \boldsymbol{\tau} ds$ with $\boldsymbol{\tau} = \frac{\partial \mathbf{r}}{\partial s}$ as shown in Fig. 2.1. Arc length parameterization would mean $\boldsymbol{\tau}$ is a unit vector. In addition, we can define the unit outward normal $\boldsymbol{\nu}$ to the boundary at each point such that

$$\boldsymbol{\nu} = \boldsymbol{\tau} \times \mathbf{n}. \tag{2.45}$$

Using the above relation we can write,

$$\mathbf{v} \cdot d\mathbf{r} = (\mathbf{v} \cdot \boldsymbol{\tau}) ds = \mathbf{v} \cdot (\mathbf{n} \times \boldsymbol{\nu}) ds. \tag{2.46}$$

Since, $\boldsymbol{\nu}$ is completely orthogonal to $\mathbf{n}$, we can write $\boldsymbol{\nu} = \nu_\alpha \mathbf{a}^\alpha$. Thus (2.46) reduces to

$$\mathbf{v} \cdot d\mathbf{r} = (v_\gamma \mathbf{a}^\gamma + v\mathbf{n}) \cdot (\mathbf{n} \times \mathbf{a}^\alpha \nu_\alpha) = v_\gamma (\mathbf{a}^\gamma \cdot \varepsilon^{\alpha\beta} \mathbf{a}_\beta) \nu_\alpha = \varepsilon^{\alpha\gamma} v_\gamma \nu^\alpha. \tag{2.47}$$

From (2.42), (2.44) and (2.47), we obtain,

$$\int_\omega (\varepsilon^{\alpha\gamma} v_\gamma)_{;\alpha} \, da = \int_{\partial\omega} \varepsilon^{\alpha\gamma} v_\gamma \, ds. \tag{2.48}$$

Defining $u^\alpha = \varepsilon^{\alpha\gamma} v_\gamma$, we can rewrite the above equation as

$$\int_\omega u^\alpha_{;\alpha} \, da = \int_{\partial\omega} u^\alpha \nu_\alpha \, ds. \tag{2.49}$$

Thus, for any vector field $\mathbf{u} = u^\alpha \mathbf{a}_\alpha + u\mathbf{n}$, the Green-Stoke's theorem reduces to

$$\int_\omega (\mathbf{u} \cdot \mathbf{a}^\alpha)_{;\alpha} \, da = \int_\omega \mathbf{u} \cdot \boldsymbol{\nu} \, ds. \tag{2.50}$$

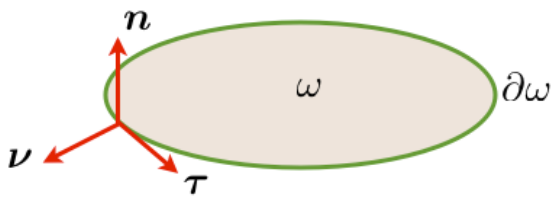

Figure 2.1: The three orthonormal vectors on a boundary $\partial\omega$.

2.2 Mechanics of Lipid Membranes

Canham proposed the quadratic energy density in curvature for modeling plasma membrane of the red blood cell [22]. Helfrich [23] then proposed the theory for lipid bilayers based on the liquid crystal theory developed by Frank [24],

under the assumptions described in the early parts of this chapter. A Continuum mechanics treatment for such surfaces was done by Jenkins [18] and Steigmann [19], where they showed that the energy functional describing the mechanics of such surface can be written as

$$E = \int_{\omega} W^*(a_{\alpha\beta}, b_{\alpha\beta})\, da + \int_{\omega} \lambda(\theta^{\alpha})\, da - pV(\omega) \tag{2.51}$$

with W^* is the strain energy density in the current configuration, $\lambda(\theta^{\alpha})$ is the Lagrange multiplier corresponding to the local area constraint and p is the Lagrange multiplier corresponding to a constraint on the volume enclosed by the bilayer surface. Fluidity is accounted through the material symmetry arguments as proposed for a simple fluid (inviscid) by Noll [25]. By considering unimodular mappings of the reference surface that do not change the strain energy density for all admissible deformations, Jenkins and Steigmann showed that the energy density depends on mean, Gaussian Curvatures and on the areal stretch J ($J = \sqrt{a/A}$). Here, 'A' represents the determinant of the metric tensor for the reference surface. Thus, in-plane deformations are only described by J, which measures the areal changes and no cost is required to penalize the shear deformations. Thus, strain energy density in the current state can be written as

$$W^*(a_{\alpha\beta}, b_{\alpha\beta}) = W(H, K). \tag{2.52}$$

The quadratic energy density proposed by Helfrich and Canham [22, 23] was of the form,

$$W(H, K) = k_B H^2 + \bar{k} K. \tag{2.53}$$

Here k_B is the mean curvature modulus or the splay modulus, corresponding to splay deformation of the lipids or the directors on the surface of the lipid bilayer and $\bar{k}$ is the Gaussian modulus. This form has been used extensively in the literature to explain various morphologies of the lipid bilayer. For lipid bilayers

which exist in closed vesicles, the term corresponding to Gaussian curvature can be ignored as the Gauss Bonnet theorem states that,

$$\int_{\omega} K\, da = 2\pi\chi - \int_{\partial\omega} \kappa_g\, ds. \tag{2.54}$$

where, χ represents the Euler-characteristic and depends on the genus for a closed orientable surface, κ_g is the geodesic curvature at the edge of the surface. Since for closed vesicles there is no edge and the cases when surface is not undergoing any topological change or is not inhomogeneous in the sense that $\bar{k}$ is uniform, the contribution from the Gaussian modulus to the energy functional can be ignored. Similar treatment also applies to surfaces with edges, when the edge has constant geodesic curvature on its edge, through the course of deformation.

To account for inhomogeneity due to curvature inducing proteins, Helfrich formulation is generally modified such that,

$$W = k_B(\theta^\alpha)(H - H_0(\theta^\alpha))^2 + \bar{k}(\theta^\alpha)K. \tag{2.55}$$

Here $\{k_B(\theta^\alpha), \bar{k}(\theta^\alpha)\}$ are the effective mean and Gaussian curvature modulus respectively and $H_0(\theta^\alpha)$ specifies the preferred curvature field on the surface. Since, the debate regarding the value or the sign of Gaussian modulus has not yet been settled in the literature, it has mostly been ignored while accounting for the effects of inhomogeneities. For the sake of generality, we will not restrict to any particular form of strain energy density to account for inhomogeneity, but instead allow W to have an explicit dependence on the material point concerned such that $W = W(H, K; \theta^\alpha)$.

For a strain energy density $W(H, K; \theta^\alpha)$, the variational formulation can be used to find its extremum which furnishes the equilibrium configuration. The principle of variation is considered such that for a particular configuration $\mathbf{r}\ (\theta^\alpha)$, a family of placements is generated by considering an explicit dependence of the mapping on another parameter ϵ (say), such that $\mathbf{r} = \mathbf{r}(\theta^\alpha; \epsilon)$. The Taylor series

expansion of $\mathbf{r}$ in ϵ about $\epsilon = 0$, which represents the surface at hand, can be written as

$$\mathbf{r}(\theta^\alpha;\epsilon) = \mathbf{r}(\theta^\alpha) + \varepsilon\mathbf{u} + O(\epsilon). \tag{2.56}$$

Defining the variational derivative as $\dot{()} = \frac{\partial()}{\partial\epsilon}$ at $\epsilon = 0$, we can write the first variation (first order variational derivative) of the energy functional defined in (2.51), as

$$\dot{E} = \int_\omega ((W_H\dot{H} + W_K\dot{K}) + (W + \lambda)\dot{J}/J)\, da - p\dot{V}. \tag{2.57}$$

Here H and K are as defined in (2.26), (W_H, W_K) represent the partial derivatives of W with respect to H and K respectively. Thus, to compute the first variation of the energy functional, we require the variations of H, K, J and V.

First variation in tangent vectors is given by

$$\dot{\mathbf{a}}_\alpha = \overline{\mathbf{r}_{,\alpha}}. \tag{2.58}$$

The superposed line with a superposed dot, $\overline{\dot{()}}$, is used represent the variational derivative of the entity (). Since the variational derivative commutes with the derivative with respect to parameterizing variables θ^α, we can write the above equation as,

$$\dot{\mathbf{a}}_\alpha = \mathbf{u}_{,\alpha}. \tag{2.59}$$

Similarly, the first variation of the components of the metric tensor can be written as

$$\dot{a}_{\alpha\beta} = \dot{\mathbf{a}}_\alpha \cdot \mathbf{a}_\beta + \mathbf{a}_\alpha \cdot \dot{\mathbf{a}}_\beta = \mathbf{u}_{,\alpha} \cdot \mathbf{a}_\beta + \mathbf{a}_\alpha \cdot \mathbf{u}_{,\beta}. \tag{2.60}$$

Using the relation,

$$\mathbf{a}_{\alpha;\beta} = \mathbf{a}_{\alpha,\beta} - \mathbf{a}_\gamma\Gamma^\gamma_{\alpha\beta} = b_{\alpha\beta}\mathbf{n}, \tag{2.61}$$

we obtain that,

$$\mathbf{u}_{;\alpha\beta} = \dot{b}_{\alpha\beta}\mathbf{n} + b_{\alpha\beta}\dot{\mathbf{n}}. \tag{2.62}$$

Since $\mathbf{n} \cdot \mathbf{n} = 1$, hence, $\mathbf{n} \cdot \dot{\mathbf{n}} = 0$. Taking the inner product of the above equation with $\mathbf{n}$, we obtain the first variation

$$\dot{b}_{\alpha\beta} = \mathbf{n} \cdot \mathbf{u}_{;\alpha\beta}. \tag{2.63}$$

Furthermore, using the relation that $a^{\beta\lambda} a_{\gamma\lambda} = \delta^{\beta}_{\gamma}$, we obtain,

$$\dot{a}^{\alpha\beta} = \dot{a}^{\alpha\gamma}\delta^{\beta}_{\gamma} + \dot{a}^{\beta\lambda}\delta^{\alpha}_{\lambda} + a^{\alpha\gamma}a^{\beta\lambda}\dot{a}_{\gamma\lambda}. \tag{2.64}$$

This yields,

$$\dot{a}^{\alpha\beta} = -a^{\alpha\gamma}a^{\beta\lambda}\dot{a}_{\gamma\lambda}. \tag{2.65}$$

Hence, using (2.26) and (2.65), we obtain

$$2\dot{H} = -b^{\alpha\beta}\dot{a}_{\alpha\beta} + a^{\alpha\beta}\dot{b}_{\alpha\beta}. \tag{2.66}$$

The first variation in the Gaussian curvature at a material point is given by,

$$2\dot{K} = e^{\alpha\beta}e^{\lambda\mu}\left[\frac{\dot{b}_{\alpha\lambda}b_{\beta\mu} + b_{\alpha\lambda}\dot{b}_{\beta\mu}}{a} - \frac{b_{\alpha\lambda}b_{\beta\mu}}{a}\frac{\dot{a}}{a}\right]. \tag{2.67}$$

Using the relations, $a = \frac{1}{2}e^{\alpha\gamma}e^{\beta\lambda}a_{\gamma\lambda}$ and $e^{\alpha\gamma}e^{\beta\lambda} = \delta^{\alpha\beta}\delta^{\gamma\lambda} - \delta^{\alpha\lambda}\delta^{\beta\gamma}$, we obtain

$$\frac{\dot{a}}{a} = a^{\alpha\beta}\dot{a}_{\alpha\beta}. \tag{2.68}$$

Using the above relation, eq. (2.67) can be reduced to the form,

$$2\dot{K} = \varepsilon^{\alpha\beta}\varepsilon^{\lambda\mu}\left[(\dot{b}_{\alpha\lambda}b_{\beta\mu} + b_{\alpha\lambda}\dot{b}_{\beta\mu}) - a^{\gamma\theta}\dot{a}_{\gamma\theta}b_{\alpha\lambda}b_{\beta\mu}\right], \tag{2.69}$$

which on substituting $\tilde{b}^{\alpha\beta} = \varepsilon^{\alpha\lambda}\varepsilon^{\beta\gamma}b_{\lambda\gamma}$, yields,

$$\dot{K} = -Ka^{\alpha\beta}\dot{a}_{\alpha\beta} + \tilde{b}^{\alpha\beta}\dot{b}_{\alpha\beta}. \tag{2.70}$$

First variation of J ($J = \sqrt{a/A}$) is given by (using (2.68)),

$$\frac{\dot{J}}{J} = \frac{\dot{a}}{2a} = \frac{1}{2}a^{\alpha\beta}\dot{a}_{\alpha\beta}, \tag{2.71}$$

and that of the enclosed volume is given by,

$$\dot{V} = \int_V \text{div } \mathbf{u}\, dV = \int_\omega \mathbf{u} \cdot \mathbf{n}\, da. \tag{2.72}$$

Now, we decompose the first variation of the position vector, $\mathbf{u}$, into the tangential and the normal directions to obtain the equilibrium criterion ($\dot{E} = 0$) along the surface and normal to the surface.

2.2.1 Tangential Variations

For tangential variations, $\mathbf{u} = u^\lambda \mathbf{a}_\lambda$, which yields,

$$\mathbf{u}_{,\alpha} = u^\lambda_{;\alpha} \mathbf{a}_\lambda + (u^\lambda b_{\lambda\alpha})\mathbf{n}. \tag{2.73}$$

Using (2.60) and (2.73), we obtain,

$$\dot{a}_{\alpha\beta} = u_{\alpha;\beta} + u_{\beta;\alpha}, \tag{2.74}$$

which along with (2.63), yields the variation of the components of the second fundamental form,

$$\dot{b}_{\alpha\beta} = u^\lambda_{;\beta} b_{\lambda\alpha} + u^\lambda_{;\alpha} b_{\beta\lambda} + u^\lambda b_{\lambda\alpha;\beta}. \tag{2.75}$$

Since $b^{\alpha\beta}$ is symmetric in α and β, using (2.73), we obtain

$$b^{\alpha\beta}\dot{a}_{\alpha\beta} = 2b^{\alpha\beta}u_{\alpha;\beta}. \tag{2.76}$$

From (2.75) and (2.76), we obtain

$$2\dot{H} = u^\alpha b^\beta_{\alpha;\beta}. \tag{2.77}$$

Using Mainardi-Codazzi equations, the above equation yields

$$\dot{H} = u^\alpha H_{,\alpha}. \tag{2.78}$$

Since, adjugate of the surface is divergence free ($\tilde{b}^{\alpha\beta}_{;\beta} = 0$), we obtain,

$$\tilde{b}^{\alpha\beta}\dot{b}_{\alpha\beta} = (u^\lambda_{;\alpha} b_{\lambda\beta} + u^\lambda_{;\beta} b_{\lambda\alpha})\tilde{b}^{\alpha\beta} + u^\lambda (b_{\lambda\alpha}\tilde{b}^{\alpha\beta})_{;\beta}. \tag{2.79}$$

Using eq. (2.74), we get

$$a^{\alpha\beta}\dot{a}_{\alpha\beta} = 2u^{\alpha}_{;\alpha}. \tag{2.80}$$

Hence, from equations (2.79) and (2.80),

$$\begin{aligned} \dot{K} &= u^{\alpha}K_{,\alpha}, \\ \frac{\dot{J}}{J} &= u^{\alpha}_{;\alpha}. \end{aligned} \tag{2.81}$$

Since $\mathbf{u}$ is tangential, $\dot{V} = 0$. Using the variations derived in (2.78) and (2.81), and substituting them to (2.57), we obtain the in-plane equilibrium condition as

$$\dot{E} = \int_{\omega} \left\{ u^{\alpha}(W_H H_{,\alpha} + W_K K_{,\alpha}) + u^{\alpha}_{;\alpha}(W + \lambda) \right\} = 0. \tag{2.82}$$

Since,

$$W_{,\alpha} = W_H H_{,\alpha} + W_K K_{,\alpha} + \frac{\partial W}{\partial \theta^{\alpha}}, \tag{2.83}$$

and from Leibniz rule for covariant derivative, $u^{\alpha}_{;\alpha}(W + \lambda) = (u^{\alpha}(W + \lambda))_{;\alpha} - u^{\alpha}(W + \lambda)_{,\alpha}$, we can rewrite the (2.83) as

$$\dot{E} = \int_{\omega} \left\{ (u^{\alpha}(W + \lambda))_{;\alpha} - u^{\alpha}\left(\lambda_{,\alpha} + \frac{\partial W}{\partial \theta^{\alpha}}\right) \right\} da. \tag{2.84}$$

Using the Green's-Stokes theorem, the first term in the above integral can be reduced to the edge of the domain ($\partial\omega$), such that

$$\dot{E} = \int_{\omega} -u^{\alpha}\left(\lambda_{,\alpha} + \frac{\partial W}{\partial \theta^{\alpha}}\right) da + \int_{\partial\omega} u^{\alpha}(W + \lambda)\nu_{\alpha} ds. \tag{2.85}$$

Thus, for equilibrium in the tangential plane of the surface, it is required that,

$$\lambda_{,\alpha} = -\frac{\partial W}{\partial \theta^{\alpha}}. \tag{2.86}$$

When the surface is homogenous, the above equation reduces to the criterion that the surface tension field is constant (λ = constant). We will combine the edge contributions from tangential and normal variations later to get the necessary forces and moments at the boundary which keep the surface in equilibrium.

2.2.2 Normal Variations

For normal variations $\mathbf{u} = u(\theta^\alpha)\mathbf{n}$. Thus,

$$\mathbf{u}_{,\alpha} = (\mathbf{u}_{,\alpha} \cdot \mathbf{a}^\beta)\mathbf{a}_\beta + (\mathbf{u}_{,\alpha} \cdot \mathbf{n})\mathbf{n}, \tag{2.87}$$

which, reduces to

$$\mathbf{u}_{,\alpha} = -ub^\beta_\alpha \mathbf{a}_\beta + u_{,\alpha}\mathbf{n}. \tag{2.88}$$

Hence, the first variation of the components of the first and the second fundamental forms, with the help of (2.60) and (2.63), are given by

$$\dot{a}_{\alpha\beta} = -2ub_{\alpha\beta} \tag{2.89}$$

and

$$\dot{b}_{\alpha\beta} = u_{;\alpha\beta} - ub_{\alpha\lambda}b^\lambda_\beta. \tag{2.90}$$

Furthermore, using (2.89) we obtain,

$$b^{\alpha\beta}\dot{a}_{\alpha\beta} = -2ub^{\alpha\beta}b_{\alpha\beta}. \tag{2.91}$$

Using Cayley-Hamilton theorem, we obtain

$$b^{\alpha\beta}b_{\alpha\beta} = (2Ha^{\alpha\beta} - \tilde{b}^{\alpha\beta})b_{\alpha\beta} = 4H^2 - 2K, \tag{2.92}$$

and from (2.90), we get

$$a^{\alpha\beta}\dot{b}_{\alpha\beta} = a^{\alpha\beta}u_{;\alpha\beta} - u(4H^2 - 2K). \tag{2.93}$$

Using (2.91), (2.92) and (2.93), we obtain the variation of the mean curvature as

$$2\dot{H} = \Delta u + u(4H^2 - 2K). \tag{2.94}$$

From (2.89), we obtain

$$a^{\alpha\beta}\dot{a}_{\alpha\beta} = -4uH, \tag{2.95}$$

and from (2.90), we obtain

$$\tilde{b}^{\alpha\beta}\dot{b}_{\alpha\beta} = \tilde{b}^{\alpha\beta}u_{;\beta\alpha} - 2KHu. \tag{2.96}$$

Using (2.95) and (2.96), we compute the variation of the Gaussain curvature and areal stretch as

$$\dot{K} = 2uHK + u_{;\alpha\beta}\tilde{b}^{\alpha\beta}, \quad \dot{J}/J = -2uH. \tag{2.97}$$

Furthermore, the variation of the volume is given by

$$\dot{V} = \int_{\omega} u\, da. \tag{2.98}$$

Thus, for normal variation (2.57) reduces to

$$\begin{aligned}\dot{E} = &\int_{\omega} \frac{1}{2}W_H\Big(u_{;\alpha\beta}a^{\alpha\beta} + u(4H^2 - 2K)\Big) + W_K(2KHu + \tilde{b}^{\alpha\beta}u_{;\alpha\beta}) \\ &- 2uH(W + \lambda)\, da - p\int_{\omega} u\, da.\end{aligned} \tag{2.99}$$

Since the metric is covariant constant and the contravariant adjugate is divergence free, we obtain the following relations using the Leibniz rule,

$$u_{;\alpha\beta}W_H a^{\alpha\beta} = (a^{\alpha\beta}W_H u_{,\alpha})_{;\beta} + ua^{\alpha\beta}(W_H)_{;\beta\alpha} - [ua^{\alpha\beta}(W_H)_{,\beta}]_{;\alpha} \text{ and} \tag{2.100}$$

$$\tilde{b}^{\alpha\beta}W_K u_{;\alpha\beta} = (\tilde{b}^{\alpha\beta}W_K u_{,\alpha})_{;\beta} + u\tilde{b}^{\alpha\beta}(W_K)_{;\beta\alpha} - [u\tilde{b}^{\alpha\beta}(W_K)_{,\beta}]_{;\alpha}. \tag{2.101}$$

Since the divergence terms can be transformed to integrals on the boundary, using (2.99), (2.100) and (2.101), we obtain the following condition by setting the first variation of the energy functional to zero

$$\frac{1}{2}\Delta W_H + (W_K)_{;\alpha\beta}\tilde{b}^{\alpha\beta} + W_H(2H^2 - K) + 2H(KW_K - W) - 2H\lambda = p. \tag{2.102}$$

The above equation represents the equilibrium criterion in the normal direction and is commonly termed as the "shape equation" in the literature.

2.2.3 Boundary Forces and Moments

The boundary terms obtained from the tangential and the normal variations of the energy functional ($\dot{E}_B$) are,

$$\begin{aligned}\dot{E}_B = \int_{\partial\omega} \Big[& u^\alpha (W+\lambda)\nu_\alpha + a^{\alpha\beta} W_H u_{,\alpha}\nu_\beta - u a^{\alpha\beta}(W_H)_{,\beta}\nu_\beta \\ & + \tilde{b}^{\alpha\beta} W_K u_{,\alpha}\nu_\beta - \tilde{b}^{\alpha\beta}(W_K)_{,\beta} u \nu_\alpha \Big]\, ds.\end{aligned} \tag{2.103}$$

A natural choice for the parameter space on the boundary is given by the tangent vectors $\boldsymbol{\tau}$ and $\boldsymbol{\nu}$ (along the curve and normal to it). Thus,

$$u' = u_{,\alpha}\tau^\alpha, \qquad \text{and} \qquad u_{,\nu} = u_{,\alpha}\nu^\alpha, \tag{2.104}$$

are the derivatives of u along and normal to the curve $\partial\omega$, respectively. Using the above equation, we can write

$$u_{,\alpha} = u'\tau_\alpha + u_{,\nu}\nu_\alpha. \tag{2.105}$$

Using the above relation, the boundary integral in (2.103) can be written as

$$\begin{aligned}\dot{E}_B = & \int_{\partial\omega} [(\tau W_K)' - \frac{1}{2}\nu^\beta (W_H)_{,\beta} - \tilde{b}^{\alpha\beta}(W_K)_{,\beta}\nu_\alpha] u \, da \\ & + \int_{\partial\omega} \left(\frac{1}{2} W_H + \kappa_\tau W_K\right) u_{,\nu}\, ds + \sum u W_K[\tau].\end{aligned} \tag{2.106}$$

In the above equation, $\kappa_\tau = b_{\alpha\beta}\tau^\alpha\tau^\beta$ and $\tau = b_{\alpha\beta}\tau^\alpha\nu^\beta$ represent the normal curvature in the direction of $\boldsymbol{\tau}$ and the twist in the surface, respectively. Furthermore, the curvature in the normal direction $\boldsymbol{\nu}$ is given by $\kappa_\nu = b_{\alpha\beta}\nu^\alpha\nu^\beta$.

Using the relation,

$$u_{,\nu} = -\boldsymbol{\tau}\cdot\boldsymbol{\omega} - \mathbf{b}\boldsymbol{\nu}\cdot\mathbf{u}, \tag{2.107}$$

with $\boldsymbol{\omega}$ being defined such that $\dot{\mathbf{n}} = \boldsymbol{\omega}\times\mathbf{n}$ [26], the boundary integral can be expressed as

$$\begin{aligned}\dot{E}_B = & \int_{\partial\omega} (F_\nu\boldsymbol{\nu} + F_\tau\boldsymbol{\tau} + F_n\mathbf{n})\cdot\mathbf{u}\, ds - \int_{\partial\omega} M\boldsymbol{\tau}\cdot\boldsymbol{\omega}\, ds \\ & + \sum_i \mathbf{f}_i\cdot\mathbf{u}_i,\end{aligned} \tag{2.108}$$

where,

$$
\begin{aligned}
M &= \frac{1}{2}W_H + \kappa_\tau W_K, \\
F_\nu &= W + \lambda - \kappa_\nu M, \\
F_\tau &= -\tau M, \\
F_n &= (\tau W_K)' - \frac{1}{2}(W_H)_{,\nu} - (W_K)_{,\beta}\tilde{b}^{\alpha\beta}\nu_\alpha, \\
\mathbf{f}_i &= (W_K[\tau])_i \mathbf{n}.
\end{aligned}
\tag{2.109}
$$

Here M represents the boundary moment per unit length. F_ν, F_n and F_τ represent the forces per unit length acting on the boundary along the directions $\boldsymbol{\nu}, \mathbf{n}$ and $\boldsymbol{\tau}$, respectively. Above $\mathbf{f}_i$ represents the forces at the corners (if any) of the boundary and [] represents the forward jump in τ at the corners of the boundary.

Table 2.1: Notations

Notation	**Significance**
θ^α	Parameters describing the surface
$\mathbf{r}(\theta^\alpha)$	Position vector of the points on surface
$\mathbf{a}_\alpha$	Tangent vectors to the surface
$a_{\alpha\beta}$	Components of the metric tensor
$a^{\alpha\beta}$	Components of the dual metric tensor
$e^{\alpha\beta}$	Components of the permutation tensor
$\varepsilon^{\alpha\beta}$	Components of the permutation tensor density
$\mathbf{n}$	unit normal to the surface at any given point
$b_{\alpha\beta}$	Components of the curvature tensor
$\tilde{b}^{\alpha\beta}$	Contravariant adjugate of $b_{\alpha\beta}$
Ω	Reference configuration
ω	Current configuration

Continued on next page

Table 2.1: Notations

Notation	Significance
Ω_a	Areal domain of actin force in reference configuration
ω_a	Areal domain of actin force in current configuration
W	Strain Energy density in the current configuration
P	Transmembrane Pressure
V	Volume enclosed by the membrane
J	Areal stretch of the surface
a	Determinant of the metric tensor in the current configuration
A	Determinant of the metric tensor in the reference configuration
$\lambda(\theta^\alpha)$	Surface tension field
$\boldsymbol{\tau}$	Unit tangent to the boundary of the surface
$\boldsymbol{\nu}$	Unit vector normal to $\boldsymbol{\tau}$ and $\mathbf{n}$ at the boundary
M	Moment per unit length at the boundary
F_τ	Force per unit length acting on the boundary along the direction $\boldsymbol{\tau}$
F_ν	Force per unit length acting on the boundary along the direction $\boldsymbol{\nu}$
F_n	Force per unit length acting on the boundary along the direction $\mathbf{n}$
$H_0(\theta^\alpha)$	Preferred mean curvature field
$D_0(\theta^\alpha)$	Preferred deviatoric curvature field
E_b	Free energy of the bilayer
E_f	Work done by actin forces
$\boldsymbol{\lambda}$	Direction of alignment of BAR protein
$\boldsymbol{\mu}$	Direction perpendicular to $\boldsymbol{\lambda}$ of BAR in tangent plane
κ_λ	Normal curvature along direction $\boldsymbol{\lambda}$
κ_μ	Normal curvature along direction $\boldsymbol{\mu}$

Continued on next page

Table 2.1: Notations

Notation	Significance
κ_λ^0	Preferred normal curvature along direction $\boldsymbol{\lambda}$
κ_μ^0	Preferred normal curvature along direction $\boldsymbol{\mu}$
k_B	Bending modulus of the bare lipid bilayer
$\bar{k}$	Gaussian modulus of the bare lipid bilayer
R_0	Normalizing radius of curvature
k_0	Mean curvature modulus of the bare lipid bilayer
$\hat{k}_B(\theta^\alpha)$	Bending modulus in the clathrin coated domain of membrane.
$\hat{\bar{k}}(\theta^\alpha)$	Gaussian modulus in the clathrin coated domain of membranes.
$\hat{k}_1(\theta^\alpha)$	Spatially varying modulus (C^∞) associated with mean curvature.
$\hat{k}_2(\theta^\alpha)$	Spatially varying modulus (C^∞) associated with deviatoric curvature.
$\hat{k}_3(\theta^\alpha)$	Spatially varying modulus (C^∞) associated with Gaussian curvature.
$\mathbf{f}$	Force per unit area applied by actin in the current configuration
$\tilde{\mathbf{f}}$	Force per unit mass applied by actin
ρ	Mass per unit area in the current configuration
ρ_0	Mass per unit area in the reference configuration

2.3 Acknowledgement

This chapter is completely based on the shell theory notes of Prof. David Steigmann and papers [19, 26, 27, 28].

Chapter 3 Orthotropic Spontaneous Curvatures in Lipid Membranes

3.1 Introduction

Cellular membranes undergo dynamic remodeling for successful execution of various processes such as cellular transport, cell mobility, cell division to name a few [29, 30, 5, 31, 32, 33]. This, in general, entails local bending of the membrane that could single-handedly or collectively be caused by i) curvature-inducing proteins or lipids, ii) active forces-generating cytoskeletal filaments, and iii) symmetry breaking enzymes [32, 33]. In the existing literature on membrane mechanics, this bending effect has been modeled on the continuum scale by introducing a so-called spontaneous curvature field. The application of this concept has ranged from studies modeling shapes of biological structures such as red-blood cells to studies modeling processes such as cellular transport [5, 29].

The idea of a spontaneous curvature field is tied to the form of the strain energy function of a lipid membrane. For the Helfrich model, the strain energy depends on the local mean curvature and the Gaussian curvature of the surface [23, 34, 35]. For this model with quadratic dependence on mean curvature and linear dependence on Gaussian curvature, a preferred geometry imposed by curvature-inducing proteins can be generated by prescribing a resting mean curvature and a Gaussian curvature. In general, the preferred mean curvature, called the spontaneous curvature, has been used in the literature to regulate the membrane geometry by shifting the vertex of the parabolic energy landscape (associated with the mean curvature) to the prescribed curvature.

This approach works well for proteins that form spherical coats and induce

an isotropic curvature such as in clathrin. However, BAR proteins impose a cylindrical curvature instead of a spherical curvature [36, 37, 38, 39]. Fig. 3.1 shows the two types of protein scaffolds and their effect on membrane geometry. As the normal curvatures along the longitudinal axis and the circumferential direction of a cylinder are different, spontaneous curvatures generated by such proteins are anisotropic in nature. As a consequence, the standard Helfrich model is not equipped to model such membrane-protein interactions because of the inherent isotropy assumed for its derivation.

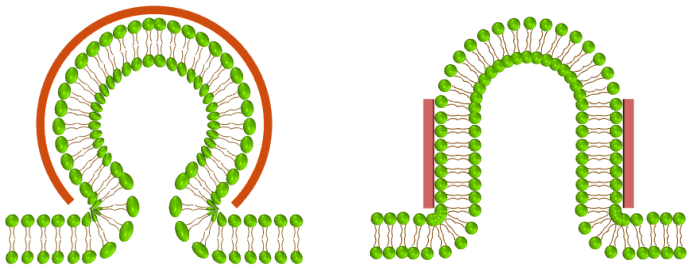

(a) (b)

Figure 3.1: Different types of protein scaffolds around the membrane (shown in red). (a) A spherical scaffold made by proteins such as clathrin, and (b) a cylindrical scaffold as those made by BAR proteins.

To address this issue, several studies have proposed a modified quadratic strain energy in different contexts. A generalized energy for membranes where tilting and chirality of lipids gives rise to anisotropic spontaneous curvatures was proposed in [40]. In a series of papers, the effect of anisotropic inclusions was studied via a mismatch tensor that energetically penalized the difference between the intrinsic curvatures preferred by the inclusions and the local membrane curvatures along the preferred directions [41, 42, 43]. For a nematic membrane made of rod-like molecules, a strain energy that incorporated spontaneous curvatures in both the normal curvatures and the twist was proposed in [44]. Models for

BAR protein attachment that account for membrane-protein electrostatic interactions and symmetry breaking by loop insertion have been reviewed in [45]. In addition to these works, computational models and all atom molecular dynamics model have been developed to investigate the interaction of BAR proteins with the lipid membrane [46, 47, 48, 49, 50, 51, 52, 53]. For an extensive list of theoretical and computational studies on membrane-protein interactions, we refer the reader to [54, 55].

In this chapter, we build upon these works to present a detailed derivation of a generalized theory to model interactions of a membrane with non-spherical protein scaffolds. In particular, we derive the Euler-Lagrange equations in a fully nonlinear setting for an inhomogeneous membrane that is equipped to capture spatial variations in membrane and protein coat properties. In addition to the *modified shape equation*, we present the force equilibrium equation in the tangential plane that has not been discussed before in the context of orthotropic membranes. Furthermore, we derive the explicit expressions for forces and moment that act locally at any arbitrary boundary in such a membrane.

3.2 Strain energy

Lipid membrane and the protein scaffold form a non-standard composite system. It bears similarity to fiber-reinforced solid materials that exhibit anisotropy generated by the directionality of the fibers [56]. However, there is a fundamental difference that distinguishes the two materials. In a fiber-reinforced material, the fibers are embedded in the matrix and as a result, the fibers get convected with the matrix when subjected to a deformation. In contrast, BAR proteins are not transmembrane proteins and sit outside the outer monolayer. Thus, while the protein shell is more solid-like, the membrane inside still remains fluid

allowing lipids to diffuse over the surface. Furthermore, the curvature-inducing proteins are more dynamic and can diffuse and reorient on the surface and self-assemble in different configurations depending on their spatial distribution and membrane geometry. As a result, these proteins cannot be modeled as embedded entities that get convected with a deforming membrane. This fact limits the use of symmetry arguments in reference configuration typically used to obtain restrictions on the constitutive functions of fiber-reinforced materials. To circumvent this problem, we impose symmetry restrictions in the current configuration, similar to the approach proposed in [41, 42, 43]. This ensures incorporation of directional effects from the curvature-inducing proteins without picking-up unphysical effects due to protein embedding.

Let ω be a two-dimensional surface with a non-uniform distribution of crescent or banana shaped bar proteins that prefer anisotropic curvatures. The locus of points on ω is tracked by the position vector $\mathbf{r}(\theta^\mu)$ where θ^μ $(\mu = 1, 2)$ are the surface coordinates. The metric and curvature tensor on the surface are computed based on this parametrization as mentioned in Chapter 2. We assume that the curvatures induced by the proteins depend both on the geometry of the proteins and their local concentrations. The orientation of a protein on the surface is given by a unit vector $\boldsymbol{\lambda}(\theta^\mu)$ that is tangential to the 1-D curve that captures the in-plane protein geometry as shown in Fig. 3.2(a). The orientational vector $\boldsymbol{\lambda}$ and the surface normal $\mathbf{n}$ furnish a third orthonormal vector $\boldsymbol{\mu} = \mathbf{n} \times \boldsymbol{\lambda}$ which together form a local triad $\{\boldsymbol{\lambda}, \boldsymbol{\mu}, \mathbf{n}\}$ at any point on the surface.

Since a membrane behaves as a fluid shell offering bending resistance, the strain energy function depends on the curvature tensor $\mathbf{b}$. However, unlike the classical model, for the present case we assume an additional dependance on a structural tensor

$$\mathbf{M} = \boldsymbol{\lambda} \otimes \boldsymbol{\lambda} - \boldsymbol{\mu} \otimes \boldsymbol{\mu} \tag{3.1}$$

to capture the anisotropic spontaneous curvatures generated from membrane-protein interactions. Such a structural tensor is routinely used to define orthotropic symmetry in two-dimensional materials [57]. In the present setting, we do not resort to a reference configuration and require the model to have orthotropic symmetry in the current configuration. This is motivated by the fact that a banana shaped protein rotated by 180^0 cannot be distinguished from the original protein. As a consequence, the normal spontaneous curvatures they generate are also indistinguishable (Fig. 3.2(b)). As is necessary for any material, we require the strain energy density $W(\mathbf{b}, \mathbf{M})$ to be Galilean invariant. This yields a list of invariants

$$I = \{tr(\mathbf{b}), tr(\mathbf{M}), det(\mathbf{b}), det(\mathbf{M}), tr(\mathbf{Mb})\}. \tag{3.2}$$

Since the second and fourth invariants above are constant scalar fields, the irreducible basis comprises of three elements H, K, and D where $H = tr(\mathbf{b})/2$ is the mean curvature, $K = det(\mathbf{b})$ is the Gaussian curvature, and $D = tr(\mathbf{Mb})/2$ is the curvature deviator. In addition to H and K present in the Helfrich model, W now has dependence on a new element D because of the directionality imposed by an orthotropic protein scaffold.

To get insight into the invariants, we compute them in terms of the local principal curvatures. In the $\{\mathbf{a}_\alpha, \mathbf{a}_\beta\}$ and $\{\boldsymbol{\lambda}, \boldsymbol{\mu}\}$ bases, they can be expressed as

$$\begin{aligned} H &= \frac{1}{2} a^{\alpha\beta} b_{\alpha\beta} = (\kappa_\lambda + \kappa_\mu)/2, \\ K &= \frac{1}{2} \varepsilon^{\alpha\beta} \varepsilon^{\theta\psi} b_{\alpha\theta} b_{\beta\psi} = \kappa_\lambda \kappa_\mu - \tau^2, \\ D &= \frac{1}{2} b_{\alpha\beta} (\lambda^\alpha \lambda^\beta - \mu^\alpha \mu^\beta) = (\kappa_\lambda - \kappa_\mu)/2, \end{aligned} \tag{3.3}$$

where,

$$\kappa_\lambda = b_{\alpha\beta} \lambda^\alpha \lambda^\beta, \;\; \kappa_\mu = b_{\alpha\beta} \mu^\alpha \mu^\beta, \;\; \tau = b_{\alpha\beta} \lambda^\alpha \mu^\beta \tag{3.4}$$

are the normal curvatures along $\boldsymbol{\lambda}$ and $\boldsymbol{\mu}$, and the twist, respectively. Above, λ^α

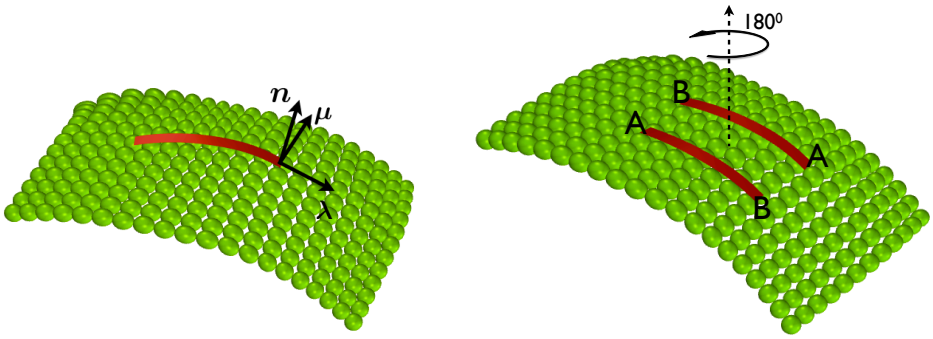

(a) (b)

Figure 3.2: Protein attachment on the membrane. a) Orientation of the protein in the tangential plane, and b) 180^0 rotation of the protein about the surface normal leads to an indistinguishable state.

and μ^α are the projections of $\boldsymbol{\lambda}$ and $\boldsymbol{\mu}$ along the tangent vectors with

$$\begin{aligned} \lambda^\alpha &= \boldsymbol{\lambda} \cdot \mathbf{a}^\alpha \quad \text{and} \\ \mu^\alpha &= \boldsymbol{\mu} \cdot \mathbf{a}^\alpha = (\mathbf{n} \times \boldsymbol{\lambda}) \cdot \mathbf{a}^\alpha = \varepsilon^{\theta\alpha} \lambda^\psi a_{\theta\psi}, \end{aligned} \tag{3.5}$$

where $\varepsilon^{\alpha\beta} = a^{-1/2} e^{\alpha\beta}$, $a = det(a_{\alpha\beta})$ and $e^{\alpha\beta}$ is the permutation tensor with $e^{12} = -e^{21} = 1$ and zero if $\alpha = \beta$. From eq. $(3.3)_3$, it is evident that D is the difference in the normal curvatures along the two orthogonal directions allowing us to prescribe a new spontaneous curvature D_0 that captures the protein-induced anisotropic curvatures. This is similar to prescribing H_0, the spontaneous curvature associated with the mean curvature in the Helfrich model. Since $\{H, D\}$ together uniquely determine $\{\kappa_\lambda, \kappa_\mu\}$ and vice-versa (see eq. 3.3), prescribing $\{H_0, D_0\}$ is analogous to imposing preferred curvatures $\{\kappa_\lambda^0, \kappa_\mu^0\}$ in the two directions $\boldsymbol{\lambda}$ and $\boldsymbol{\mu}$. In contrast, imposing a set of $\{H_0, K_0\}$ can lead to infinitely many combinations of $\{\kappa_\lambda^0, \kappa_\mu^0\}$. Hence, the unique direction of attaching proteins cannot be deciphered in a model that depends solely on H and K.

3.3 Variations

Based on the Kirchhoff-Love Shell theory assumptions of constant thickness and lipids aligned with the normal direction, we write the energy functional accounting for lipid bilayer interacting with orthotropic proteins as:

$$E = \int_{\omega} (W(H, D, K; \theta^{\alpha}) + \lambda(\theta^{\alpha}))da - pV(\omega), \tag{3.6}$$

with λ and p as Lagrange multipliers to constrain the area and volume enclosed respectively.

We consider a family of surfaces generated by $\mathbf{r}(\theta^{\alpha}; \epsilon)$. The virtual displacement of the surface is given by $\mathbf{u}(\theta^{\alpha}) = \frac{\partial}{\partial \epsilon}\mathbf{r}(\theta^{\alpha}; \epsilon)_{|\epsilon=0} = \dot{\mathbf{r}}$, where the superposed dot refers to the derivative with respect to the parameter ϵ [27]. Variation of E in (3.6) yields

$$\dot{E} = \int_{\omega} \dot{W} da + \int_{\omega} (W + \lambda)(\dot{J}/J)\, da - p\dot{V}, \tag{3.7}$$

where $J = \sqrt{a/A}$ is the ratio of the material area after deformation to that before, and

$$\dot{W} = W_H \dot{H} + W_K \dot{K} + W_D \dot{D}. \tag{3.8}$$

The variations of the mean curvature and the Gaussian curvature are given by

$$\begin{aligned} 2\dot{H} &= a^{\alpha\beta}\dot{b}_{\alpha\beta} - b^{\alpha\beta}\dot{a}_{\alpha\beta}, \\ \dot{K} &= -Ka^{\alpha\beta}\dot{a}_{\alpha\beta} + \tilde{b}^{\alpha\beta}\dot{b}_{\alpha\beta}. \end{aligned} \tag{3.9}$$

Variation of the curvature deviator, using $(3.3)_3$, can be expressed as

$$\dot{D} = \frac{1}{2}(\dot{\kappa}_{\lambda} - \dot{\kappa}_{\mu}). \tag{3.10}$$

Using (3.4), variations of κ_{λ} and κ_{μ} can be expressed as

$$\begin{aligned} \dot{\kappa}_{\lambda} &= \dot{b}_{\alpha\beta}\lambda^{\alpha}\lambda^{\beta} + 2b_{\alpha\beta}\dot{\lambda}^{\alpha}\lambda^{\beta} \quad \text{and} \\ \dot{\kappa}_{\mu} &= \dot{b}_{\alpha\beta}\mu^{\alpha}\mu^{\beta} + 2b_{\alpha\beta}\dot{\mu}^{\alpha}\mu^{\beta}. \end{aligned} \tag{3.11}$$

It is important to emphasize here that there are two mappings from the parameter space to the current configuration. One is the position field $\mathbf{r}\,(\theta^\alpha)$ and the other $\boldsymbol{\lambda}(\theta^\alpha)$, which specifies the in-plane orientation of the protein dimers. These proteins are convected to the surface such that they remain in the tangent plane of the surface in all configurations. Thus, the variations have to be considered such that $\overline{\dot{\boldsymbol{\lambda}} \cdot \mathbf{n}} = 0$. The superposed dot over the line represents the variation of the overall quantity. Since, the orientation of protein along the surface is not convected to the surface, it's component along the surface is assumed to remain constant while considering the variations such that,

$$\overline{\dot{\boldsymbol{\lambda}} \cdot \mathbf{a}_\alpha \mathbf{a}^\alpha} = 0. \tag{3.12}$$

Hence, the variation of $\boldsymbol{\lambda}$ is completely normal to the surface and can be written as,

$$\dot{\boldsymbol{\lambda}} = (\dot{\boldsymbol{\lambda}} \cdot \mathbf{n})\mathbf{n}. \tag{3.13}$$

Similarly, variation of $\boldsymbol{\mu}$, is

$$\dot{\boldsymbol{\mu}} = \dot{\mathbf{n}} \times \boldsymbol{\lambda} + \mathbf{n} \times \dot{\boldsymbol{\mu}} = \dot{\mathbf{n}} \times \boldsymbol{\lambda}. \tag{3.14}$$

Since $\mathbf{n} \cdot \mathbf{n} = 1$, $\dot{\mathbf{n}}$ is perpendicular to $\mathbf{n}$ and lies in the tangent plane. As a result, $\dot{\mathbf{n}} \times \boldsymbol{\lambda}$ is oriented along the normal whose projection in the tangential plane vanishes.

Thus, using eq. (3.5), eq. (3.13), eq. (3.14) and the relation $\mathbf{a}^\alpha = a^{\alpha\gamma}\mathbf{a}_\gamma$, we can compute

$$\begin{aligned} \dot{\lambda}^\alpha &= a^{\alpha\gamma}(\boldsymbol{\lambda} \cdot \dot{\mathbf{a}}_\gamma) + (\boldsymbol{\lambda} \cdot \mathbf{a}_\gamma)\dot{a}^{\alpha\gamma} \quad \text{and} \\ \dot{\mu}^\alpha &= a^{\alpha\gamma}(\boldsymbol{\mu} \cdot \dot{\mathbf{a}}_\gamma) + (\boldsymbol{\mu} \cdot \mathbf{a}_\gamma)\dot{a}^{\alpha\gamma}. \end{aligned} \tag{3.15}$$

Substituting (3.11) and (3.15) in (3.10), we can finally obtain

$$\begin{aligned} \dot{D} = \frac{1}{2}\dot{b}_{\alpha\beta}(\lambda^\alpha\lambda^\beta - \mu^\alpha\mu^\beta) + b_{\alpha\beta}[a^{\alpha\gamma}\dot{\mathbf{a}}_\gamma \cdot (\lambda^\beta\boldsymbol{\lambda} - \mu^\beta\boldsymbol{\mu}) \\ + \dot{a}^{\alpha\gamma}\mathbf{a}_\gamma \cdot (\lambda^\beta\boldsymbol{\lambda} - \mu^\beta\boldsymbol{\mu})]. \end{aligned} \tag{3.16}$$

3.3.1 Tangential Variations

For tangential variation $\mathbf{u} = u^{\lambda}\mathbf{a}_{\lambda}$, we have (chapter 2)

$$\dot{\mathbf{a}}_{\gamma} = u^{\eta}{}_{;\gamma}\mathbf{a}_{\eta} + u^{\lambda}b_{\lambda\gamma}\mathbf{n} \tag{3.17}$$

and

$$\dot{a}^{\alpha\gamma} = -a^{\alpha\theta}a^{\gamma\psi}(u_{\theta;\psi} + u_{\psi;\theta}). \tag{3.18}$$

Substitution of (3.17) and (3.18) in $(3.15)_1$ furnishes

$$\dot{\lambda}^{\alpha} = -\lambda_{\gamma}a^{\alpha\theta}a^{\gamma\psi}(u_{\theta;\psi} + u_{\psi;\theta}) + a^{\alpha\theta}u^{\gamma}_{;\theta}\lambda_{\gamma}. \tag{3.19}$$

Since the metric is covariant constant,

$$a^{\gamma\psi}u_{\psi;\theta} = u^{\gamma}_{;\theta}, \quad \text{and} \quad a^{\alpha\theta}u_{\theta;\psi} = u^{\alpha}_{;\psi}. \tag{3.20}$$

Combining (3.19) with eq. (3.20) yields

$$\dot{\lambda}^{\alpha} = -\lambda^{\psi}u^{\alpha}_{;\psi}. \tag{3.21}$$

Following a similar procedure, we can show

$$\dot{\mu}^{\alpha} = -\mu^{\psi}u^{\alpha}_{;\psi}. \tag{3.22}$$

We employ (3.11), (3.21), (3.22) along with the Mainardi-Codazzi equations, and the variation of the covariant components of the curvature tensor [27]

$$\dot{b}_{\alpha\beta} = u^{\eta}_{;\alpha}b_{\eta\beta} + u^{\eta}_{;\beta}b_{\eta\alpha} + u^{\eta}b_{\eta\alpha;\beta} \tag{3.23}$$

to compute

$$\dot{\kappa}_{\lambda} = u^{\eta}b_{\alpha\beta;\eta}\lambda^{\alpha}\lambda^{\beta}, \text{ and } \dot{\kappa}_{\mu} = u^{\eta}b_{\alpha\beta;\eta}\mu^{\alpha}\mu^{\beta}. \tag{3.24}$$

Substitution of (3.24) in (3.10) finally furnishes the variation of the curvature deviator

$$\dot{D} = u^{\eta}b_{\alpha\beta;\eta}(\lambda^{\alpha}\lambda^{\beta} - \mu^{\alpha}\mu^{\beta})/2. \tag{3.25}$$

Further, we note that since $\boldsymbol{\lambda}$ and $\boldsymbol{\mu}$ span the tangent plane and are unit vectors, we can write the contravariant basis such that,

$$\mathbf{a}^{\alpha} = (\mathbf{a}^{\alpha} \cdot \boldsymbol{\lambda})\boldsymbol{\lambda} + (\mathbf{a}^{\alpha} \cdot \boldsymbol{\mu})\boldsymbol{\mu}. \tag{3.26}$$

Thus we obtain,

$$a^{\alpha\beta} = \lambda^{\alpha}\lambda^{\beta} + \mu^{\alpha}\mu^{\beta}. \tag{3.27}$$

Using this we can write,

$$\dot{D} = u^{\eta} b_{\alpha\beta;\eta}(2\lambda^{\alpha}\lambda^{\beta} - a^{\alpha\beta})/2. \tag{3.28}$$

Having obtained $\dot{D}$, we can now proceed to derive the force equilibrium equation in the tangential plane. Since $\dot{V}$ vanishes for tangential variations and $\dot{J}/J = u^{\eta}_{;\eta}$ [27], we can write eq. (3.7) as

$$\dot{E} = \int_{\omega} [\dot{W} - u^{\eta}(W + \lambda)_{;\eta}]da + \int_{\omega} [u^{\eta}(W + \lambda)]_{;\eta} da, \tag{3.29}$$

where

$$W_{,\eta} = W_H H_{,\eta} + W_K K, \eta + W_D D_{,\eta} + \partial W/\partial\theta^{\eta}. \tag{3.30}$$

Making use of $\dot{H} = u^{\eta} H_{,\eta}$ and $\dot{K} = u^{\eta} K_{,\eta}$ (derived in Chapter 2) together with eqs. (3.8), (3.28), (3.29), (3.30) and the Stokes' theorem, we compute the Euler-Lagrange equation

$$\lambda_{,\eta} = -\partial W/\partial\theta^{\eta} - W_D b_{\alpha\beta}(\lambda^{\alpha}\lambda^{\beta})_{;\eta}. \tag{3.31}$$

The above equation allows for the computation of the surface tension field on the surface. It generalizes the tangential equilibrium equation derived in [27, 18] for homogeneous membranes and in [28] for membranes interacting with isotropic curvature inducing proteins. The first term on the right is a result of spatial heterogeneities in membrane properties and holds both for isotropic and anisotropic membranes. The second term is specific to anisotropic membranes and is governed by the functional dependence of the strain energy on D and the

orientation of the proteins. If the membrane is homogeneous and isotropic, right-hand side would vanish, furnishing a uniform surface tension over the entire surface. However, if the properties vary spatially or have a directionality, as is expected in the present context, the right-hand side can be non-zero forcing the surface tension to evolve over the surface.

3.3.2 Normal Variations

For normal variation $\mathbf{u} = u(\theta^\alpha)\mathbf{n}$, we follow a similar procedure. Using eq. (3.15) and the relations

$$\begin{aligned} &\dot{\mathbf{a}}_\alpha = u_{,\alpha}\mathbf{n} - ub^\beta_\alpha \mathbf{a}_\beta, \quad \text{and} \quad \dot{a}_{\alpha\beta} = -2ub_{\alpha\beta}, \\ &\dot{b}_{\alpha\beta} = u_{;\alpha\beta} - ub_{\alpha\gamma}b^\gamma_\beta \end{aligned} \tag{3.32}$$

(from Chapter 2), we derive

$$\dot{\lambda^\alpha} = ub^\gamma_\psi a^{\alpha\psi}\lambda_\gamma, \quad \text{and} \quad \dot{\mu^\alpha} = ub^\gamma_\psi a^{\alpha\psi}\mu_\gamma. \tag{3.33}$$

Substituting (3.32) and (3.33) in (3.11), we compute the variations of the normal curvatures

$$\begin{aligned} \dot{\kappa}_\lambda &= [u_{;\alpha\beta} + ub_{\alpha\gamma}b^\gamma_\beta]\lambda^\alpha\lambda^\beta \quad \text{and} \\ \dot{\kappa}_\mu &= [u_{;\alpha\beta} + ub_{\alpha\gamma}b^\gamma_\beta]\mu^\alpha\mu^\beta, \end{aligned} \tag{3.34}$$

which together with (3.10) yield

$$\dot{D} = (u_{;\alpha\beta} + ub_{\alpha\gamma}b^\gamma_\beta)(\lambda^\alpha\lambda^\beta - \mu^\alpha\mu^\beta)/2. \tag{3.35}$$

Substituting (3.35), along with the relations

$$\begin{aligned} &2\dot{H} = \Delta u + u(4H^2 - 2K), \;\; \dot{J}/J = -2Hu \\ &\text{and} \;\; \dot{K} = 2KHu + (\tilde{b}^{\alpha\beta}u_{,\alpha})_{;\beta}, \end{aligned} \tag{3.36}$$

from chapter 2 in eq. (3.7) and employing Stokes' theorem, we compute the associated Euler-Lagrange equation

$$\frac{1}{2}[W_D(\lambda^\alpha\lambda^\beta - \mu^\alpha\mu^\beta)]_{;\beta\alpha} + \frac{1}{2}W_D(\lambda^\alpha\lambda^\beta - \mu^\alpha\mu^\beta)b_{\alpha\gamma}b^\gamma_\beta + \Delta(\frac{1}{2}W_H) + (W_K)_{;\beta\alpha}\tilde{b}^{\beta\alpha} + W_H(2H^2 - K) + 2H(KW_K - W) - 2H\lambda = p. \tag{3.37}$$

This is the modified *shape equation* in the context of anisotropic membranes. Suppressing the dependence of W on the curvature deviator D, yields the original shape equation for the isotropic lipid membranes [28, 26, 27, 18].

3.3.3 Edge conditions

With the Euler-Lagrange equations (3.31) and (3.37) satisfied, the variation of the energy E for a surface ω with a boundary $\partial\omega$ reduces to $\dot{E}_B = B_t + B_n$ where

$$B_t = \int_{\partial\omega}(W + \lambda)u^\alpha\nu_\alpha ds \tag{3.38}$$

and

$$B_n = \int_{\partial\omega}\Big[\frac{1}{2}(W_H - W_D)\nu^\alpha u_{,\alpha} - \frac{1}{2}((W_H)_{,\alpha} - (W_D)_{,\alpha})\nu^\alpha u + (W_K\tilde{b}^{\alpha\beta} + W_D\lambda^\alpha\lambda^\beta)\nu_\beta u_{,\alpha} - ((W_K)_{,\alpha}\tilde{b}^{\alpha\beta} + (W_D\lambda^\alpha\lambda^\beta)_{;\alpha})\nu_\beta u\Big]ds. \tag{3.39}$$

Similar to the derivation in chapter 2, we re-parameterize the surface at the edge in terms of arc length and normal to the edge. We define a vector $\boldsymbol{\tau}$ as the unit tangent to $\partial\omega$ as shown in Fig. 2.1 by taking the derivative with respect to arc length parameterizing the boundary $\partial\omega$, $\boldsymbol{\tau} = \frac{d\mathbf{r}(\theta^\alpha(s))}{ds}$. The unit normal to the boundary lying in the tangent plane to the surface can then be defined by the vector $\boldsymbol{\nu} = \boldsymbol{\tau} \times \mathbf{n}$. Using the orthonormality of $\boldsymbol{\nu}$ and $\boldsymbol{\tau}$, we can decompose the derivatives $u_{,\alpha}$ in (3.39) as $u_{,\alpha} = \tau_\alpha u' + \nu_\alpha u_{,\nu}$ where u' is the derivative along $\boldsymbol{\tau}$ in the direction of increasing arclength and $u_{,\nu}$ is the normal derivative along $\boldsymbol{\nu}$ [26].

We combine this with $u_{,\nu} = -\boldsymbol{\tau}\cdot\boldsymbol{\omega} - (\kappa_\nu \boldsymbol{\nu} + \tau\boldsymbol{\tau})\cdot\mathbf{u}$ and $u = \mathbf{u}\cdot\mathbf{n}$ to recast the edge contributions for a piecewise smooth boundary as

$$\begin{aligned}\dot{E}_B &= \int_{\partial\omega} (F_\nu \boldsymbol{\nu} + F_\tau \boldsymbol{\tau} + F_n \mathbf{n})\cdot\mathbf{u} ds - \int_{\partial\omega} M\boldsymbol{\tau}\cdot\boldsymbol{\omega} ds \\ &+ \sum_i \mathbf{f}_i \cdot \mathbf{u}_i,\end{aligned} \tag{3.40}$$

where

$$\begin{aligned} M &= \frac{1}{2}W_H + \kappa_\tau W_K + W_D \lambda^\alpha \lambda^\beta \nu_\beta \nu_\alpha - \frac{1}{2}W_D \\ F_\nu &= W + \lambda - \kappa_\nu M \\ F_\tau &= -\tau M \\ F_n &= (\tau W_K)' - \frac{1}{2}(W_H)_{,\nu} - (W_K)_{,\beta}\tilde{b}^{\alpha\beta}\nu_\alpha \\ &+ \frac{1}{2}(W_D)_{,\nu} - (W_D\lambda^\alpha\lambda^\beta)_{;\beta}\nu_\alpha - (W_D\lambda^\alpha\lambda^\beta\nu_\beta\tau_\alpha)' \\ \mathbf{f}_i &= (W_K[\tau] + W_D[\lambda^\alpha\lambda^\beta\nu_\beta\tau_\alpha])_i\mathbf{n}. \end{aligned} \tag{3.41}$$

Square brackets indicate forward jumps in values within the brackets at corners of the boundary, where there is a jump in $\boldsymbol{\tau}$. Above, M is the bending moment per unit length, F_ν is the in-plane normal force per unit length, F_τ is the in-plane shear force per unit length, F_n is the transverse shear force per unit length and $\mathbf{f}_i$ is the force applied at i th corner of $\partial\omega$. As expected, the anisotropic contribution to the strain energy results in modified expressions for the boundary forces and moment, furnishing an extension to the edge conditions derived for isotropic membranes [58, 59, 60, 61].

3.4 Example

In this section, we test the proposed theory by simulating the constriction of a cylindrical tubule by an exterior scaffold made of crescent shaped proteins, such as BAR protein dimers. To this end, we customize the equations derived in the previous section for axisymmetric surfaces parameterized by meridional arc

length s and azimuthal angle θ. For such a surface,

$$\mathbf{r}(s,\theta) = r(s)\mathbf{e}_r(\theta) + z(s)\mathbf{k}, \tag{3.42}$$

where $r(s)$ is the radius from axis of revolution, $z(s)$ is the elevation from a base plane and $(\mathbf{e}_r, \mathbf{e}_\theta, \mathbf{k})$ form the coordinate basis. Since $(r')^2 + (z')^2 = 1$, we can define an angle ψ such that

$$r'(s) = \cos\psi \quad \text{and} \quad z'(s) = \sin\psi. \tag{3.43}$$

Above and in the rest of the section, $()' = \partial()/\partial s$. With $\theta^1 = s$ and $\theta^2 = \theta$, we can easily show that

$$\begin{aligned} &\mathbf{a}_1 = r'\mathbf{e}_r + z'\mathbf{k}, \quad \mathbf{a}_2 = r\mathbf{e}_\theta \quad \text{and} \\ &\mathbf{n} = -\sin(\psi)\mathbf{e}_r + \cos(\psi)\mathbf{k}. \end{aligned} \tag{3.44}$$

Using (3.44) and its derivative, we can show that the metric $(a_{\alpha\beta}) = diag(1, r^2)$, the dual metric $(a^{\alpha\beta}) = diag(1, \frac{1}{r^2})$, and the covariant components of the curvature tensor $(b_{\alpha\beta}) = diag(\psi', r\sin\psi)$. Together they furnish the two invariants

$$2H = \psi' + \frac{\sin\psi}{r}, \quad \text{and} \quad K = H^2 - (H - (\sin\psi)/r)^2. \tag{3.45}$$

The BAR proteins align in a helical pattern on the membrane tubule [38]. The lateral and tip to tip interactions between the dimers help to deform the underlying membrane [51]. To achieve this efficiently, the BAR proteins maintain close proximity and orient themselves on the cylindrical surface with low tilt angle [37] (tilt with respect to the longitudinal axis of the tubule). Thus, for our simulations, we neglect the small tilt angle and assume a continuous distribution of crescent shaped dimers aligned in the circumferential direction. As a result, the two orientation vectors are given by

$$\boldsymbol{\lambda} = -\mathbf{e}_\theta, \quad \text{and} \quad \boldsymbol{\mu} = \cos\psi\mathbf{e}_r + \sin\psi\mathbf{k}. \tag{3.46}$$

The corresponding normal curvatures in the two directions become $\kappa_\lambda = (\sin\psi)/r$ and $\kappa_\mu = \psi'$. Together, they yield the curvature deviator $D = [(\sin\psi)/r - \psi']/2$.

We consider an extension of the Helfrich energy W that is quadratic in the mean curvature H and the curvature deviator D. For the time being, we suppress the dependence of W on the Gaussian curvature K as the influence of protein coat on the Gaussian modulus is not yet known. We discuss the possible consequences of different Gaussian moduli in Section 3.4.1. The generalized form of W can therefore be written as

$$\begin{aligned} W(H, D; s) &= \hat{k}_1(s)(H - H_0(s))^2 + \hat{k}_2(s)(D - D_0(s))^2 \\ &\quad + 2\hat{k}_{12}(s)(H - H_0(s))(D - D_0(s)), \end{aligned} \tag{3.47}$$

where $H_0(s)$ and $D_0(s)$ are the preferred H and D values that arise because of the anisotropic curvatures generated by the protein scaffold. In addition to the spontaneous curvatures, we assume the protein scaffold also alters the effective bending moduli and hence, allow them to vary spatially. In the absence of the protein coat, the last two terms vanish, furnishing the standard Helfrich energy. To get some additional insight into the membrane-protein system, we can express the above energy in terms of the normal curvatures in the $\boldsymbol{\lambda}$ and $\boldsymbol{\mu}$ directions in lieu of the mean curvature and the curvature deviator. With the help of $(3.3)_1$ and $(3.3)_3$, eq. (3.47) can be written as

$$\begin{aligned} W &= k_1(s)(\kappa_\lambda - \kappa_\lambda^0(s))^2 + k_2(s)(\kappa_\mu - \kappa_\mu^0(s))^2 \\ &\quad + 2k_{12}(s)(\kappa_\lambda - \kappa_\lambda^0(s))(\kappa_\mu - \kappa_\mu^0(s)). \end{aligned} \tag{3.48}$$

The link between the eqs. (3.47) and (3.48) is provided by the relations

$$\begin{aligned} &\hat{k}_1 = k_1 + k_2 + 2k_{12},\ \hat{k}_2 = k_1 + k_2 - 2k_{12}, \\ &\hat{k}_{12} = (k_1 - k_2), \\ &H_0 = (\kappa_\lambda^0 + \kappa_\mu^0)/2, \ \text{ and } \ D_0 = (\kappa_\lambda^0 - \kappa_\mu^0)/2. \end{aligned} \tag{3.49}$$

In eq. (3.48), $\{\kappa_\lambda^0, \kappa_\mu^0\}$ and $\{k_1, k_2\}$ are the spontaneous curvatures and the bending moduli along the directions $\boldsymbol{\lambda}$ and $\boldsymbol{\mu}$ and hence, provide a more intuitive picture of the effect of the protein scaffold on the membrane in the two directions.

The shape equation (3.37) for $W(H, D; s)$ and axisymmetric geometry reduces to

$$\begin{aligned} p = \frac{L'}{r} + W_H(2H^2 - K) - 2H(W + \lambda - W_D D) \\ + \frac{((W_D)' \cos\psi)}{r}, \end{aligned} \tag{3.50}$$

where

$$L/r = \frac{1}{2}[(W_H)' - (W_D)']. \tag{3.51}$$

The equilibrium equation in the tangent plane (eq. (2.41)) takes the form

$$\lambda' = -W'. \tag{3.52}$$

We account for the area incompressibility of the membrane by transforming the independent variable from arclength s to area a employing the relation $da/ds = 2\pi r$. In addition, we non-dimensionalize the system of equations and define

$$\begin{aligned} &\bar{r} = r/R_0,\ \bar{z} = z/R_0,\ \ \bar{a} = a/2\pi {R_0}^2,\ \bar{\kappa}_\lambda = R_0\kappa_\lambda, \\ &\bar{\kappa}_\mu = R_0\kappa_\mu,\ \bar{H} = R_0 H,\ \bar{D} = R_0 D,\ \bar{\lambda} = \lambda {R_0}^2/k_0, \\ &\bar{L} = R_0 L/k_0,\ \bar{k}_1 = \hat{k}_1/k_0,\ \bar{k}_2 = \hat{k}_2/k_0, \\ &\quad \text{and}\ \ \bar{k}_{12} = \hat{k}_{12}/k_0. \end{aligned} \tag{3.53}$$

where R_0 is a reference radius of curvature and k_0 is the bending modulus of the uncoated membrane.

The uncoated tubule has a uniform circumferential radius ($\bar{\kappa}_\lambda = 0.5$) with $\bar{k}_1 = 1$, $\bar{k}_2 = \bar{k}_{12} = 0$ and $\kappa^0_\lambda = \kappa^0_\mu = 0$. We simulate the shape evolution of the tubule for a sequence of non-uniform protein concentrations (C_1, C_2, C_3) shown in Fig. 3.3a. In a realistic setting such a changing spatial concentration would correspond to a binding-driven accumulation of the protein dimers. Since in the present study we do not explicitly model the self-assembly dynamics of dimers, we prescribe the protein concentration field a priori. We cap the concentration to a maximum value as the protein size and geometry would impose a physical restriction on the

packing density. We assume that the effective membrane parameters influenced by the protein coat ($\bar{H}_0, \bar{D}_0, \bar{k}_1, \bar{k}_2$) depend linearly on the protein concentration field (Fig 3.3b). A concentration dependent preferred curvature has indeed been experimentally observed for the BAR domain attachments [36].

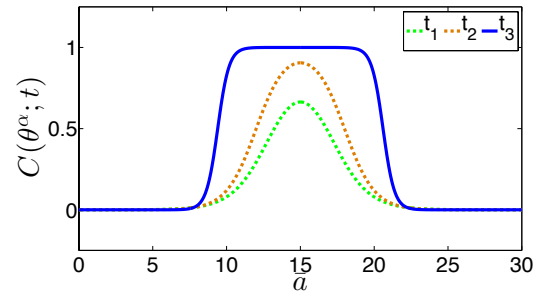

(a)

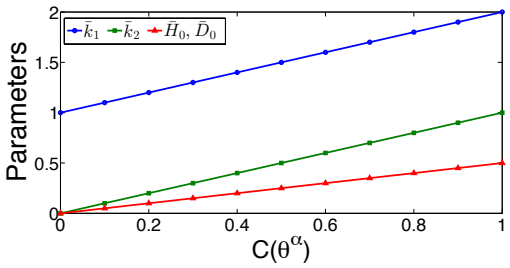

(b)

Figure 3.3: (a) Three prescribed spatially varying protein concentration fields, and (b) linear dependence of the various protein-induced parameters on the concentration values

We assume that the protein scaffold prefers a narrower tubule and prescribe a larger curvature ($\bar{\kappa}^0_\lambda = 1$) in the circumferential direction and zero curvature in the longitudinal direction ($\bar{\kappa}^0_\mu = 0$). In the (H, D) framework, these maximum directional curvatures transform to $\bar{H}_0 = 0.5$ and $\bar{D}_0 = 0.5$. These values correspond to the maximum protein concentration and get scaled by the local concentration values in the rest of the coated domain. In addition, we assume that the protein coat results in increased effective bending modulus and set $\hat{k}_1 = 2$, $\hat{k}_2 = 1$ in the highest concentration region. These parameters, computed from eq. (3.49),

assume a two times stiffening of the membrane in the $\boldsymbol{\lambda}$ and $\boldsymbol{\mu}$ directions. This choice of parameters is in agreement with a stiffness of $20 \pm 10\ k_B$T for the BAR proteins computed by the shape based coarse graining approach [46].

For the above mentioned parameters, we solve the differential equations (3.43), $(3.45)_1$, (3.50), (3.51) and (3.52) over an area domain varying from 0 to $\bar{a}_0 = 30$ for vanishing transmembrane pressure subject to the boundary conditions

$$\begin{aligned} &\bar{r}(0) = 2, \quad \bar{z}(0) = 0, \quad \psi(0) = \pi/2, \\ &\bar{r}(\bar{a}_0) = 2, \ \ \psi(\bar{a}_0) = \pi/2, \ \text{ and } \ \bar{\lambda}(\bar{a}_0) = 1/16. \end{aligned} \tag{3.54}$$

The last boundary condition is obtained from the solution of the standard shape equation to maintain the original cylindrical geometry far away from the protein coat domain.

The computed tubule geometry and the surface tension field are shown in Fig 3.4. As the protein coat continues to grow, the preferred circumferential and meridional curvatures are effectively imposed and the tubule attains a smaller radius in the coated domain (Fig. 3.4a). It is important to note that the changes in the geometry are accompanied by a concomitant change in the surface tension values shown in Fig. 3.4b. The surface tension profile closely follows the concentration profile. From a far away normalized resting tension of 0.06, the surface tension increases to 0.27 in the protein coat domain (for C_3 concentration field) leading to an approximate increase by 450%. Such a drastic change in the surface tension would be specifically relevant to comprehend the role and energetics of fission proteins that form cylindrical coats. The role of the tangential equilibrium equation in capturing the spatial variation in the surface tension can thus not be undermined.

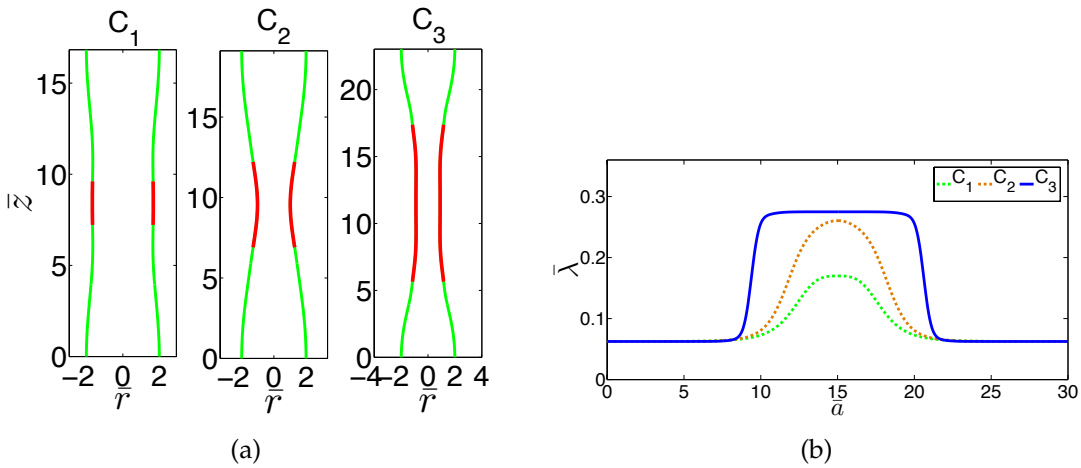

(a) (b)

Figure 3.4: (a) Tubule shapes for the three concentration fields. Red curve is the protein coated segment while the green curve is the uncoated segment. (b) Surface tension field for the three geometries.

3.4.1 Effect of Gaussian modulus

In the results presented so far, we have suppressed the role of Gaussian energy because of lack of experimental/numerical data on an estimate of the Gaussian modulus in the protein-coated domain. If the modulus remains unaffected by the scaffold, which appears rather non-intuitive, the equilibrium equations and the boundary conditions remain unchanged and the results presented before hold. If the modulus changes spatially, like the other bending moduli, it would affect both the geometry and the membrane stresses. To get a quantitative insight into this effect, we revisit the tubule problem with a modified strain energy $\bar{W}(H, D, K; s) = W(H, D; s) + \bar{k}(s)(K - K_0(s))$, where the first term is the energy in eq. 3.47 and the second term is the contribution from the Gaussian curvature. Since crescent shaped dimers prefer a cylindrical geometry, we set $K_0(s) = 0$. In the uncoated domain, we set $\bar{k} = -k_0$ based on the recent findings of Deserno and co-workers [62]. In the protein-coated domain, we perform a parametric analysis and compute the equilibrium solution for a few different values of $\bar{k}$. A

similar approach was adopted by Das et al. to model the impact of Gaussian modulus on the geometry of a membrane with two distinct phases of lipids [63]. Since the constraint on the Gaussian modulus from the stability condition is not known for anisotropic membranes at present and will be a subject of future study, we allow the modulus to span both the positive and the negative regimes. The tubule shapes and the membrane tension variations for three specific values of maximum $\bar{k}$ ($\bar{k} = k_0, -k_0, -3k_0$) corresponding to the C_3 concentration field are shown in Fig. 3.5. The changes in the overall geometry are rather subtle with minor variations occurring near the membrane-coat interface. The changes in the membrane tension, however, appear more significant, especially for the positive value of the modulus. Overall, the variations in the Gaussian modulus do not alter the qualitative response of the tubule.

3.5 Conclusions

We have derived the generalized theory for lipid membranes that interact with protein scaffolds inducing anisotropic spontaneous curvatures. In addition to the mean curvature and Gaussian curvature, the strain energy for a membrane interacting with a protein scaffold with orthotropic symmetry depends on the curvature deviator. Inclusion of this new invariant alters both the equilibrium equations and the edge conditions as shown in this paper. The proposed theory is equipped to model various kinds of spatial heterogeneities that may arise because of the membrane-protein interactions. We show the efficacy of the theory by modeling squeezing of a tubule by crescent shaped proteins. We emphasize the role of the equilibrium equation in the tangential plane by evaluating the surface tension field on the surface and showing its non-uniform behavior. Since membrane tension is a critical player in several cellular processes and remains

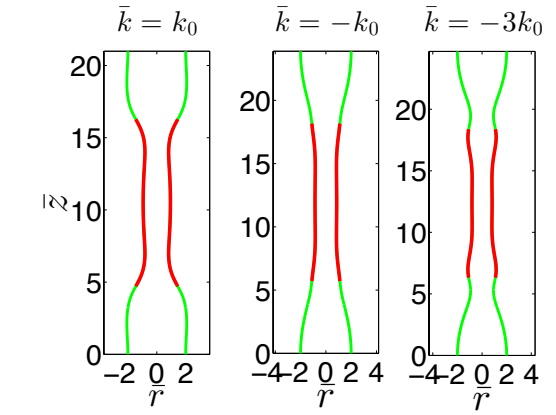

(a)

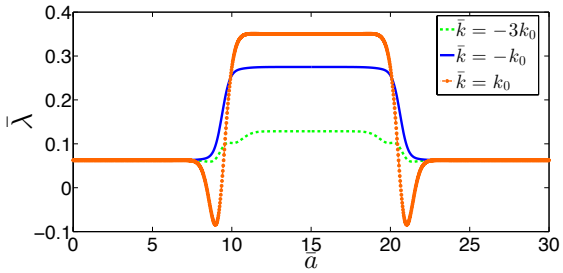

(b)

Figure 3.5: (a) Tubule shapes for the three prescribed Gaussian moduli for C_3 concentration field. Red curve is the protein coated segment while the green curve is the uncoated segment. (b) Surface tension field for the three geometries.

an enigma in experimental studies, modeling-based quantitative estimates of tension can prove to be of vital importance. We model the influence of Gaussian modulus on the equilibrium geometry and the membrane tension. Although the influence of protein-coat on the modulus is unknown at present, comparison of the experimental data on tubule shapes with the simulation results might provide an avenue to gain insight into the nature of the modulus.

Overall, the proposed framework would be valuable in comprehending biological phenomena where membrane-protein scaffold interactions play an important role. This bears special relevance for modeling of endocytic pathways in yeast and mammalian cells as cylindrical protein coats play a critical role in both

vesicle formation and fission. Lack of an apt mathematical framework may lead to erroneous conclusions about the need and roles of different components of the endocytic machinery. In addition, the proposed framework would form the basis for formulating a dynamic model to capture self-assembly of such proteins on a curved surface. This would be critical for understanding curvature-based protein sorting and localization in cellular membranes.

Chapter 4 Endocytic protein drive vesicle growth via Snap through Instability

4.1 Introduction

As discussed in Chapter 1, CME entails significant local bending of the membrane, transforming an almost planar patch of a bilayer into a spherical vesicle. This makes CME highly sensitive to the resting tension in the membrane. A higher tension in a membrane makes a membrane taut, making it harder to bend, thus, increasing the energetic cost required to form new vesicles. As a consequence, in cells experiencing high membrane tension, such as yeast cells and mammalian cells with polarized domains or those subjected to increased tension, actin dynamics has been found to be necessary to provide additional driving force to successfully complete CME [11, 16, 64, 65, 66, 67, 68]. Although this fact has been established by seminal experimental studies, how actin forces actually drive vesicle formation and can facilitate vesicle scission are not well understood. In addition, the role of another key membrane remodeling protein- the BAR protein, in overcoming tension has not yet been explored. In this chapter, we pursue a detailed theoretical and computational analysis to unravel some new mechanisms by which these key endocytic proteins (actin and BAR proteins) offset membrane tension, drive vesicle growth and assist vesicle scission.

We begin by posing a conundrum. In yeast cells, clathrin, actin and BAR proteins contribute to vesicle formation in different capacities. While the inhibition of actin polymerization completely arrests endocytosis [16, 65, 67, 68], the absence of clathrin and BAR proteins only leads to about 50% and 25% reduction in the

internalization events, respectively [7, 16, 69, 70, 71]. Although a high scission rate is maintained in BAR mutant cells, there is a fundamental difference between the shape evolution process in these and the wild-type cells. In the wild-type cells, a shallow invagination turns into an elongated vesicle with a constricted neck prior to scission which is successfully imaged in experimental studies (Fig. 4.1) [7, 16, 72]. In contrast, such an intermediate shape is not observed in BAR mutant cells. After a shallow and broad invagination, experimental images are only able to capture detached vesicles in the cytoplasm (Fig. 4.1 where lipid membrane is shown in yellow, clathrin coat in red, actin filaments in blue, and BAR coat in green) [7]. This is rather intriguing as the existing model of membrane scission requires lipids to come in close proximity and pass through a hemifission state prior to scission to avoid any leak during the topological transition [73, 74, 75, 76]. How then does a shallow invagination directly transform into a detached vesicle? We will show in later sections that this conundrum is at the core of the shape-evolution mechanism in the presence of resting tension in the plasma membrane and is critical for understanding the roles of actin and BAR proteins in CME.

Several theoretical and computational studies have advanced our physical understanding of CME in both mammalian and yeast cells [28, 77, 78, 79]. Liu et al. [77] studied vesicle formation and scission in yeast cells under the action of curvature-generating proteins and actin filaments. The study highlighted a critical role of lipid phase boundary-induced line tension in budding and scission. In a follow-up work, temporal and spatial coordination of endocytic proteins was studied in an integrated model to simulate endocytosis in mammalian and yeast cells [78]. The study showed a dynamic two-way coupling between the membrane geometry and the various biochemical reactions. Agrawal and Steigmann [28], employed a unified theory of heterogeneous membrane to show that clathrin coat could drive vesicle formation without assistance from line tension in the

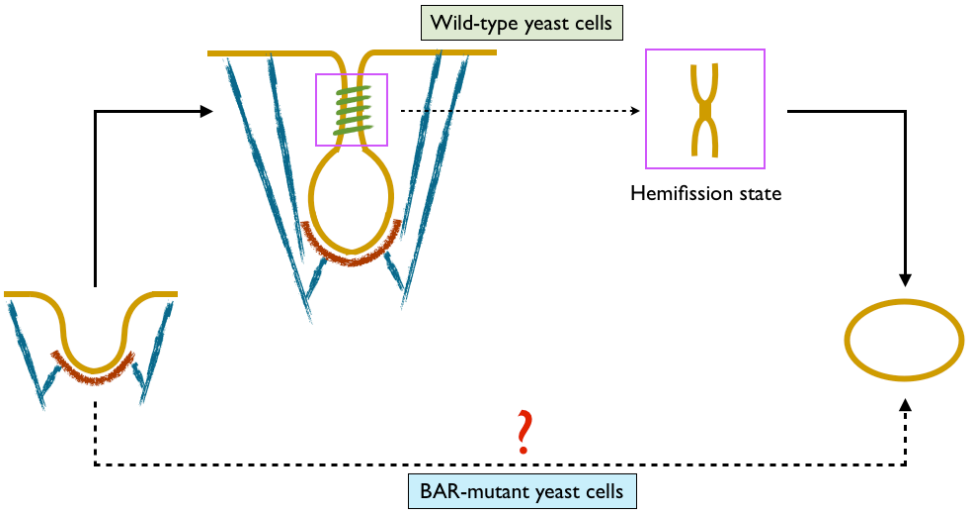

Figure 4.1: In wild type yeast cells, actin and BAR proteins turn a shallow invagination into a mature vesicle with a tubular neck. In BAR mutant yeast cells, the intermediate vesicle with a constricted neck is not observed.

absence of a resting plasma membrane tension. Agrawal et al. studied the roles of epsin and clathrin in the nucleation of membrane vesicles [79]. Although these studies have provided fundamental mechanistic insights into CME, the physical underpinnings of the remodeling mechanism in the presence of tension and the specific roles played by key proteins in countering tension remain unaddressed.

In this study, we simulate membrane-protein interactions at the continuum scale to explore the consequences of finite tension. We first model the effect of actin forces in driving the growth of a shallow clathrin-coated vesicle. We find that until a critical force is reached, the vesicle undergoes smooth transition. Once the critical force is crossed, it experiences a snap-through transition that drastically elongates and squeezes the vesicle. This leads to a significant in-plane stress in the tubular region of the vesicle that far exceeds the rupture tension. We then model the effect of BAR proteins. We find that the attachment of BAR proteins also drives vesicle formation by instability but it is much more gentle compared to the actin case. To our surprise, we find that after the instability has

occurred, the dissociation of BAR proteins leads to a larger elongation and growth of the vesicle. We predict vesicle shapes at different stages of CME which closely match those observed experimentally in yeast cells. To test the in-plane stress as a criterion for membrane scission, we simulate the geometries of detached vesicles. We find that the vesicles in the actin-driven case (in the absence of BAR proteins) are smaller than the vesicles in the BAR-driven case. In the latter case, the BAR proteins end up in the vesicle along with the clathrin coat as observed in [7]. We finally show that the membrane tension is the key parameter that regulates vesicle morphology.

4.2 The Model

The central feature of our model is that it incorporates protein-induced heterogeneities in the membrane in a seamless manner. As was shown in [28, 89], this generalization has a crucial consequence. It breaks down the well known requirement that the surface tension has to be uniform in the entire membrane, as is the case for a homogenous membrane. This feature is very pertinent as tension and its impact on membrane remodeling are at the center of this study. The fact that non-uniform tension can exist in the plasma membrane of cells is supported by experimental studies. The tension-based variation in the roles of actin-dynamics on the apical and basolateral surfaces of polarized MDHK cells [11] unambiguously shows that the tensions in the two parts of the same plasma membrane are different. It is, therefore, extremely crucial to capture the local variations in surface tension by allowing for heterogeneities in the membrane in order to model all the nuances of the membrane-protein interactions and their effect on membrane geometry. An overview of the key physical concepts that govern membrane-protein energetics is discussed next.

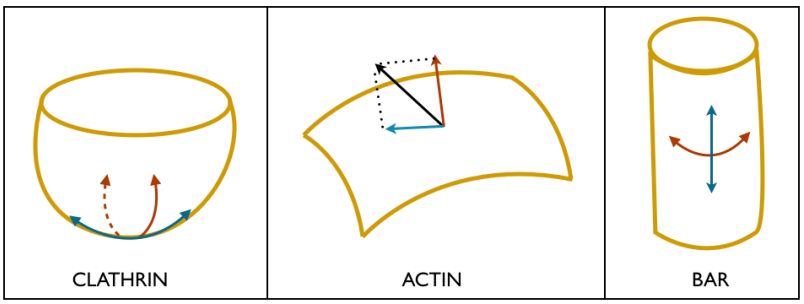

(a)

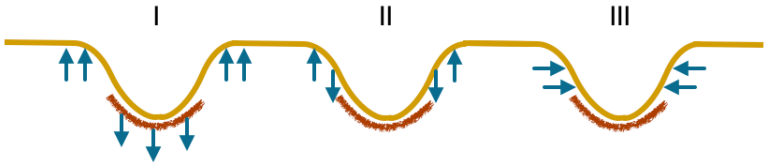

(b)

Figure 4.2: (a) Remodeling mechanisms of the three key endocytic proteins. Clathrin coat imposes spherical geometry, actin filaments apply forces and BAR imposes cylindrical geometry onto a lipid bilayer.

i) Lipid Membrane: The lipid bilayer is modeled as a two-dimensional surface embedded in three dimensional space. Since a relative misalignment of the lipids costs energy, a bilayer offers flexural stiffness. For an isotropic fluid bilayer, the areal strain energy density depends on the local mean curvature (H) and the Gaussian curvature (K) of the surface [5, 18, 19, 23, 29, 90]. For our model, we employ the well known Helfrich-Canham energy density, $W = k_B H^2 + \bar{k} K$, where k_B and $\bar{k}$ are the bending moduli. The values of these parameters and those discussed later are presented in Table 4.1. Since a lipid bilayer sustains a very small areal dilation (less than 2-3%) [5, 20, 29], we assume that any arbitrary patch on the bilayer surface maintains its area. This results in a Lagrange multiplier field λ, which is well known as the surface tension in the membrane. (Reader is referred to Table 2.1 for notations)

ii) Clathrin coat: Tri-legged proteins, called triskelions, assemble to form a clathrin scaffold that imparts a spherical geometry to the underlying bilayer (Fig.

4.2a). The preferred mean curvature of the sphere, called the 'spontaneous curvature', is isotropic in nature. In other words, the curvature induced by clathrin is identical in all the directions in the tangent plane at any point on the coated membrane surface. In addition to curvature generation, clathrin scaffold also stiffens the membrane resulting in an increase in the bending moduli of the coated domain [82]. These effects manifest themselves in the form of a modified strain energy density $W = \hat{k}_B(H - H_0)^2 + \hat{\bar{k}}K$, where H_0 is the spontaneous curvature and $\{\hat{k}_B, \hat{\bar{k}}\}$ are the modified bending moduli.

iii) Actin forces: Polymerizing actin filaments apply a force $\mathbf{f}$ on membrane invaginations. For a point on the surface with a unit surface normal $\mathbf{n}$, projection of $\mathbf{f}$ yields a normal component $(\mathbf{f} \cdot \mathbf{n})\mathbf{n}$ and an in-plane component $\mathbf{f} - (\mathbf{f} \cdot \mathbf{n})\mathbf{n}$ (red and blue arrows in Fig. 4.2a). Since the precise architecture of the actin network in the vicinity of the invagination and the resulting forces are not yet well established, we model a few different forcing scenarios shown in Fig. 4.2b. In the first case, we assume that the actin filaments form a branched network and are connected to a portion of the clathrin coat. Hip1R in mammalan cells and sla2p in yeast cells have been known to establish this clathrin-actin link [14, 91, 92]. We assume that the actin filaments apply a vertical distributed load on the invagination. This is inspired from the model proposed by Idrissi and coworkers [72] based on their ultrastructural analysis of endocytic profiles obtained using immunoelectron microscopy [68]. A similar model was found to be the most likely driving mechanism when the initial coat fails to deform the membrane significantly [8]. In the second case, we assume that the actin filaments form bundles that apply vertical forces on an annulus at the interface of the clathrin domain and the uncoated membrane. This model is aligned with the dendritic actin network with collar-like arrangement observed via high resolution platinum replica electron microscopy and electron tomography [93]. This is also in agreement with the

parallel bundled network scenario proposed by Drubin and co-workers [16] and used in the computational study by Liu et al. on yeast cells [78]. In the third case, we assume that the actin bundles apply inward acting horizontal forces near the base of the invagination. This loading condition has been discussed by Collins et al. [93] and Kirchhausen and co-workers [11] in the context of mammalian cells. For all the loading conditions, we assume that the downward acting forces are balanced by equal upward acting forces that impose global force equilibrium. This should be true in the real scenario as the actin network or bundle has to take support from some structure to apply forces on to the budding vesicle. A natural consequence of this condition is that it allows the parent bilayer to maintain planar geometry outside the remodeling domain as observed in experimental images.

iv) BAR coat: BAR dimers are crescent shaped proteins that bend the underlying bilayer by forming a cylindrical scaffold (Fig. 4.2a). Such a bilayer possesses local orthotropic symmetry and it's strain energy depends on an additional physical parameter D, referred to as the curvature deviator as shown in previous chapter. In addition, similar to the clathrin coat, the BAR coat also stiffens the membrane [51]. To incorporate these effects, we prescribe bending energy which has a quadratic dependence on D and a corresponding spontaneous curvature D_0. The resultant strain energy takes the form: $\mathrm{W} = \hat{k}_1(H - H_0)^2 + \hat{k}_2(D - D_0)^2 + \hat{k}_3 K$, where $\{\hat{k}_1, \hat{k}_2\}$ are the modified bending moduli and $\hat{k}_3$ is the modified Gaussian moduli.

We combine these contributions from the membrane and the endocytic proteins to construct the total free energy as,

$$E = E_b - E_f, \tag{4.1}$$

where,

$$E_b = \int_\omega [W + \lambda(\theta^\alpha)]da - pV(\omega), \tag{4.2}$$

and,

$$E_f = \int_{\omega_a} \rho \tilde{\mathbf{f}}(\theta^\alpha) \cdot (\mathbf{r} - \mathbf{r}_0)\, da = \int_{\Omega_a} \rho_0 \tilde{\mathbf{f}}(\theta^\alpha) \cdot (\mathbf{r} - \mathbf{r}_0)\, dA. \tag{4.3}$$

In the above equations, $\lambda(\theta^\alpha)$ represents the spatially varying Lagrange multiplier to prevent the local areal dilation and is termed as the surface tension field. p is the transmembrane pressure which is the Lagrange multiplier of V, the enclosed volume by the membrane patch ω being studied. For the evolution of shapes considered in simulations, the volume enclosed by an open patch of membrane is not conserved. The transmembrane pressure has been set to zero as it is an order lower than the pressure due to actin filaments. When the rupture stress is reached, equilibrium shape of the detached vesicle is obtained by preserving the detached area of lipid membrane and the volume enclosed by the vesicle. Moreover, it is assumed that the force per unit mass applied by the actin filaments, $\tilde{\mathbf{f}}$, is constant from the reference to the current configuration.

Table 4.1: Parameters used for simulations

Symbol	Significance	Value	Ref.
k_B	Bending Modulus of the bare lipid bilayer	20 k_BT	[80, 81]
$\hat{k}_B$	Bending modulus of the clathrin coated domain	200 k_BT	[82]
C	Preferred curvature of the clathrin coat	$1/50$ nm^{-1}	[83]
p	Transmembrane (Osmotic) pressure in the Yeast	1000 Pa	[84]
f	Max. force applied by the actin filaments	$100 - 200$ pN	[85, 86, 87]
f_0	Force intensity applied by the actin filaments	$< 2\text{x}10^5$ Pa	[85, 86, 87]
H_0	Preferred mean curvature of the BAR coat	$0 - (1/30)$ nm^{-1}	[48, 88]
D_0	Preferred deviatoric curvature of the BAR coat	$0 - (1/30)$ nm^{-1}	[48, 88]
$\hat{k}_1$	Mean curvature modulus of the BAR coat	0 - 200 k_BT	[51]
$\hat{k}_2$	Deviatoric curvature modulus of the BAR coat	0 - 200 k_BT	[51]

4.2.1 Variations

Variation of the total free energy of the membrane-protein system can be written as

$$\dot{E} = \dot{E}_b - \dot{E}_f, \tag{4.4}$$

where

$$\dot{E}_b = \int_\omega \dot{W} da + \int_\omega (W + \lambda)(\dot{J}/J)\, da - p\dot{V} \tag{4.5}$$

and

$$\begin{aligned} \dot{E}_f &= \int_{\Omega_a} \rho_0 \tilde{\mathbf{f}} \cdot \mathbf{u}\, dA \\ &= \int_{\omega_a} \mathbf{f} \cdot \mathbf{u}\, da. \end{aligned} \tag{4.6}$$

$J = \sqrt{a/A}$ is the ratio of the material area after and before the deformation. We obtain the equilibrium equations in the tangent plane,

$$\lambda_{,\eta} = -\partial W/\partial\theta^\eta - W_D(b_{\alpha\beta}(\lambda^\alpha\lambda^\beta)_{;\eta}) - \mathbf{f}\cdot\mathbf{a}_\eta, \tag{4.7}$$

and along the normal,

$$\begin{aligned} &\frac{1}{2}[W_D(\lambda^\alpha\lambda^\beta - \mu^\alpha\mu^\beta)]_{;\beta\alpha} + \frac{1}{2}W_D(\lambda^\alpha\lambda^\beta - \mu^\alpha\mu^\beta)b_{\alpha\gamma}b^\gamma_\beta + \Delta(\frac{1}{2}W_H) + (W_K)_{;\beta\alpha}\tilde{b}^{\beta\alpha} \\ &+ W_H(2H^2 - K) + 2H(KW_K - W) - 2H\lambda = p + \mathbf{f}\cdot\mathbf{n}. \end{aligned} \tag{4.8}$$

The in-plane component of the force intensity is added to the expression for spatial variation in tension field and the normal component of the force intensity gets added to the pressure when compared with equilibrium conditions obtained in (3.31) and (3.37). Since, the forces being applied by actin are distributed on the domain of the surface, they do not affect the boundary forces and moment derived in (3.41).

4.2.2 Axisymmetric Deformations

We assume that the deformations during membrane invaginations are axisymmetric. We simplify the equilibrium equations (4.7) and (4.8) for axisymmetric surfaces parameterized by meridional arc length $\theta^1 = s$ and azimuthal angle $\theta^2 = \phi$. For such a surface,

$$\mathbf{r}(s, \phi) = r(s)\mathbf{e}_r(\phi) + z(s)\mathbf{k}, \tag{4.9}$$

where $r(s)$ is the radius from axis of revolution, $z(s)$ is the elevation from a base plane and $(\mathbf{e}_r, \mathbf{e}_\phi, \mathbf{k})$ form the coordinate basis. Since $(r')^2 + (z')^2 = 1$, we can define an angle ψ such that

$$r'(s) = \cos\psi \quad \text{and} \quad z'(s) = \sin\psi. \tag{4.10}$$

In the above equations, superposed prime represents derivative with respect to arc length such that, $()' = \partial()/\partial s$. For BAR coated domain, we consider a continuous distribution of proteins on the surface with crescent shaped dimers aligned in the circumferential direction such that,

$$\boldsymbol{\lambda} = -\frac{1}{r}\mathbf{a}_2 = -\mathbf{e}_\phi =, \quad \boldsymbol{\mu} = \mathbf{a}_1 = \cos\psi\mathbf{e}_r + \sin\psi\mathbf{k}. \tag{4.11}$$

Same as the example solved in chapter 3, we obtain that

$$\begin{aligned} 2H &= \frac{\sin\psi}{r} + \psi', \\ 2D &= \frac{\sin\psi}{r} - \psi', \quad \text{and} \\ K &= H^2 - (H - (\sin\psi)/r)^2. \end{aligned} \tag{4.12}$$

The normal curvatures κ_λ and κ_μ are $(\sin\psi)/r$ and ψ' respectively. For this choice of $\boldsymbol{\lambda}$ and $\boldsymbol{\mu}$, the shape equation (4.8) for an axisymmetric geometry reduces to

$$p + \mathbf{f}\cdot\mathbf{n} = \frac{L'}{r} + W_H(2H^2 - K) - 2H(W + \lambda - W_D D) + \frac{((W_D)'\cos\psi)}{r}, \tag{4.13}$$

where

$$L/r = \frac{1}{2}[(W_H)' - (W_D)'] . \tag{4.14}$$

The equilibrium equation in the tangent plane (4.7) takes the form

$$\lambda' = -W' - \mathbf{f} \cdot \mathbf{a}_1 . \tag{4.15}$$

The above equilibrium equations (4.13), (4.14), and (4.15) remain valid even for the uncoated and the clathrin coated domain of the membrane as the effective membrane properties under the influence of clathrin and BAR proteins and the forces due to actin filaments, are specified via a hyperbolic tangent function (tanh) as shown in Fig. 4.3. This ensures continuity and differentiability of the strain energy density, W, at the interfaces of the protein coated membrane or the actin forcing domain. In order to maintain a control over the domains over which

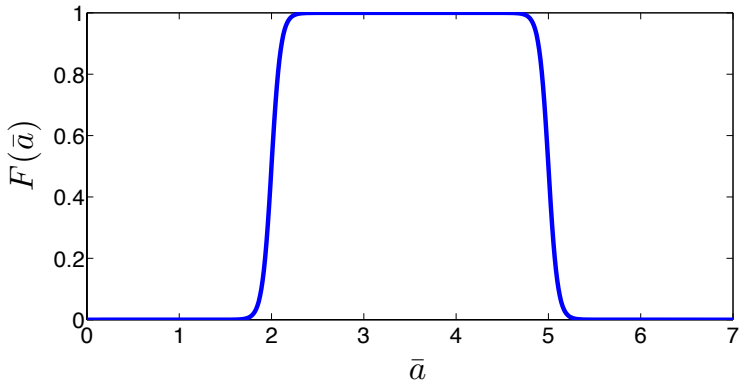

Figure 4.3: Function used to specify domains over which prescribed curvature and force fields generated key proteins are applied. F($\bar{a}$)= tanh [10($\bar{a} - \bar{a}_1$)] - tanh [10*($\bar{a} - \bar{a}_2$)] with $\bar{a}_1 = 2$, $\bar{a}_2 = 5$ (for illustration).

clathrin, actin and BAR proteins interact with the membrane, we transform the independent variable from arclength s to area a with by using the relation $da = 2\pi r ds$.

The strain energy density is considered of the form,

$$W = \hat{k}_1(a)(H - H_0(a))^2 + \hat{k}_2(a)(D - D_0(a))^2 . \tag{4.16}$$

In the clathrin coated domain $\hat{k}_1 = \hat{k}_B, \hat{k}_2 = 0$ and $D_0 = 0$.The above can also be written as

$$W = k_1(\kappa_\lambda - \kappa_\lambda^0)^2 + k_2(\kappa_\mu - \kappa_\mu^0)^2 + 2k_{12}(\kappa_\lambda - \kappa_\lambda^0)(\kappa_\mu - \kappa_\mu^0). \tag{4.17}$$

The bending moduli in the $\{H, D\}$ and the $\{\kappa_\lambda, \kappa_\mu\}$ framework are related by the following expressions $k_1 = k_2 = (\hat{k}_1 + \hat{k}_2)$ and $k_{12} = (\hat{k}_1 - \hat{k}_2)$. We have ignored the effect of Gaussian modulus by assuming that the associated modulus is constant in all the domains (clathrin coated, BAR coated and bare) of the lipid bilayer and the edge has zero geodesic curvature.

We non-dimensionalize the parameters used to define,

$$\begin{aligned}
&\bar{r} = r/R_0,\ \bar{z} = z/R_0,\ \ \bar{a} = a/2\pi {R_0}^2,\ \bar{\kappa}_\lambda = R_0\kappa_\lambda,\ \bar{W} = W{R_0}^2/k_0,\\
&\bar{\kappa}_\mu = R_0\kappa_\mu,\ \bar{H} = R_0 H,\ \bar{D} = R_0 D,\ \bar{K} = {R_0}^2 K,\ \bar{\lambda} = \lambda {R_0}^2/k_0,\\
&\bar{L} = R_0 L/k_0,\ \bar{k}_1 = \hat{k}_1/k_0,\ \bar{k}_2 = \hat{k}_2/k_0,\ \bar{p} = p{R_0}^3/k_0,\ \bar{\mathbf{f}} = ({R_0}^3/k_0)\mathbf{f}.
\end{aligned} \tag{4.18}$$

Here, $R_0 = 25\,nm$ is the normalizing radius of curvature and $k_0 = 20k_BT$ is the normalizing bending modulus. Using the above mentioned normalized parameters and defining the partial derivative with respect to $\bar{a}$, $\mathring{()} = \partial()/\partial\bar{a}$, the system of equations to be solved can be written as

$$\mathring{\bar{r}} = \sin\psi/\bar{r}, \quad \mathring{\bar{z}} = \cos\psi/\bar{r}, \tag{4.19}$$

$$\mathring{\psi} = \bar{\kappa}_\lambda/\bar{r}, \tag{4.20}$$

$$\bar{L}/\bar{r}^2 = \frac{1}{2}(\mathring{\bar{W}}_H - \mathring{\bar{W}}_D), \tag{4.21}$$

$$\mathring{\bar{L}} = \bar{p} + \bar{\mathbf{f}}\cdot\mathbf{n} - \bar{W}_H(2\bar{H}^2 - \bar{K}) + 2\bar{H}(\bar{W} + \bar{\lambda} - \bar{W}_D\bar{D}) - \mathring{\bar{W}}_D\cos\psi, \tag{4.22}$$

and

$$\mathring{\bar{\lambda}} = -\mathring{\bar{W}} - \bar{\mathbf{f}}\cdot\mathbf{a}_1. \tag{4.23}$$

In terms of the normalized principal curvatures, Eqs. (4.21)-(4.23) can be expressed as,

$$\begin{aligned}\mathring{\bar{L}} = &\Big(\bar{p} + \bar{\mathbf{f}}\cdot\mathbf{n} + (\bar{\kappa}_\lambda + \bar{\kappa}_\mu)(W + \bar{\lambda}) - 2\bar{\kappa}_\lambda^2[\bar{k}_1(\bar{\kappa}_\lambda - \bar{\kappa}_\lambda^0) + \bar{k}_{12}(\bar{\kappa}_\mu - \bar{\kappa}_\mu^0)] \\ &- 2\bar{\kappa}_\mu^2[\bar{k}_{12}(\bar{\kappa}_\lambda - \bar{\kappa}_\lambda^0) + \bar{k}_2(\bar{\kappa}_\mu - \bar{\kappa}_\mu^0)]\Big) - \mathring{W}_D\cos\psi,\end{aligned} \tag{4.24}$$

$$\mathring{\bar{\kappa}}_\lambda = \frac{(\cos\psi)\bar{\kappa}_\mu}{\bar{r}^2} - \frac{(\sin\psi\cos\psi)}{\bar{r}^3}, \tag{4.25}$$

and

$$\begin{aligned}\mathring{\bar{\lambda}} = -\Big(&\mathring{\bar{k}}_1(\bar{\kappa}_\lambda - \bar{\kappa}_\lambda^0)^2 - 2\bar{k}_1(\bar{\kappa}_\lambda - \bar{\kappa}_\lambda^0)\mathring{\bar{\kappa}}_\lambda^0 + \mathring{\bar{k}}_2(\bar{\kappa}_\mu - \bar{\kappa}_\mu^0)^2 - 2\bar{k}_2(\bar{\kappa}_\mu - \bar{\kappa}_\mu^0)\mathring{\bar{\kappa}}_\mu^0 \\ &+ 2\mathring{\bar{k}}_{12}(\bar{\kappa}_\lambda - \bar{\kappa}_\lambda^0)(\bar{\kappa}_\mu - \bar{\kappa}_\mu^0) - 2\bar{k}_{12}(\bar{\kappa}_\mu - \bar{\kappa}_\mu^0)\mathring{\bar{\kappa}}_\lambda^0 - 2\bar{k}_{12}(\bar{\kappa}_\lambda - \bar{\kappa}_\lambda^0)\mathring{\bar{\kappa}}_\mu^0\Big),\end{aligned} \tag{4.26}$$

where,

$$\begin{aligned}\mathring{W}_D = &(2\mathring{\bar{k}}_1 - 2\mathring{\bar{k}}_{12})(\bar{\kappa}_\lambda - \bar{\kappa}_\lambda^0) + (2\bar{k}_1 - 2\bar{k}_{12})(\mathring{\bar{\kappa}}_\lambda - \mathring{\bar{\kappa}}_\lambda^0) \\ &+ (2\mathring{\bar{k}}_{12} - 2\mathring{\bar{k}}_2)(\bar{\kappa}_\mu - \bar{\kappa}_\mu^0) + (2\bar{k}_{12} - 2\bar{k}_2)(\mathring{\bar{\kappa}}_\mu - \mathring{\bar{\kappa}}_\mu^0),\end{aligned} \tag{4.27}$$

and

$$\mathring{\bar{\kappa}}_\mu = \frac{\bar{L}}{2\bar{k}_2\bar{r}^2} + \mathring{\bar{\kappa}}_\mu^0 - \frac{\mathring{\bar{k}}_2}{k_2}(\bar{\kappa}_\mu - \bar{\kappa}_\mu^0) - \frac{\bar{k}_{12}}{k_2}(\mathring{\bar{\kappa}}_\lambda - \mathring{\bar{\kappa}}_\lambda^0) - \frac{\mathring{\bar{k}}_{12}}{k_2}(\bar{\kappa}_\lambda - \bar{\kappa}_\lambda^0). \tag{4.28}$$

The expressions for the boundary forces and moments reduce to (using (3.41)),

$$\begin{aligned}&\bar{F}_\tau = -\bar{\tau}\bar{M} = 0, \\ &\bar{M} = 2\bar{k}_2(\bar{\kappa}_\mu - \bar{\kappa}_\mu^0) + 2\bar{k}_{12}(\bar{\kappa}_\lambda - \bar{\kappa}_\lambda^0), \\ &\bar{F}_\nu = \bar{k}_1(\bar{\kappa}_\lambda - \bar{\kappa}_\lambda^0)^2 + \bar{k}_2(\bar{\kappa}_\mu - \bar{\kappa}_\mu^0)^2 + 2\bar{k}_{12}(\bar{\kappa}_\lambda - \bar{\kappa}_\lambda^0)(\bar{\kappa}_\mu - \bar{\kappa}_\mu^0) + \bar{\lambda} - \bar{\kappa}_\mu(2\bar{k}_2(\bar{\kappa}_\mu - \bar{\kappa}_\mu^0) \\ &\qquad + 2\bar{k}_{12}(\bar{\kappa}_\lambda - \bar{\kappa}_\lambda^0)), \\ &\bar{F}_n = -\bar{L}/\bar{r}.\end{aligned} \tag{4.29}$$

Boundary Conditions:

The system of equations to be solved comprises of six simultaneous ODE's (4.19), (4.20), (4.21), (4.22), and (4.23). We prescribe the following six boundary conditions at the two ends of the simulation domain as shown in Fig. 4.4, where **n** represents the normal vector to the surface. Parametrization of surface is done in terms of area rather than arc length to control the area over which clathrin and BAR proteins attach to the membrane and actin filaments apply force on the membrane. Directions of increasing area is represented with purple arrow while direction for increasing theta is represented in green.

i) For the near end at $\bar{a} = 0$

$$\bar{r} = 0, \quad \psi = 0 \quad \text{and} \quad \bar{L} = 0 \,(\text{due to reflection symmetry about z axis}) \tag{4.30}$$

ii) For the far end at $\bar{a} = \bar{a}_0$

$$\bar{z} = 0, \quad \psi = 0 \quad \text{and} \quad \bar{\lambda} = \bar{\lambda}_0 \,(\text{prescribed far end tension}) \tag{4.31}$$

The ODE's along with the boundary conditions are solved in Matlab using 'bvp4c solver'.

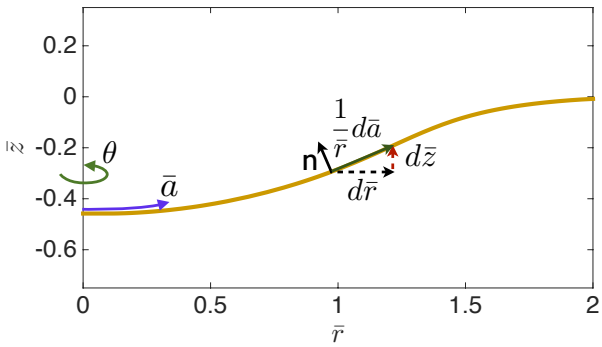

Figure 4.4: Simulation domain where the boundary conditions are prescribed at the end points ($\bar{a} = 0$, $\bar{a} = \bar{a}_0$).

4.3 Results

4.3.1 Actin forces drive membrane invagination via instability

We first present the actin-driven growth of a vesicle for loading case I (Fig. 4.2b) in the absence of BAR proteins. We assume an initial invagination has been created by a clathrin domain of 3200 nm^2. This estimate of coat size is based on the study of Kukulski et al. [7] in which clathrin was found to form a hemispherical coat on vesicles with an average size of 6400 nm^2. We assume that the resting tension in the membrane is 0.5 mN/m. This estimate is computed from the Young-Laplace relation based on an estimated turgor pressure of 1 KPa in yeast cells [84] which have an average cell diameter of one micron [96]. The vesicle shapes are computed in response to an increase in the intensity of the actin forces. Such an increase in the force intensity (force per unit area) is expected to arise from an increasing filament density which is observed experimentally in the vicinity of the vesicle [14]. Similar to Oster and co-workers [78], we neglect the pressure across the membrane as the force intensity due to actin is an order of magnitude higher than the osmotic pressure.

Fig. 4.5 presents our first key finding. The top row shows the vesicle morphology at three discrete stages of actin loading. As expected, the invagination grows as the actin force intensity is increased. The first shape is the initial invagination driven by the clathrin coat in the absence of actin forces (Fig. 4.5a). As the actin forces are increased, the invagination grows deeper reaching the geometry shown in Fig. 4.5b in a continuous manner. However, a further slight increase in the actin force leads to an unexpected shape change characterized by a drastic increase in vesicle length and a concurrent reduction in the tubule width (Fig. 4.5c). To gain insight into this discontinuous shape transition, we plot the force-deflection response of the vesicle (Fig. 4.5d). On the $y-$axis is the net vertical

downward force due to actin filaments and on the $x-$axis is the vertical distance of the tip of the vesicle from the initial flat configuration. The force-deflection curve exhibits a classic *snap-through instability* and comprises of three phases. In the first phase, the invagination grows monotonically as the force intensity is increased. This branch tracks shape evolution from the geometry in Fig. 4.5a to Fig. 4.5b. After reaching a peak force of about $190\,pN$, the system jumps to a point on the third linear branch with a much larger invagination length and positive slope. This represents the discontinuous transition from the shape in Fig. 4.5b to that in Fig. 4.5c while the intermediate shapes are skipped during the loading phase. The second branch with a negative slope is unstable and is never realized by the system. Such a force-deflection response with instability bears some similarity to that computed for a tether pulled out of a vesicle by a point force [97] as shown in Fig 4.6. However, unlike the force-deflection curve in Fig. 4.5, this response exhibits a horizontal third branch. As the pulling force is increased, the tether elongates linearly till it reaches a critical point, beyond which it undergoes a first order shape transition and continues to elongate at a constant force. Instability leading to morphological changes has also been observed in the context of closed vesicles. For example, Smith et al. simulated the unbinding of an adhered vesicle under the action of an applied point load and predicted a pathway that passes through metastable shapes characterized by discontinuous transition [98]. Agrawal and Steigmann showed that a closed vesicle with a preferred spontaneous curvature undergoes a snap-through transition when subjected to point loads [26].

The simulated shape just prior to instability is very similar to the shallow 50 nm invaginations observed in BAR (Rvs 161/167) mutant yeast cells by Briggs and co-workers [7]. In addition, the computed and experimentally measured angles between the membranes (defined in Fig. 4.7) during the shape evolution

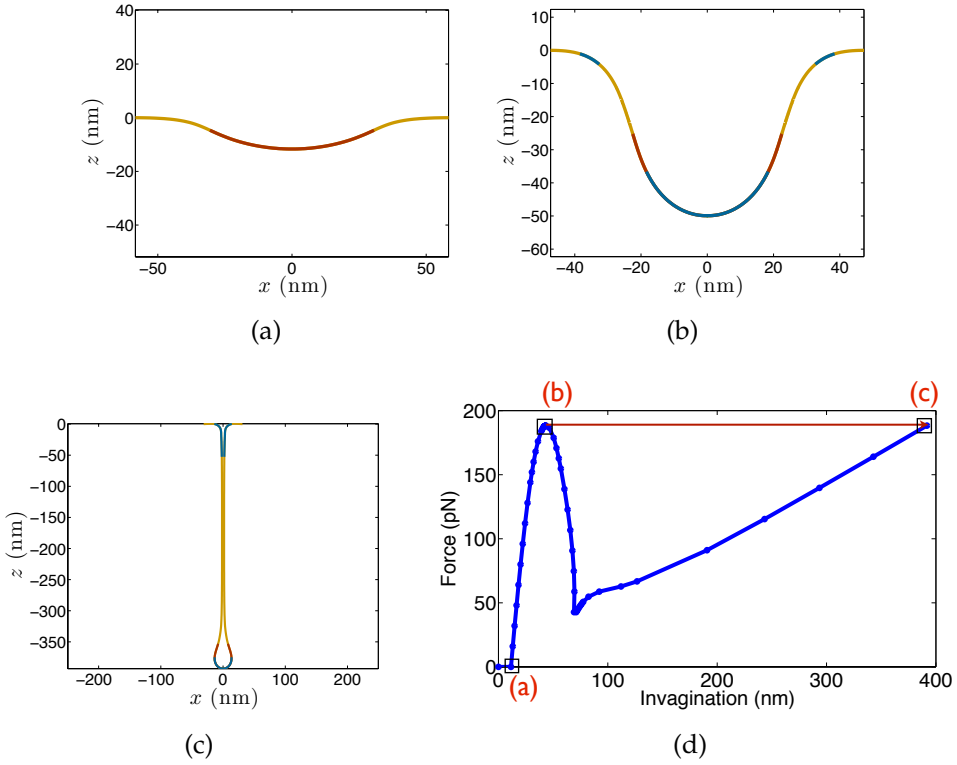

Figure 4.5: (a) Vesicle shape at vanishing actin force. (b) Vesicle shape prior to instability. (c) Vesicle shape post instability. (d) Force-deflection plot. The jump undergone by the vesicle is highlighted with a red arrow.

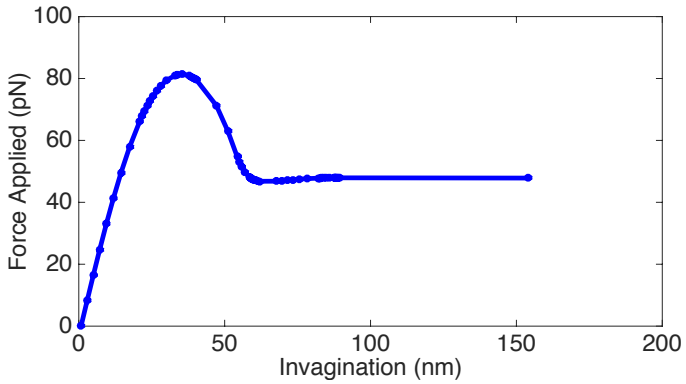

Figure 4.6: Force-deflection response in the absence of clathrin coat and counter forces in the planar membrane adjacent to the vesicle site. Resting tension in the membrane is 0.5 mN/m.

presented in Fig. 4.8 show a very good agreement. As the membranes become parallel for a cylindrical tubule and the ones where neck has formed, the angle becomes zero. In contrast, a highly elongated vesicle after the instability predicted by our model has not been experimentally observed in these BAR mutant cells. Instead, as mentioned earlier, the experiments report a detached vesicle directly after a shallow invagination. This leads to a natural question- why is the computed post-instability shape not seen in experiments? To investigate this issue, we compute the surface tension and the tangential stress in the vesicle as it undergoes shape evolution. It should be noted that unlike soap films, the net tangential stress in bilayer comprises of two components- the surface tension and the bending-induced stress. The stresses for the shapes just prior to and after instability are presented in Fig. 4.9. F_ν is the net in-plane stress and λ is the surface tension. The maximum tangential stress in the vesicle just before the snap-through transition reaches a value of 1 mN/m. After the transition, the in-plane stress increases to 17 mN/m. To get a sense of how high this stress is, we compute an average estimate of the lysis tension of a bilayer. Since a typical bilayer can withstand a maximum of about 3% areal strain and has an average stretch modulus of 250 mN/m [5, 20], it can endure a rupture stress of around 7.5 mN/m. The peak stress in the post-instability vesicle far exceeds this critical value and as a result, before the elongated vesicle is realized, the bilayer is likely to undergo rupture. Since the tubular domain is narrow ($\approx$ 5 nm in diameter), the lipids in the inner monolayer are adjacent to each other. This can allow a non-leaky scission to proceed via the hemifission state. Thus, a snap-through instability followed by a high stress-induced scission provides a mechanism by which shallow invaginations can end up directly as detached vesicles, providing a quantitatively tested answer to the mystery observed in BAR mutant yeast cells.

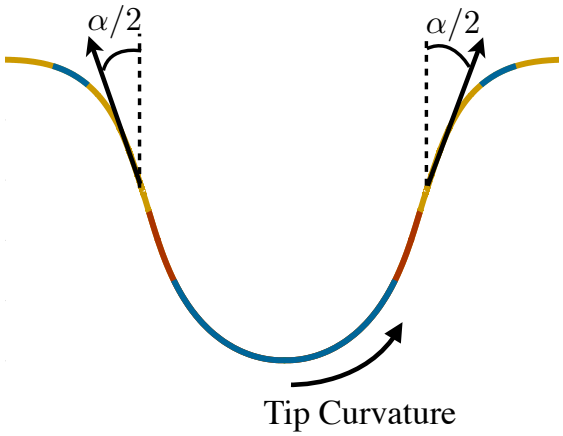

Figure 4.7: Tip curvature signifies normal curvature at tip in the tangential direction. Angle between the membranes is the minimum angle (α) between bilayers in the tubular domain. Definitions obtained from [7].

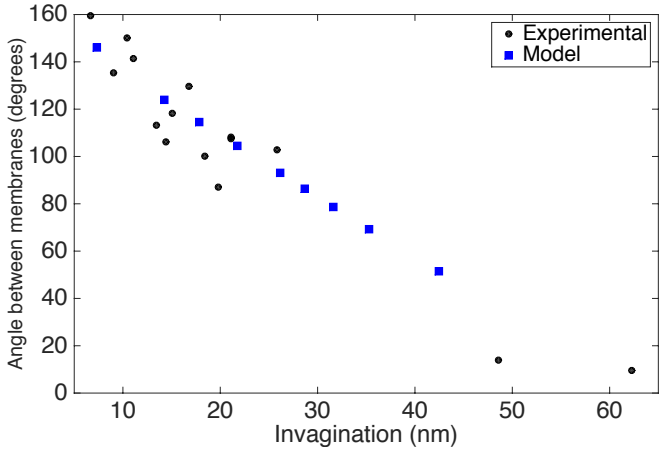

Figure 4.8: Variation of angle between membranes with invagination in Rvs 167 mutant case. Experimental data points are obtained from [7].

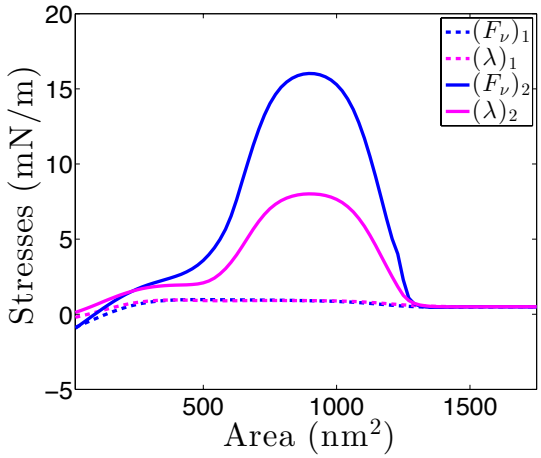

Figure 4.9: In-plane stress (F_ν) and surface tension (λ) in the vesicle just prior $()_1$ to and post $()_2$ instability. In-plane stress comprises of the surface tension and the bending-induced stress.

4.3.2 BAR proteins act as facilitators

We now simulate the effect of BAR coat proteins on shape evolution. To this end, we incorporate the effect of BAR proteins starting from an intermediate stage corresponding to a net vertical actin force that is lower than the critical force needed to induce snap-through transition. Here, we present the results for a net actin force of 160 pN (84% of the critical force value). To isolate the effect of BAR scaffold on vesicle growth, we hold the actin force and the clathrin domain fixed during the shape evolution. We follow the BAR dimer assembly trend observed in yeast cells characterized by two main phases- the polymerization phase where dimers self-assemble on actin-driven partial invaginations at a uniform rate, and the depolymerization phase, where they begin to dissociate at a uniform rate [78, 99]. This observed change in BAR concentration could be a consequence of either an increase in the areal density of the dimers, or an increase in the area over which polymerization has occurred, or both. For our simulations, we allow both the areal density and area of BAR-coated domain to increase and decrease simultaneously in the two phases (Fig. 4.10a). We further assume that

the BAR coat-induced curvatures and stiffnesses are linearly proportional to the dimer concentration. This assumption is based on the rationale that an increased proximity between the dimers would lead to a stronger lattice with enhanced remodeling capabilities. Such a behavior has been experimentally observed for amphiphysins that bind onto vesicles at dilute concentrations [100].

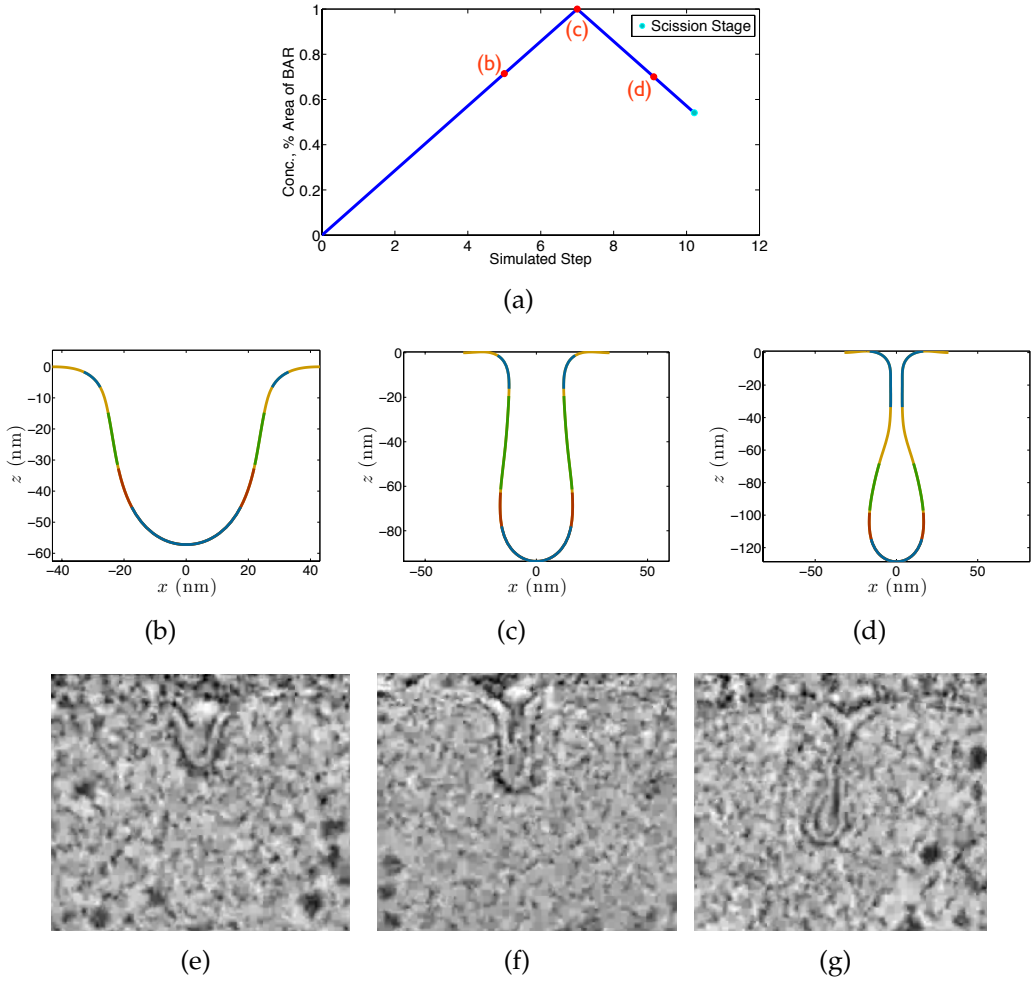

(a) (b) (c) (d) (e) (f) (g)

Figure 4.10: (a) Areal density and surface area of the BAR. Vesicle shapes during the (b)-(c): polymerization phase and the (d) depolymerization phase. (e)-(g) Observed vesicle shapes in wild-type yeasts [7].

Fig. 4.10 (b through g) shows our second key finding. In the BAR-driven case, the shape transition occurs in a more gradual and controlled fashion, in contrast to the rapid and discontinuous transition in the actin-driven case. This is

a consequence of the stabilizing effect of the BAR scaffold as it increases the flexural rigidity of the coated domain, thereby reducing it's compliance to bending. The BAR proteins transform the shallow invagination to a more U-shaped invagination as shown in Fig. 4.10b. An increase in the BAR density and area, leads to vesicle elongation and a narrowing of the neck domain (Fig. 4.10c). Once past this point, a decrease in the density and the area of the BAR coat has a counterintuitive impact on the vesicle morphology. Instead of decreasing the invagination, the removal of the BAR coat leads to a further elongation and narrowing of the vesicle (Fig. 4.10d). This irreversibility suggests that the vesicle again undergoes instability during the shape transition, this time triggered by the BAR scaffold. Thus, for a prescribed concentration (hence spontaneous curvatures and stiffness), and area of BAR proteins, there exist two vesicle geometries corresponding to the two branches (polymerization and depolymerization). The two solution branches meet at a unique set of BAR coat values. For the simulated case, this turning point corresponds to a preferred radius of curvature of 15 nm in the circumferential direction, bending moduli of $200k_BT$, and an area of attachment of 3700 nm^2. We compare the computed vesicle geometries with those observed by Briggs et al. for wild type yeast cells (Figs. 4.10e-g). The shapes show a remarkable agreement at three different stages of vesicle formation. In addition, we also see a very good agreement between a few other geometric parameters computed from our simulations and those measured by Briggs et al. which are presented in Figs. 4.11 and 4.12.

What makes the post-instability geometries in Fig. 4.10 experimentally tractable for visualization? To explain this, we again compute the stresses in the vesicle as it undergoes BAR-driven invagination. Unlike the highly invaginated vesicle in the actin-case, the in-plane stress for the shapes in Figs. 4.10b-d are well below the rupture limit making them stable structures that could potentially be imaged

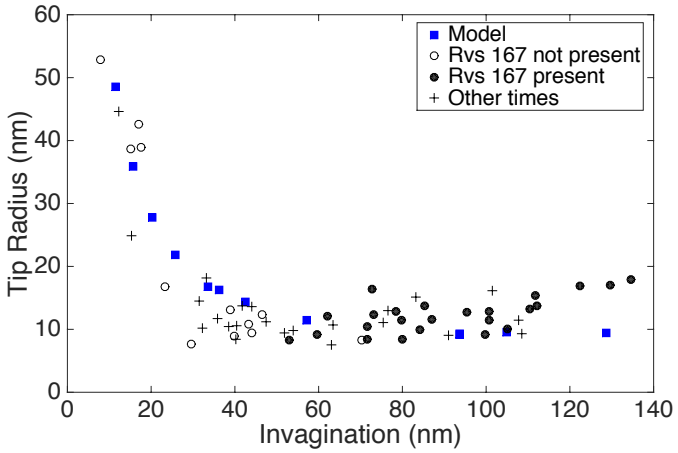

Figure 4.11: Variation of radius of curvature at tip of invagination in tangential direction (Fig 4.7) with invagination. The radius of curvature matches well with the experimental observations by Kukulski et. al [7].

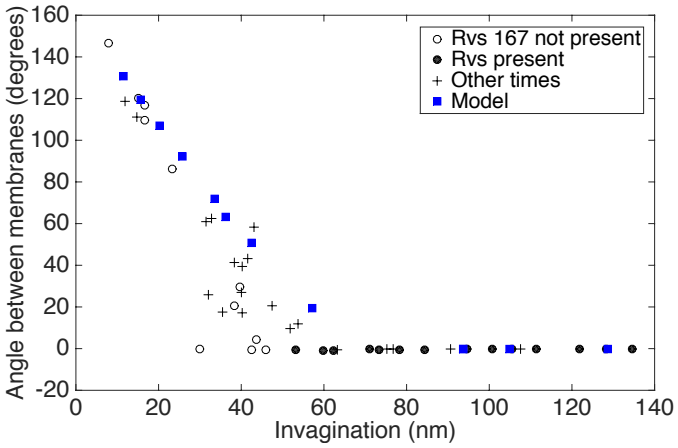

Figure 4.12: Variation of angle between membranes with invagination in the wild type case. Experimental data points are obtained from [7].

in experiments. If we continue to decrease the BAR density and the BAR domain size, we see enhanced elongation and narrowing of the tubule leading to higher internal stresses. Eventually, a shape is obtained for which the in-plane stress reaches the critical rupture stress (Fig. 4.13). All the intermediate shapes are therefore conducive to imaging and might be the reason for a variation in vesicle shapes observed in wild type yeast cells [7].

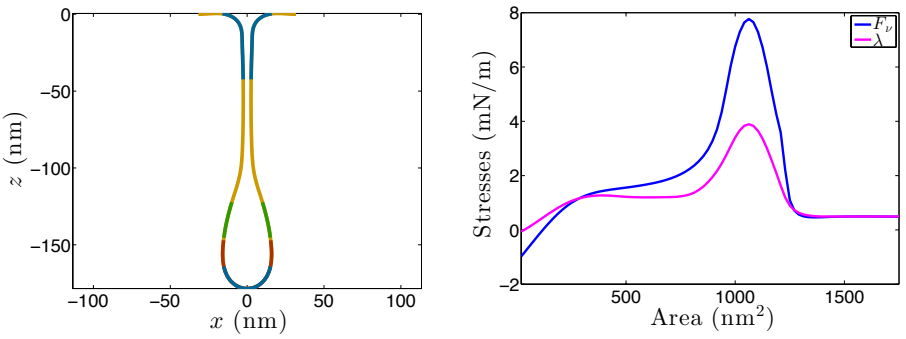

(a) (b)

Figure 4.13: Scission stage for BAR-driven invagination. (a) Vesicle shape, and (b) Membrane stresses. Total in-plane stress F_ν crosses the rupture stress of 7.5 mN/m.

4.3.3 Detached vesicle shapes support stress-based scission criterion

To further test the role of membrane stresses in CME, we simulate the geometry of detached vesicles for actin-driven and BAR-driven cases. Although scission is an intricate process in itself involving participation of special scission proteins or lipids, like dynamin in mammalian cells or PIP2 in yeast cells, we identify the probable sites for scission based on the in-plane stress profile. We hypothesize that the external work needed from scission proteins/lipids for executing membrane scission would be minimal at these sites. We therefore detach

the vesicle at the site of maximum in-plane stress and simulate the geometry of the closed vesicle. In addition, we constrain the area and volume of the detached membrane domain before and after scission. The geometries of the vesicles for the actin-driven and BAR-driven cases are shown in Fig. 4.14. Both vesicles exhibit a prolate geometry, unlike the nearly spherical vesicles observed in mammalian cells at low resting tension values. The vesicle in the actin-driven case possesses a more tear drop geometry. Interestingly, the vesicles observed by Briggs and co-workers in yeast cells also fall into two categories- tear dropped vesicles and prolate vesicles [7]. Their study also revealed a size variation in the wild type and BAR mutant cells. For the wild type cells, the vesicles had an average surface area of 6400 nm^2 and in the BAR mutant cells, the average size reduced to 5000 nm^2. These values are in excellent agreement with the computed vesicle sizes of 5500 nm^2 and 6480 nm^2 for the actin and BAR-driven cases, respectively based on the in-plane stress criterion. In addition to this match in overall vesicle geometry, our model makes another prediction that is aligned with an observation made by Kukulski et al. [7]. They found the detached vesicles to be coated with both clathrin and BAR proteins. This finding is different from the general notion that the detached vesicles are coated with just clathrin proteins. Our simulations support the findings of Kukulski et al. [7]. As the peak stress is reached at the interface of the BAR coat and the uncoated membrane tubule, the BAR coated domain, along with the clathrin-coated domain, becomes part of the detached vesicle. This match between the simulations and experimental data further bolsters the peak-stress based criterion for scission.

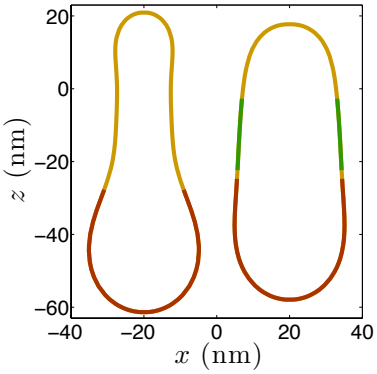

Figure 4.14: Detached vesicles obtained for the actin-driven (left) and BAR-driven (right) shape evolutions. The scission was assumed to occur at the site where the in-plane stress in the vesicle reaches the rupture stress.

4.4 Discussion

4.4.1 Actin-BAR synergy imparts robustness to the endocytic machinery

Our study on actin-driven vesicle growth predicts a net vertical force of about 190 pN for inducing instability at a resting tension of 0.5 mN/m (Figs. 4.5 and 4.15). In terms of force per actin filament, it amounts to an average force of approximately 2.4 pN which is distributed over an area of 1600 nm^2 in the clathrin-coated domain. This value is comparable to the compressive load required to buckle actin filaments obtained experimentally by Kovar et al. [87] and Footer et al. [86]. However, if the BAR proteins begin to polymerize before the critical actin force is reached, the instability could be induced sooner. In fact, BAR proteins establish a new transition pathway that connects the equilibrium solutions on the first and the third branches of the actin-driven force-deflection curve (Fig. 4.15). The BAR association phase (in cyan in Fig. 4.15) induces the instability and drives the initial membrane invagination. Once the instability has been triggered by the BAR proteins and the BAR proteins begin to dissociate, the vesicle has

a natural tendency to go to the equilibrium solution on the third branch of the force-deflection curve corresponding to the initial actin force at which the BAR proteins began to polymerize. Thus, once the BAR polymerization has tipped the system over, BAR disassembly reduces the stabilization effect of the scaffold and the vesicle growth becomes more actin-driven. It is for this reason that the disassembly of BAR proteins leads to larger elongation and tubulation of a vesicle.

The above discussion highlights a remarkable synergy between the actin and BAR proteins in driving vesicle growth. If we look at the above findings from a slightly different perspective, we can link the timing of the BAR activity to the functionality of the BAR proteins. Drubin and co-workers, for example, observed short phases of BAR polymerization and depolymerization after an initial phase of actin dynamics. Such a timing of the arrival of BAR proteins and their brief stay can now be seen to be more function-oriented than coincidental. The BAR proteins arrive after the actin forces set the stage and bring the system close to instability. The BAR proteins serve to tip the system over and depart, allowing instability driven transition to proceed. Thus, a short but well timed activity of BAR proteins is enough to drive vesicle growth and facilitate CME.

If we take this argument a step further, we can predict a domain over which actin and BAR proteins can synergistically drive vesicle growth (shaded area in Fig. 4.15). The upper limit of this domain is defined by the pure actin-driven path. To define a lower limit, we require the vesicle after BAR dissociation to experience rupture stress for successful completion of CME. For this pathway, the green domain represents BAR polymerization-dependent invagination and the cyan domain represents BAR depolymerization-driven invagination. The actin force required for this path is approximately 30% lower than the critical actin-force needed to induce instability in the absence of BAR proteins (double-sided vertical arrow). For any force above this threshold value and lower than the peak

force (shaded region in Fig. 4.15), actin and BAR can synergistically drive vesicle formation and set the stage for scission. This showcases an inherent robustness of the endocytic machinery where the two proteins can work together to complete CME. If, in addition to in-plane stresses, other scission effects, such as the line tension induced by PIP2, are at play, the actin force requirement would decrease further thereby expanding the domain of actin-BAR cooperativity. However, a certain actin force would always be needed to create an initial invagination on to which BAR dimers can polymerize making actin forces indispensable for CME in tense plasma membranes.

4.4.2 Tension differentiates CME in yeast and mammalian cells

Although membrane tension has been postulated to be an important factor leading to differences in yeast and mammalian cells, it has not yet been quantitatively examined. Mammalian cells on an average have a lower resting tension in the plasma membrane because of a lower turgor pressure [10]. The tension estimates vary from 0.003 mN/m in chick neurons [101] to 0.02 mN/m in molluscan neurons [102]. For the case of vanishing tension, clathrin-driven vesicle formation has been shown to reproduce the experimental findings [28]. For higher tension (0.5 mN/m), we have shown a good match between the simulations and the shape evolution in yeast cells [7, 16]. We now present the results for an intermediate value of 0.08 mN/m, and compare them with the experimental findings of [11] in mammalian cells subjected to increased tension generated by either osmotic swelling or stretching. In addition to lowering the resting tension value, we increase the clathrin coat size to 20,800 nm^2, which is in between the value used for yeast cells and that for a closed spherical coat (32000 nm^2 for a spherical vesicle of radius 50 nm) that would ideally form in low tension environment in mammalian cells.

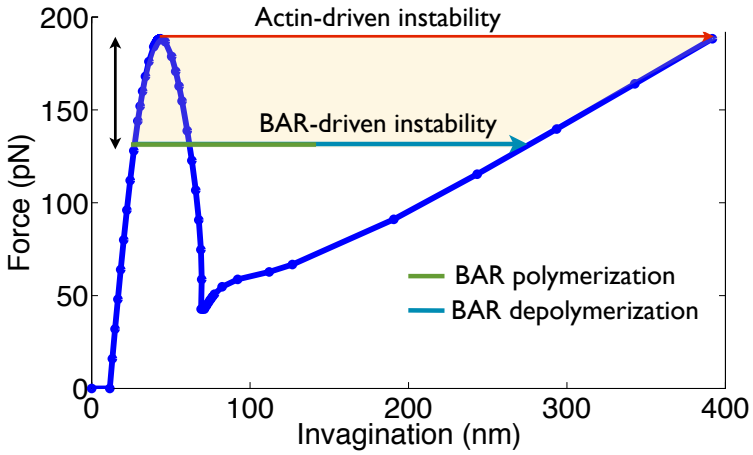

Figure 4.15: Synergistic roles of actin and BAR proteins in executing CME. Shaded region shows the domain over which final vesicle obtained after complete BAR dissociation experiences close to rupture stress.

The computed shapes with the above parameters are shown in Fig. 4.16. The shape in Fig. 4.16a corresponds to a clathrin-induced invagination in the absence of actin forces. It matches well with the stalled vesicles (Fig. 4.16b) observed by Boulant et al. [11]. The shape in Fig. 4.16c is obtained after the occurrence of the snap-through transition which bears resemblance to the mature vesicles observed by Boulant et al. [11] (Fig. 4.16d). The good agreement between the computed vesicle shapes at different tension values and those observed in yeast and mammalian cells provides quantitative evidence that tension indeed is a key factor that differentiates CME in the two cell types. The vesicle in Fig. 4.16c has a maximum in-plane stress of 0.46 mN/m, almost an order of magnitude less than the rupture tension, thereby, making it stable. We would like to note that vesicles with elongated tubular domains have also been observed in dynamin-mutant mammalian cells [103]. Since actin burst in mammalian cells (under low resting tension) occurs just prior to scission, our work suggests that actin forces lead to elongation of the vesicles but are unable to dissociate vesicles from the plasma membrane due to inadequate scission stress.

4.4.3 Tension governs vesicle morphology

If we generalize the actin-driven shape evolution studies to a wider range of tension values, we find that the vesicle geometry and the initiation and extent of discontinuous shape transition is a function of the resting tension in the membrane. Fig. 4.17a shows the critical force needed to induce instability as a function of the resting tension in the planar bilayer. These results have been obtained for a fixed clathrin coat size of 3200 nm^2. The critical force increases monotonically with an increase in the resting tension. This trend is aligned with the recent studies by Basu et al. [104] and Aghamohammadzadeh et al. [10] that found actin requirement to be proportional to the turgor pressure and hence, resting tension, in yeast cells. In addition, we compute the invagination length (Z_1, marked blue in Fig. 4.17) at the critical point prior to and after transition. An increase in tension reduces the initial invagination depth at which the snap-through transition occurs in a linear fashion (Fig. 9b). In contrast, the jump in the invagination length ($Z_2 - Z_1$, marked green in Fig. 4.17) increases almost linearly as the tension is ramped up. Elongation of vesicles is also accompanied with a narrowing of the width of the tubular domain. Thus, beyond a critical resting tension, invaginated vesicles after instability would experience significant in-plane stresses making them experimentally intractable until stabilized by BAR coat proteins. For a clathrin area of 3200 nm^2, we predict this critical value to be around 0.2 mN/m. These predictions can be tested in experiments by systematically varying tension in the plasma membrane, either by osmotic swelling or stretching, and imaging the vesicles.

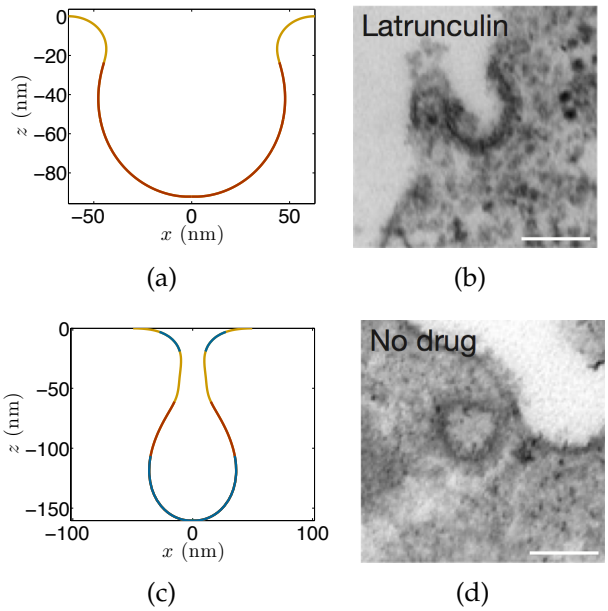

Figure 4.16: Vesicle shapes in (a) absence of actin, (b) MDCK cells subjected to increased tension and no actin [11], (c) presence of actin, (d) MDCK cells with increased tension [11]

4.4.4 Actin induced in-plane stress should be a key determinant of scission

Our study provides strong evidence that in-plane stress should play an integral role in governing membrane scission. Our explanation of the discontinuous transition observed in BAR mutant yeast cells and the vesicle shapes and sizes generated by our model support this prediction. Although other mechanisms have been implicated in scission, membrane stress could facilitate the topological transition and determine the site for membrane scission. For example, Oster et al. proposed the role of line tension in vesicle formation and scission in yeast cells [77]. The arrival of synaptojanin in the later stages hydrolyzes PIP2 in the clathrin coated domain giving rise to a line tension at the interface of the clathrin and BAR coated domains. However, it is important to note that even in the absence of BAR proteins, scission events occur in around 75-80 % of the endocytic

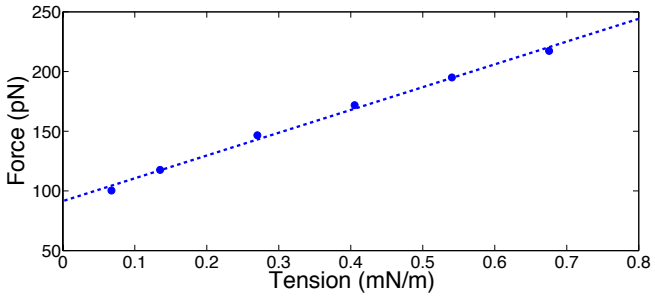

(a)

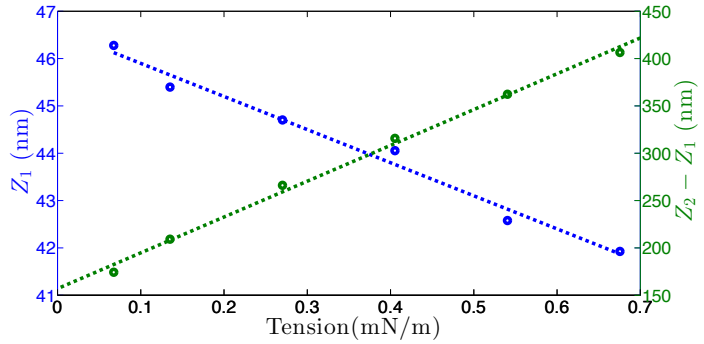

(b)

Figure 4.17: Effect of resting tension. (a) The critical actin force required to induce instability. (b) The invagination length prior to instability (Z_1) and the jump in the invagination length ($Z_2 - Z_1$)

events [7]. This alludes to a role of additional mechanisms in executing scission. We propose actin-induced in-plane stress to be a potential candidate. In wild type mammalian cells, since actin burst occurs in the latter part of endocytosis, actin-induced stress could assist dynamin in scission. In addition, actin-induced in-plane stress in the neck domain could facilitate dynamin polymerization [105]. This idea is supported by the recent work of Campelo et al. [106], which predicts that high stress facilitates insertion of shallow proteins within the bilayer. Thus, in-plane stress could act as a facilitator for dynamin-induced scission.

4.4.5 Limitations

The major limitation of our mathematical framework is that it is not equipped to model topological changes and hence, cannot be used to simulate vesicle scission. It is for this reason, the model predicts highly elongated vesicles after snap-through transition that would otherwise undergo scission. The other limitation of our study is that the actin loading scenarios modeled are based on the proposals made in the literature and might not be very accurate. However, the findings made above are true for both the distributed network and bundle type actin loadings (Cases I and II in Fig. 4.2b). Barring some minor quantitative differences, the overall nature of the force-deflection response of the vesicle remains unchanged for the first two cases (Fig. 4.18). This suggests that our predictions should hold for a wide variation in the actin loading mechanisms. Only the horizontal loading (Case III in Fig. 4.2b) requires a much higher actin force (almost twice), induces negative in-plane stress in the tubule region and leads to short spherical vesicles typically not seen in yeast cells (Fig. 4.18). These major differences indicate that a purely horizontal force driven vesicle formation is not likely to exist in the high tension regime. The shape evolutions for cases II and III are presented in Figs. 4.19 and 4.20.

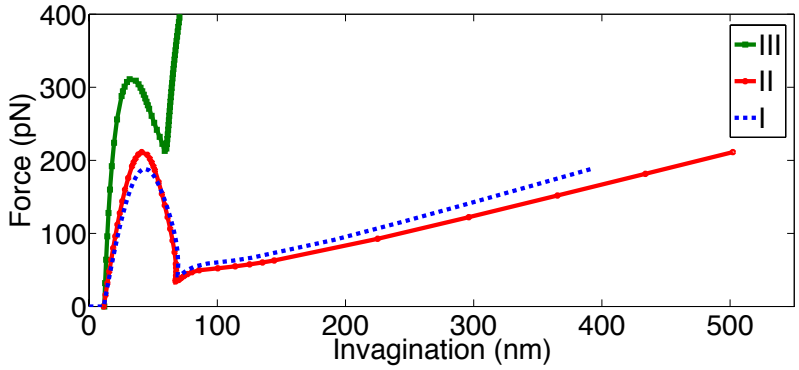

Figure 4.18: Force-deflection curves for the different actin loading cases presented in Fig. 4.2b. Cases I and II show similar response whereas Case III predicts smaller invaginations and larger forces to induce instability.

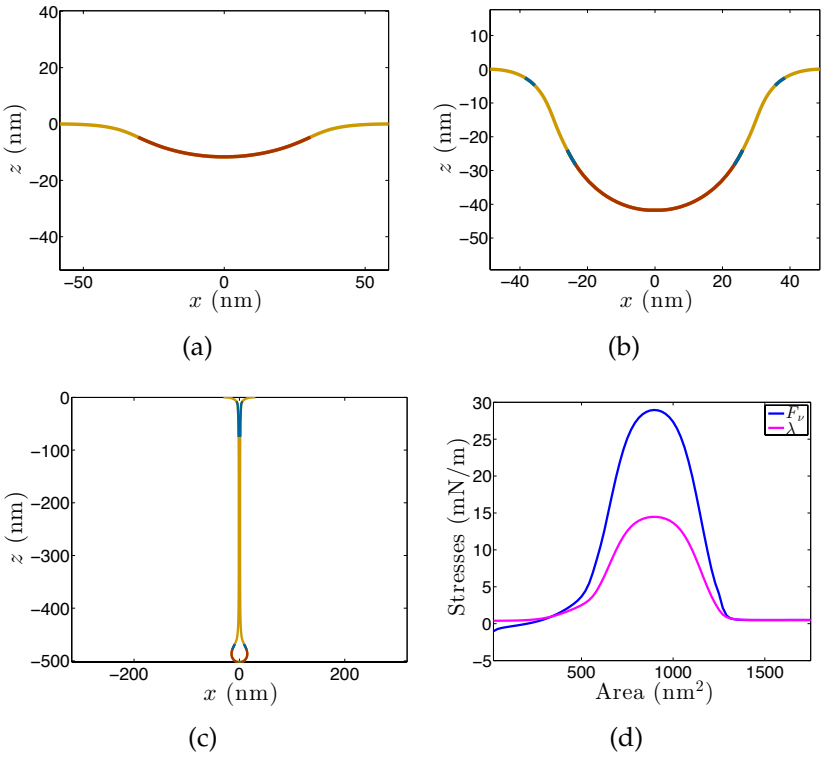

Figure 4.19: Actin-driven vesicle growth for actin loading II. (a)-(c) Vesicle shapes at different stages. (d) Stress profile for the shape after snap-through instability shown in (c). The behavior is almost similar to loading I.

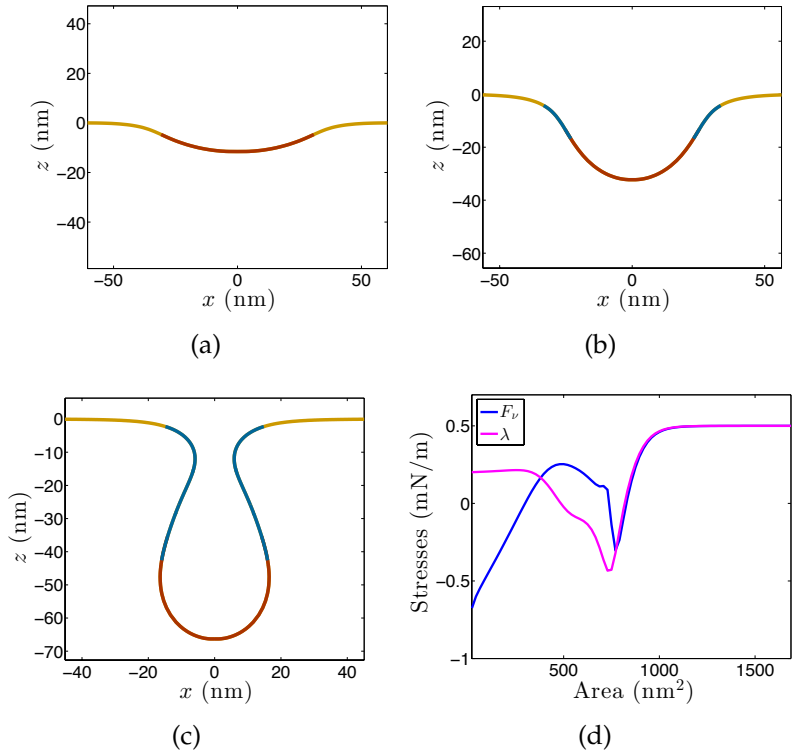

Figure 4.20: Actin-driven vesicle growth for actin loading III. (a)-(c) Vesicle shapes. (d) Stress profile for the shape after instability shown in (c). Peak stress in the tubular domain in (c) reaches only 0.25 mN/m.

Chapter 5 Stability of Lipid Membranes

5.1 Introduction

The lipid bilayers exhibit a wide variety of morphologies, ranging from spherical vesicles to spherocylindrical shapes in mitochondria to much more complex shapes in endoplasmic reticulum. These shapes undergo drastic changes in response to mechanical, electrical or thermal stimuli during numerous cellular processes [108, 109, 110], making it pertinent to study the stability of these versatile structures to model and comprehend their shape evolutions.

Several fundamental studies have investigated the stability of lipid membranes. A rigorous derivation of the second variation for homogenous membranes with quadratic strain energy (Helfrich-Canham energy) has been done in [112, 113, 114, 115, 116]. The stability analysis has been applied to investigate the shape transitions of spheres and cylinders. A classic example is the loss of stability in membrane tubules, known as Pearling instability [117, 118]. The stability of flat discs have been recently studied in the context of HDL (high density lipoproteins) [119] and disc-to-vesicle shape transition [120].

While the above studies have given fundamental insights into the stability of homogeneous membranes with quadratic energy, there is a need to extend the framework to study systems with heterogeneous properties and higher order bending energies. The impact of heterogeneity on equilibrium configurations has been revealed in [28, 89]. The effect of inhomogeneity-dependent instability was also shown to be a key factor in determining cellular transport via clathrin-mediated endocytosis in the previous chapter [121]. In addition, generalized strain energies have been used to study sorting of lipids [55, 122] (where stiffness of tubular membranes is observed to be a function of curvature) and phase

transitions [123]. In this context, the Legendre-Hadamard condition for stability of generalized fluidic shells was derived in [19, 123, 124] and the stability of fluidic surfaces with multiple phases was investigated in [125]. In this work, we extend the model to account for strain energy that can have arbitrary dependence on the mean curvature and Gaussian curvature. In addition, our model allows for material properties such as bending moduli or preferred curvatures to undergo spatial variation due to heterogeneities induced by lipid composition and/or protein interactions [28]. We note that stability in continuous systems is only defined with respect to a particular norm and choices of different norms could lead to different results regarding inferring the stability, the details of which have been discussed by Como and Grimaldi in [126]. We, as others, use the second Gateaux derivative of the energy functional to define the stability criteria. Thus, the stability is examined with respect to a weaker norm (also mentioned as the energy norm) for which the variations in the position and its higher order derivatives are assumed to be bounded.

5.2 The Variations

Let $\mathbf{r}(\theta^\alpha)$ be the position of a material point on the surface where θ^α are the surface coordinates that parametrize the surface. The tangent vectors at any point on the surface are given by $\mathbf{r}_{,\alpha} = \mathbf{a}_\alpha$. The strain energy density of an isotropic membrane depends on the mean curvature H and Gaussian curvature K as discussed in Chapter 2. Due to heterogeneities, the strain energy density can explicitly depend on θ^α [28]. In the presence of area and volume constrains, the energy of an isotropic membrane is given by

$$E = \int_\omega W(H, K; \theta^\alpha)\, da + \int_\omega \lambda(\theta^\alpha)\, da - pV(\omega), \tag{5.1}$$

where $\lambda(\theta^\alpha)$ is the local Lagrange multiplier associated with local area constraint commonly known as surface tension, p is the Lagrange multiplier associated with the volume constraint and is commonly referred to as the transmembrane pressure.

The variation of position vector is given by,

$$\dot{\mathbf{r}} = \mathbf{u} = u^\alpha \mathbf{a}_\alpha + u\mathbf{n}. \tag{5.2}$$

As derived in chapter 2, using (2.74), (2.89), (2.75) and (2.90), this yields the following variations of the first and second fundamental form,

$$\begin{aligned} \dot{a}_{\alpha\beta} &= u_{\alpha;\beta} + u_{\beta;\alpha} - 2ub_{\alpha\beta}, \\ \dot{b}_{\alpha\beta} &= u^\lambda_{;\alpha} b_{\lambda\beta} + u^\lambda_{;\beta} b_{\lambda\alpha} + u^\lambda b_{\lambda\alpha;\beta} + u_{;\alpha\beta} - ub_{\alpha\lambda} b^{\lambda\beta}. \end{aligned} \tag{5.3}$$

Using the above relations, the variations of the mean curvature, Gaussian curvature and scalar J, can be computed to be,

$$\begin{aligned} \dot{H} &= u^\alpha H_{,\alpha} + \frac{1}{2}(\Delta u) + u(2H^2 - K), \\ \dot{K} &= u^\alpha K_{,\alpha} + 2HKu + \tilde{b}^{\alpha\beta} u_{;\alpha\beta}, \quad \text{and} \\ \frac{\dot{J}}{J} &= u^\alpha_{;\alpha} - 2uH. \end{aligned} \tag{5.4}$$

With the help of these variations and the procedure outlined in chapter 2, the first variation of E can be expressed as

$$\dot{E} = \int_\omega \left\{ -u^\alpha \left(\lambda_{,\alpha} + \frac{\partial W}{\partial \theta^\alpha} \right) + uG \right\} da, \tag{5.5}$$

where

$$G = \frac{1}{2}\Delta W_H + (W_K)_{;\alpha\beta}\tilde{b}^{\alpha\beta} + W_H(2H^2 - K) + 2H(KW_K - W) - 2H\lambda - p. \tag{5.6}$$

Above, we have suppressed the boundary terms since we restrict our attention to closed geometries in the current study.

The first variation in Eq. (5.5) then furnishes the equilibrium equations in the tangent plane

$$\lambda_{,\alpha} = -\frac{\partial W}{\partial \theta^{\alpha}} \tag{5.7}$$

and along the surface normal

$$G = 0, \tag{5.8}$$

popularly known as the shape equation.

5.3 The second variation

The second variation of the position field can be expressed as

$$\ddot{\mathbf{r}} = \left.\frac{\partial^2 \mathbf{r}}{\partial \epsilon^2}\right|_{\epsilon=0} = \mathbf{v} = v^{\alpha}\mathbf{a}_{\alpha} + v\mathbf{n}, \tag{5.9}$$

where v^{α} and v are the tangential and normal components and are independent of the vector components of the first variation. The second variation of the energy E can be computed from Eq. (5.5) and is given by

$$\ddot{E} = \int_{\omega} \left\{ -\dot{u}^{\alpha}\left(\lambda_{,\alpha} + \frac{\partial W}{\partial \theta^{\alpha}}\right) - u^{\alpha}\frac{\partial \dot{W}}{\partial \theta^{\alpha}} + \dot{u}G + u\dot{G} \right\} da \tag{5.10}$$

subject to the incompressibility constraint,

$$\frac{\dot{J}}{J} = u^{\alpha}_{;\alpha} - 2uH = 0, \tag{5.11}$$

and the volumetric constraint

$$\dot{V} = \int_{\omega} u\, da = 0. \tag{5.12}$$

The variation of the tangential components of the first variation of the position field $\mathbf{u}$ is given by

$$\begin{aligned} \dot{u}^{\alpha} &= \dot{\mathbf{u}} \cdot \mathbf{a}^{\alpha} + \mathbf{u} \cdot \dot{\mathbf{a}}^{\alpha}, \\ &= (\mathbf{v} \cdot \mathbf{a}^{\alpha}) + (\mathbf{u} \cdot \mathbf{u}_{,\beta})a^{\alpha\beta} - (\mathbf{u} \cdot \mathbf{a}^{\gamma})a^{\alpha\lambda}\dot{a}_{\lambda\gamma} \end{aligned} \tag{5.13}$$

where

$$\begin{aligned}\dot{\mathbf{a}}^{\alpha} &= a^{\alpha\beta}\dot{\mathbf{a}}_{\beta} + \dot{a}^{\alpha\beta}\mathbf{a}_{\beta}, \quad \text{and} \\ \dot{a}^{\alpha\beta} &= -a^{\alpha\lambda}a^{\beta\gamma}\dot{a}_{\lambda\gamma}.\end{aligned} \tag{5.14}$$

Using the relation,

$$\mathbf{u}\cdot\mathbf{u}_{,\beta} = \frac{1}{2}(\mathbf{u}\cdot\mathbf{u})_{,\beta} = u^{\eta}u_{\eta;\beta} + uu_{,\beta} \tag{5.15}$$

in Eq. (5.13), we obtain

$$\begin{aligned}\dot{u}^{\alpha} &= v^{\alpha} + a^{\alpha\beta}\Big(u^{\eta}u_{\eta;\beta} + uu_{,\beta}\Big) - u^{\gamma}a^{\alpha\lambda}\Big(u_{\lambda;\gamma} + u_{\gamma;\lambda} - 2ub_{\lambda\gamma}\Big), \\ &= v^{\alpha} + uu_{,\beta}a^{\alpha\beta} - u^{\gamma}u^{\alpha}_{;\gamma} + 2uu^{\gamma}b^{\alpha}_{\gamma}.\end{aligned} \tag{5.16}$$

Next, we compute the variation of the normal component of the first variation of the position field,

$$\begin{aligned}\dot{u} &= \dot{\mathbf{u}}\cdot\mathbf{n} + \mathbf{u}\cdot\dot{\mathbf{n}}, \\ &= v - u^{\alpha}u_{,\alpha} - u^{\alpha}u^{\gamma}b_{\gamma\alpha}.\end{aligned} \tag{5.17}$$

Above, the variation of the surface normal has been be expressed as [127],

$$\dot{\mathbf{n}} = -(\mathbf{n}\cdot\mathbf{u}_{,\alpha})\mathbf{a}^{\alpha}. \tag{5.18}$$

To proceed further, we define $I_{\alpha}(H, K; \theta^{\gamma}) = \frac{\partial W}{\partial \theta^{\alpha}}$ and compute its variation

$$\begin{aligned}\dot{I}_{\alpha} &= (I_{\alpha})_{H}\dot{H} + (I_{\alpha})_{K}\dot{K} \\ &= \frac{\partial W_H}{\partial\theta^{\alpha}}\left(u^{\gamma}H_{,\gamma} + \frac{(\Delta u)}{2} + u(2H^2 - K)\right) + \frac{\partial W_K}{\partial\theta^{\alpha}}\left(u^{\gamma}K_{,\gamma} + 2uHK + \tilde{b}^{\gamma\beta}u_{;\gamma\beta}\right).\end{aligned} \tag{5.19}$$

Next, we compute the variation of G. We decompose its variation into tangential and normal parts denoted by $\dot{G}_t$ and $\dot{G}_n$, respectively.

5.3.1 Tangential variations

The tangential variation of the first term of G in Eq. (5.6) can be written as

$$\dot{\overline{\Delta W_H}} = \dot{\overline{(W_H)_{;\alpha\beta}}}a^{\alpha\beta} + (W_H)_{;\alpha\beta}\dot{a}^{\alpha\beta}, \tag{5.20}$$

where $\dot{\overline{()}}$ signifies the variation of the overall quantity within the parentheses. Expanding the first term in the above equation, we get

$$\dot{\overline{(W_H)_{;\alpha\beta}}} = \dot{\overline{(W_H)_{,\alpha\beta} - (W_H)_{,\lambda}\Gamma^{\lambda}_{\alpha\beta}}}. \tag{5.21}$$

Here, we note the fact that variational derivative (signified by the superposed dot) does not commute with the covariant derivative but it does commute with the derivative with respect to parameterizing variables θ^{α}. Thus, the above relation can be rewritten as,

$$\dot{\overline{(W_H)_{;\alpha\beta}}} = (\dot{W}_H)_{,\alpha\beta} - (\dot{W}_H)_{,\lambda}\Gamma^{\lambda}_{\alpha\beta} - (W_H)_{,\lambda}\dot{\Gamma}^{\lambda}_{\alpha\beta}. \tag{5.22}$$

Substituting Eq. (5.22) in Eq. (5.20) yields

$$\dot{\overline{\Delta W_H}} = (\dot{W}_H)_{;\alpha\beta}a^{\alpha\beta} - (W_H)_{,\lambda}\dot{\Gamma}^{\lambda}_{\alpha\beta}a^{\alpha\beta} + (W_H)_{;\alpha\beta}\dot{a}^{\alpha\beta}, \tag{5.23}$$

where the variation of the Christoffel symbols are given by ([113])

$$\dot{\Gamma}^{\lambda}_{\alpha\beta} = \frac{1}{2}a^{\lambda\eta}\left\{\dot{a}_{\eta\beta;\alpha} + \dot{a}_{\eta\alpha;\beta} - \dot{a}_{\alpha\beta;\eta}\right\}. \tag{5.24}$$

The tangential variations of $a_{\alpha\beta}$, $b_{\alpha\beta}$, H, K and J are given by (from chapter 2)

$$\begin{aligned} &\dot{a}_{\alpha\beta} = u_{\alpha;\beta} + u_{\beta;\alpha}; \quad \dot{b}_{\alpha\beta} = u^{\lambda}_{;\beta}b_{\lambda\alpha} + u^{\lambda}_{;\alpha}b_{\lambda\beta} + u^{\lambda}b_{\lambda\alpha;\beta}; \\ &\dot{H} = u^{\alpha}H_{,\alpha}; \quad \dot{K} = u^{\alpha}K_{,\alpha}; \quad \frac{\dot{J}}{J} = u^{\alpha}_{;\alpha}. \end{aligned} \tag{5.25}$$

Using Eqs. (5.14), (5.24) and (5.25), Eq. (5.23) can be expressed as

$$\begin{aligned} \dot{\overline{\Delta W_H}} = &(W_{HH}\dot{H} + W_{HK}\dot{K})_{;\alpha\beta}a^{\alpha\beta} - (W_H)_{,\lambda}a^{\lambda\eta}(u_{\eta;\alpha\beta} + u_{\alpha;\eta\beta} \\ &- u_{\alpha;\beta\eta})a^{\alpha\beta} - (W_H)_{;\alpha\beta}a^{\alpha\lambda}a^{\beta\gamma}(u_{\lambda;\gamma} + u_{\gamma;\lambda}). \end{aligned} \tag{5.26}$$

With the help of Eq. (5.25), Eq. (5.26) can be further rearranged and expressed as

$$\begin{aligned} \dot{\overline{\Delta W_H}} = &\left(u^{\gamma}(W_H)_{,\gamma} - u^{\gamma}\frac{\partial W_H}{\partial\theta^{\gamma}}\right)_{;\alpha\beta}a^{\alpha\beta} - (W_H)_{,\lambda}u^{\lambda}_{;\alpha\beta}a^{\alpha\beta} \\ &- (W_H)_{,\lambda}a^{\lambda\eta}(u^{\beta}_{;\eta\beta} - u^{\beta}_{;\beta\eta}) - 2u^{\alpha}_{;\gamma}a^{\beta\gamma}(W_H)_{;\alpha\beta}. \end{aligned} \tag{5.27}$$

To simplify the above relation, we use the definition of Riemann curvature tensor

$$R^{\alpha}_{\beta\gamma\eta} = Ka^{\alpha\lambda}\Big\{a_{\lambda\gamma}a_{\beta\eta} - a_{\lambda\eta}a_{\beta\gamma}\Big\} \tag{5.28}$$

and the relationship

$$R^{\alpha}_{\beta\eta\gamma}u^{\beta} = u^{\alpha}_{;\gamma\eta} - u^{\alpha}_{;\eta\gamma} \tag{5.29}$$

which holds for any arbitrary vector field lying in the tangent plane. With the help of Eq. (5.29) along with the linearity of the Laplace operator and the chain rule for covariant derivatives, Eq. (5.27) can be written as

$$\begin{aligned}
\overline{\Delta\dot{W}_H} &= \Big(u^{\gamma}_{;\alpha\beta}(W_H)_{,\gamma} + 2u^{\gamma}_{;\alpha}(W_H)_{;\gamma\beta} + u^{\gamma}(W_H)_{;\gamma\alpha\beta}\Big)a^{\alpha\beta} - \Delta\Big(u^{\gamma}\frac{\partial W_H}{\partial\theta^{\gamma}}\Big) \\
&- (W_H)_{,\lambda}u^{\lambda}_{;\alpha\beta}a^{\alpha\beta} - u^{\gamma}(W_H)_{,\lambda}a^{\lambda\eta}R^{\beta}_{\gamma\beta\eta} - 2u^{\alpha}_{;\gamma}a^{\beta\gamma}(W_H)_{;\alpha\beta} \\
&= u^{\gamma}((W_H)_{,\alpha}a^{\alpha\beta})_{;\gamma\beta} - \Delta\Big(u^{\gamma}\frac{\partial W_H}{\partial\theta^{\gamma}}\Big) - u^{\gamma}(W_H)_{,\lambda}a^{\lambda\eta}R^{\beta}_{\gamma\beta\eta}.
\end{aligned} \tag{5.30}$$

To derive Eq. $(5.30)_2$, we have used the fact that metric is covariant constant and torsion free. As a result, for any scalar field '(W_H)' defined on the surface, $(W_H)_{;\alpha\beta} = (W_H)_{;\beta\alpha}$. Using the definition of the covariant derivative of a vector field along with Eqs. (5.29) and (5.28), Eq. (5.30) can be further reduced to

$$\begin{aligned}
\overline{\Delta\dot{W}_H} &= u^{\gamma}\Big[((W_H)_{,\alpha}a^{\alpha\beta})_{;\gamma\beta} - ((W_H)_{,\alpha}a^{\alpha\beta})_{;\beta\gamma}\Big] + u^{\gamma}(\Delta W_H)_{,\gamma} - \Delta\Big(u^{\gamma}\frac{\partial W_H}{\partial\theta^{\gamma}}\Big) \\
&- u^{\gamma}(W_H)_{,\lambda}a^{\lambda\eta}R^{\beta}_{\gamma\beta\eta} \\
&= u^{\gamma}(W_H)_{,\alpha}a^{\alpha\eta}R^{\beta}_{\eta\beta\gamma} + u^{\gamma}(\Delta W_H)_{,\gamma} - R^{\beta}_{\gamma\beta\eta}u^{\gamma}(W_H)_{,\lambda}a^{\lambda\eta} - \Delta\Big(u^{\gamma}\frac{\partial W_H}{\partial\theta^{\gamma}}\Big) \\
&= u^{\gamma}(\Delta W_H)_{,\gamma} - \Delta\Big(u^{\gamma}\frac{\partial W_H}{\partial\theta^{\gamma}}\Big).
\end{aligned} \tag{5.31}$$

The rightmost term in the above equation arises from the inhomogeneity in the lipid membrane.

Next, we compute the tangential variation of $(W_K)_{;\alpha\beta}\tilde{b}^{\alpha\beta}$ in Eq.(5.6). We use the Cayley-Hamilton theorem in the form

$$\tilde{b}^{\alpha\beta} = 2Ha^{\alpha\beta} - b^{\alpha\beta} \tag{5.32}$$

to obtain

$$\dot{\overline{(W_K)_{;\alpha\beta}(2Ha^{\alpha\beta}-b^{\alpha\beta})}} = 2\dot{H}\Delta W_K + 2H\dot{\overline{\Delta W_K}} - \dot{\overline{(W_K)_{;\alpha\beta}b^{\alpha\beta}}}. \tag{5.33}$$

Analogous to the variation of the surface Laplacian of W_H, we can write

$$\dot{\overline{\Delta W_K}} = u^\gamma(\Delta W_K)_{,\gamma} - \Delta\left(u^\gamma \frac{\partial W_K}{\partial \theta^\gamma}\right). \tag{5.34}$$

Substituting Eqs. (5.25) and (5.32) in Eq. (5.33) yields

$$\dot{\overline{(W_K)_{;\alpha\beta}(2Ha^{\alpha\beta}-b^{\alpha\beta})}} = 2u^\gamma\left(H\Delta W_K\right)_{,\gamma} - \dot{\overline{(W_K)_{;\alpha\beta}b^{\alpha\beta}}} - 2H\Delta\left(u^\gamma \frac{\partial W_K}{\partial \theta^\gamma}\right). \tag{5.35}$$

The second term on the RHS of Eq. (5.35) can be expressed as

$$\dot{\overline{(W_K)_{;\alpha\beta}b^{\alpha\beta}}} = \left((\dot{W}_K)_{;\alpha\beta} - (W_K)_{,\lambda}\dot{\Gamma}^\lambda_{\alpha\beta}\right)b^{\alpha\beta} + (W_K)_{;\alpha\beta}\dot{b}^{\alpha\beta}. \tag{5.36}$$

Next, we substitue Eqs. (5.3), (5.14), (5.24) and (5.29) in Eq. (5.36) to obtain,

$$\begin{aligned}
&\dot{\overline{(W_K)_{;\alpha\beta}b^{\alpha\beta}}} = \left(u^\gamma(W_{KK}\dot{K} + W_{KH}\dot{H})\right)_{;\alpha\beta} b^{\alpha\beta} - \frac{1}{2}(W_K)_{,\lambda}a^{\lambda\eta}\Big\{\dot{a}_{\eta\beta;\alpha} + \dot{a}_{\eta\alpha;\beta} \\
&- \dot{a}_{\alpha\beta;\eta}\Big\} + (W_K)_{;\alpha\beta}\dot{b}_{\lambda\gamma}a^{\alpha\lambda}a^{\beta\gamma} + 2(W_K)_{;\alpha\beta}b_{\lambda\gamma}a^{\beta\gamma}\dot{a}^{\alpha\lambda} \\
&= \left(u^\gamma(W_K)_{,\gamma}\right)_{;\alpha\beta} b^{\alpha\beta} - \left(u^\gamma\frac{\partial(W_K)}{\partial\theta^\gamma}\right)_{;\alpha\beta} b^{\alpha\beta} - (W_K)_{,\lambda}b^{\alpha\beta}a^{\lambda\eta}(u_{\eta;\beta\alpha} + u_{\beta;\eta\alpha} \\
&- u_{\alpha;\beta\eta}) + (W_K)_{;\alpha\beta}a^{\alpha\lambda}a^{\beta\gamma}\Big\{u^\eta_{;\gamma}b_{\eta\lambda} + u^\eta_{;\lambda}b_{\eta\gamma} + u^\eta b_{\eta\gamma;\lambda}\Big\} \\
&- 2(W_K)_{;\alpha\beta}b^\beta_\lambda a^{\alpha\eta}a^{\lambda\theta}(u_{\theta;\eta} + u_{\eta;\theta}) \\
&= \left(u^\gamma_{;\alpha\beta}(W_K)_{,\gamma} + 2u^\gamma_{;\alpha}(W_K)_{;\gamma\beta} + u^\gamma(W_K)_{;\gamma\alpha\beta}\right)b^{\alpha\beta} - u^\lambda_{;\alpha\beta}(W_K)_{,\lambda}b^{\alpha\beta} \\
&- (W_K)_{,\lambda}b^\alpha_\beta a^{\lambda\eta}(u^\beta_{;\eta\alpha} - u^\beta_{;\alpha\eta}) + u^\eta(W_K)_{;\alpha\beta}(b^{\alpha\beta})_{;\eta} - 2u^\alpha_{;\theta}(W_K)_{;\alpha\beta}b^{\beta\theta} \\
&= u^\gamma(W_K)_{;\beta\gamma\alpha}b^{\alpha\beta} - (W_K)_{,\lambda}b^\alpha_\beta a^{\lambda\eta}R^\beta_{\gamma\alpha\eta}u^\gamma + u^\eta(W_K)_{;\alpha\beta}(b^{\alpha\beta})_{;\eta} \\
&- b^{\alpha\beta}\left(u^\gamma\frac{\partial W_K}{\partial\theta^\gamma}\right)_{;\alpha\beta}.
\end{aligned} \tag{5.37}$$

We use the fact that the metric is torsion free and add-and-subtract $u^\gamma (W_K)_{;\alpha\beta\gamma} b^{\alpha\beta}$ in the above equation to obtain,

$$\begin{aligned}\dot{\overline{(W_K)_{;\alpha\beta} b^{\alpha\beta}}} &= u^\gamma \Big\{ ((W_K)_{,\beta} a^{\beta\eta})_{;\gamma\alpha} - ((W_K)_{,\beta} a^{\beta\eta})_{;\alpha\gamma} \Big\} b^\alpha_\eta \\ &- (W_K)_{,\lambda} b^\alpha_\beta a^{\lambda\eta} R^\beta_{\gamma\alpha\eta} u^\gamma + u^\gamma (W_K)_{;\alpha\beta\gamma} b^{\alpha\beta} \\ &+ u^\gamma (W_K)_{;\alpha\beta} (b^{\alpha\beta})_{;\gamma} - b^{\alpha\beta} \left(u^\gamma \frac{\partial W_K}{\partial \theta^\gamma} \right)_{;\alpha\beta}.\end{aligned} \tag{5.38}$$

With the help of Eqs. (5.19) and (5.29), Eq. (5.38) can be further reduced to

$$\dot{\overline{(W_K)_{;\alpha\beta} b^{\alpha\beta}}} = u^\gamma \left((W_K)_{;\alpha\beta} b^{\alpha\beta} \right)_{;\gamma} - b^{\alpha\beta} \left(u^\gamma \frac{\partial W_K}{\partial \theta^\gamma} \right)_{;\alpha\beta}. \tag{5.39}$$

We then substitute Eq. (5.39) into Eq. (5.35) to obtain

$$\begin{aligned}&\dot{\overline{(W_K)_{;\alpha\beta} (2Ha^{\alpha\beta} - b^{\alpha\beta})}} = u^\gamma \left(2H\Delta W_K \right)_{,\gamma} - u^\gamma \left((W_K)_{;\alpha\beta} b^{\alpha\beta} \right)_{,\gamma} \\ &+ b^{\alpha\beta} \left(u^\gamma \frac{\partial W_K}{\partial \theta^\gamma} \right)_{;\alpha\beta} - 2H\Delta \left(u^\gamma \frac{\partial W_K}{\partial \theta^\gamma} \right) \\ &= u^\gamma \left((W_K)_{;\alpha\beta} \tilde{b}^{\alpha\beta} \right)_{;\gamma} - \tilde{b}^{\alpha\beta} \left(u^\gamma \frac{\partial W_K}{\partial \theta^\gamma} \right)_{;\alpha\beta}.\end{aligned} \tag{5.40}$$

Similar to the tangential variation of $\Delta(W_H)$, the second term in Eq. (5.40) arises because of inhomogeneity in the membrane properties.

Next, we compute the tangential variations of the remaining terms of 'G' in Eq. (5.6). These include

$$\begin{aligned}&\dot{\overline{W_H (2H^2 - K)}} = (W_{HH}\dot{H} + W_{HK}\dot{K})(2H^2 - K) + W_H (4H\dot{H} - \dot{K}) \\ &= u^\gamma \left(W_H (2H^2 - K) \right)_{,\gamma} - u^\gamma \left(\frac{\partial W_H}{\partial \theta^\gamma} \right) (2H^2 - K) \text{ and}\end{aligned} \tag{5.41}$$

$$\begin{aligned}&\dot{\overline{2H(KW_K - W)}} = 2\dot{H}(KW_K - W) + 2H(\dot{K}W_K + KW_{KH}\dot{H} + KW_{KK}\dot{K} \\ &- W_H\dot{H} - W_K\dot{K}) \\ &= u^\gamma \left(2H(KW_K - W) \right)_{,\gamma} - u^\gamma 2H \left(K\frac{\partial W_K}{\partial \theta^\gamma} - \frac{\partial W}{\partial \theta^\gamma} \right).\end{aligned} \tag{5.42}$$

and

$$\overline{2\dot{\lambda}H} = 2\lambda\dot{H} = u^{\gamma}(2\lambda H)_{,\gamma} - 2u^{\gamma}\lambda_{,\gamma}H. \tag{5.43}$$

We now substitute Eqs. (5.31), (5.40), (5.41), (5.42) and (5.43) in Eq. (5.6), to compute the tangential variation of G ($\dot{G}_t$)

$$\begin{aligned}\dot{G}_t = u^{\gamma}\Bigg\{&\frac{1}{2}\Delta W_H + (W_K)_{;\alpha\beta}\tilde{b}^{\alpha\beta} + W_H(2H^2 - K) + 2H(KW_K - W) - 2\lambda H \\ &- p\Bigg\}_{,\gamma} - \Bigg\{\frac{1}{2}\Delta\left(u^{\gamma}\frac{\partial W_H}{\partial\theta^{\gamma}}\right) + \tilde{b}^{\alpha\beta}\left(u^{\gamma}\frac{\partial W_K}{\partial\theta^{\gamma}}\right)_{;\alpha\beta} + u^{\gamma}(2H^2 - K)\frac{\partial W_H}{\partial\theta^{\gamma}} \\ &+ 2u^{\gamma}H\left(K\frac{\partial W_K}{\partial\theta^{\gamma}} - \frac{\partial W}{\partial\theta^{\gamma}} - \lambda_{,\gamma}\right)\Bigg\}.\end{aligned} \tag{5.44}$$

Above, we have used the fact that pressure field is uniform on the surface. Using Eq. (5.6), Eq. (5.44) can be expressed as,

$$\begin{aligned}\dot{G}_t = u^{\gamma}G_{,\gamma} - \Bigg\{&\frac{1}{2}\Delta\left(u^{\gamma}\frac{\partial W_H}{\partial\theta^{\gamma}}\right) + \tilde{b}^{\alpha\beta}\left(u^{\gamma}\frac{\partial W_K}{\partial\theta^{\gamma}}\right)_{;\alpha\beta} + u^{\gamma}(2H^2 - K)\frac{\partial W_H}{\partial\theta^{\gamma}} \\ &+ 2u^{\gamma}H\left(K\frac{\partial W_K}{\partial\theta^{\gamma}} - \frac{\partial W}{\partial\theta^{\gamma}} - \lambda_{,\gamma}\right)\Bigg\}.\end{aligned} \tag{5.45}$$

Other than the terms arising from inhomogeneity, Eq. (5.45) is similar to the tangential variations of an arbitrary scalar surface field '$f(\mathbf{r}(\theta^{\alpha}))$' derived by Capovilla et. al [113].

5.3.2 Normal Variations

For normal variations $\mathbf{u} = u\mathbf{n}$, Eqs. (5.3) and (5.4) yield [27]

$$\begin{aligned}&\dot{a}_{\alpha\beta} = -2ub_{\alpha\beta}; \quad \dot{b}_{\alpha\beta} = u_{;\alpha\beta} - ub^{\gamma}_{\alpha}b_{\gamma\beta}; \\ &\dot{H} = \frac{1}{2}(\Delta u) + u(2H^2 - K); \quad \dot{K} = u_{;\alpha\beta}\tilde{b}^{\alpha\beta} + 2uHK.\end{aligned} \tag{5.46}$$

First, we use Eq. (5.23) to compute the normal variation of $\Delta(W_H)$. With the help of Eq. (5.46), we compute the first term on the RHS of Eq. (5.23) and is given by

$$\begin{aligned}(\dot{W}_H)_{;\alpha\beta}a^{\alpha\beta} &= \left\{W_{HH}\dot{H} + W_{HK}\dot{K}\right\}_{;\alpha\beta}a^{\alpha\beta} \\ &= \left\{W_{HH}\left(\frac{1}{2}\Delta u + u(2H^2 - K)\right) + W_{HK}\left(u_{;\alpha\beta}\tilde{b}^{\alpha\beta} + 2uHK\right)\right\}_{;\alpha\beta}a^{\alpha\beta}.\end{aligned} \tag{5.47}$$

We use Eq. (5.24) along with Cayley-Hamilton theorem and the fact that metric tensor is covariant constant to compute the second term in Eq. (5.23)

$$\begin{aligned} &- (W_H)_{,\lambda}\dot{\Gamma}^{\lambda}_{\alpha\beta}a^{\alpha\beta} = (W_H)_{,\lambda}a^{\alpha\beta}a^{\lambda\eta}((2ub_{\eta\alpha})_{;\beta} - (ub_{\alpha\beta})_{;\eta}) \\ &= (W_H)_{,\lambda}\bigg((2uHa^{\beta\lambda})_{;\beta} - (2u\tilde{b}^{\beta\lambda})_{;\beta}\bigg). \end{aligned} \tag{5.48}$$

We again use Eq. (5.46) to compute the third term in Eq. (5.23)

$$(W_H)_{;\alpha\beta}\dot{a}^{\alpha\beta} = 2u(W_H)_{;\alpha\beta}b^{\alpha\beta}. \tag{5.49}$$

Finally, we substitute Eqs. (5.47), (5.48) and (5.49) in Eq. (5.23) to obtain

$$\begin{aligned} \dot{\overline{\Delta W_H}} &= \bigg\{W_{HH}\bigg(\frac{1}{2}\Delta u + u(2H^2 - K)\bigg) + W_{HK}\bigg(u_{;\alpha\beta}\tilde{b}^{\alpha\beta} + 2uHK\bigg)\bigg\}_{;\alpha\beta}a^{\alpha\beta} \\ &+ (W_H)_{,\lambda}\bigg((2uHa^{\beta\lambda})_{;\beta} - (2u\tilde{b}^{\beta\lambda})_{;\beta}\bigg) + 2u(W_H)_{;\alpha\beta}b^{\alpha\beta}. \end{aligned} \tag{5.50}$$

Next, we use Eq. (5.46) to compute the normal variation of $(W_K)_{;\alpha\beta}\tilde{b}^{\alpha\beta}$ given by

$$\dot{\overline{(W_K)_{;\alpha\beta}(2Ha^{\alpha\beta} - b^{\alpha\beta})}} = (\dot{W}_K)_{;\alpha\beta}\tilde{b}^{\alpha\beta} - (W_K)_{,\lambda}\dot{\Gamma}^{\lambda}_{\alpha\beta}\tilde{b}^{\alpha\beta} + (W_K)_{;\alpha\beta}\dot{\tilde{b}}^{\alpha\beta}, \tag{5.51}$$

where

$$\begin{aligned} (\dot{W}_K)_{;\alpha\beta}\tilde{b}^{\alpha\beta} &= \bigg\{W_{KH}\bigg(\frac{1}{2}\Delta u + u(2H^2 - K)\bigg) \\ &+ W_{KK}\bigg(u_{;\alpha\beta}\tilde{b}^{\alpha\beta} + 2uHK\bigg)\bigg\}_{;\alpha\beta}\tilde{b}^{\alpha\beta}, \end{aligned} \tag{5.52}$$

$$(W_K)_{,\lambda}\dot{\Gamma}^{\lambda}_{\alpha\beta}\tilde{b}^{\alpha\beta} = -(W_K)_{,\lambda}\tilde{b}^{\alpha\beta}a^{\lambda\eta}\bigg[(2ub_{\eta\alpha})_{;\beta} - (ub_{\alpha\beta})_{;\eta}\bigg] \quad = 0, \tag{5.53}$$

and

$$\begin{aligned} \dot{\tilde{b}}^{\alpha\beta} &= -\varepsilon^{\alpha\lambda}\varepsilon^{\beta\gamma}\frac{\dot{a}}{a}b_{\lambda\gamma} + \varepsilon^{\alpha\lambda}\varepsilon^{\beta\gamma}\dot{b}_{\lambda\gamma} \\ &= 4uH\tilde{b}^{\alpha\beta} + \varepsilon^{\alpha\lambda}\varepsilon^{\beta\gamma}(u_{;\lambda\gamma} - ub^{\eta}_{\lambda}b_{\eta\gamma}). \end{aligned} \tag{5.54}$$

Substituting Eqs. (5.52), (5.53) and (5.54) in Eq. (5.51) furnishes

$$\begin{aligned} \dot{\overline{(W_K)_{;\alpha\beta}(2Ha^{\alpha\beta} - b^{\alpha\beta})}} &= \bigg\{W_{KH}\bigg(\frac{1}{2}\Delta u + u(2H^2 - K)\bigg) \\ &+ W_{KK}\bigg(u_{;\alpha\beta}\tilde{b}^{\alpha\beta} + 2uHK\bigg)\bigg\}_{;\alpha\beta}\tilde{b}^{\alpha\beta} + 4uH(W_K)_{;\alpha\beta}\tilde{b}^{\alpha\beta} \\ &+ \varepsilon^{\alpha\lambda}\varepsilon^{\beta\gamma}(u_{;\lambda\gamma} - ub^{\eta}_{\lambda}b_{\eta\gamma})(W_K)_{;\alpha\beta}. \end{aligned} \tag{5.55}$$

Next, we use Eq. (5.46) to compute the normal variations of the remaining terms of G in Eq. (5.6) which are given by

$$\begin{aligned}
&\overline{\dot{W_H}(2H^2-K)+2H(KW_K-W)} = \Big\{W_{HH}(2H^2-K)+2HW_H+2KW_K \\
&+2HKW_{HK}-2W\Big\}\dot{H}+\Big\{W_{HK}(2H^2-K)-W_H+2HKW_{KK}\Big\}\dot{K}, \\
&=(\Delta u)\Big\{\frac{1}{2}W_{HH}(2H^2-K)+HW_H+HKW_{HK}+(KW_K-W)\Big\} \\
&+u_{;\alpha\beta}\tilde{b}^{\alpha\beta}\Big\{2HKW_{KK}+(2H^2-K)W_{HK}-W_H\Big\}+u\Big\{W_{HH}(2H^2-K)^2 \\
&+W_{KK}(2HK)^2+4HK(2H^2-K)W_{HK}+4HW_H(H^2-K) \\
&+2(2H^2-K)(KW_K-W)\Big\},
\end{aligned} \tag{5.56}$$

and

$$2\lambda\dot{H}=\lambda(\Delta u+2u(2H^2-K)). \tag{5.57}$$

Combining Eqs. (5.50), (5.55), (5.56) and (5.57) yields the total normal variation of G, which after some rearrangement can be written as

$$\begin{aligned}
&\dot{G}_n=\frac{1}{2}\Big\{\Delta\Big[W_{HH}\Big(\frac{1}{2}\Delta u+u(2H^2-K)\Big)\Big]+\Delta\Big[W_{HK}\Big(u_{;\alpha\beta}\tilde{b}^{\alpha\beta}+2uHK\Big)\Big] \\
&+(W_H)_{,\lambda}\Big((2uH)_{;\beta}a^{\beta\lambda}-2u_{,\beta}\tilde{b}^{\beta\lambda}\Big)\Big\}+\Big\{W_{KH}\Big[\frac{1}{2}\Delta u+u(2H^2-K)\Big] \\
&+W_{KK}\Big[u_{;\lambda\gamma}\tilde{b}^{\lambda\gamma}+2uHK\Big]\Big\}_{;\alpha\beta}\tilde{b}^{\alpha\beta}+\varepsilon^{\alpha\lambda}\varepsilon^{\beta\gamma}(W_K)_{;\alpha\beta}(u_{;\lambda\gamma}-ub^{\eta}_{\lambda}b_{\eta\gamma}) \\
&-u(W_H)_{;\alpha\beta}\tilde{b}^{\alpha\beta}+(\Delta u)\Big\{\frac{1}{2}W_{HH}(2H^2-K)+HW_H+HKW_{HK} \\
&+(KW_K-W)\Big\}+u_{;\alpha\beta}\tilde{b}^{\alpha\beta}\Big\{2HKW_{KK}+(2H^2-K)W_{HK}-W_H\Big\} \\
&+u\Big\{W_{HH}(2H^2-K)^2+W_{KK}(2HK)^2+4HK(2H^2-K)W_{HK}-4H^3W_H \\
&-2(2H^2+K)(KW_K-W)\Big\}-2\lambda\Big\{\frac{1}{2}\Delta u-u(2H^2+K)\Big\}+4uH(G+p).
\end{aligned} \tag{5.58}$$

5.3.3 Total Variations

We now combine Eqs. (5.16), (5.17), (5.19), (5.45), (5.58) to compute the second variation of E

$$
\begin{aligned}
\ddot{E} = \int_\omega \Bigg\{ & -(v^\alpha + uu_{,\beta}a^{\alpha\beta} - u^\gamma u^\alpha_{;\gamma} + 2uu^\gamma b^\alpha_\gamma)\left(\lambda_{,\alpha} + \frac{\partial W}{\partial \theta^\alpha}\right) \\
& - u^\alpha \left\{ \frac{\partial W_H}{\partial \theta^\alpha}\left(u^\gamma H_{,\gamma} + \frac{1}{2}\Delta u + u(2H^2 - K)\right) + \frac{\partial W_K}{\partial \theta^\alpha}\left(u^\gamma K_{,\gamma} + 2uHK \right.\right. \\
& \left.\left. + u_{;\gamma\beta}\tilde{b}^{\gamma\beta}\right)\right\} + (v - u^\gamma u_{,\alpha} - u^\alpha u^\gamma b_{\gamma\alpha})G + uu^\gamma G_{,\gamma} - u\left\{\frac{1}{2}\Delta\left(u^\gamma \frac{\partial W_H}{\partial \theta^\gamma}\right)\right. \\
& \left. + \tilde{b}^{\alpha\beta}\left(u^\gamma \frac{\partial W_K}{\partial \theta^\gamma}\right)_{;\alpha\beta} + u^\gamma(2H^2 - K)\frac{\partial W_H}{\partial \theta^\gamma} + 2u^\gamma H\left(K\frac{\partial W_K}{\partial \theta^\gamma} - \frac{\partial W}{\partial \theta^\gamma} - \lambda_{,\gamma}\right)\right\} \\
& + u\left[\frac{1}{2}\left\{\Delta\left[W_{HH}\left(\frac{1}{2}\Delta u + u(2H^2 - K)\right)\right] + \Delta\left[W_{HK}\left(u_{;\alpha\beta}\tilde{b}^{\alpha\beta} + 2uHK\right)\right]\right. \right. \\
& \left. + (W_H)_{,\lambda}\left((2uH)_{;\beta}a^{\beta\lambda} - 2u_{,\beta}\tilde{b}^{\beta\lambda}\right)\right\} + \left\{W_{KH}\left[\frac{1}{2}\Delta u + u(2H^2 - K)\right]\right. \\
& \left.\left. + W_{KK}\left[u_{;\alpha\beta}\tilde{b}^{\alpha\beta} + 2uHK\right]\right\}_{;\alpha\beta}\tilde{b}^{\alpha\beta} + \varepsilon^{\alpha\lambda}\varepsilon^{\beta\gamma}(W_K)_{;\alpha\beta}(u_{;\lambda\gamma} - ub^\eta_\lambda b_{\eta\gamma}) \right. \\
& - u(W_H)_{;\alpha\beta}\tilde{b}^{\alpha\beta} + (\Delta u)\left\{\frac{1}{2}W_{HH}(2H^2 - K) + HW_H + HKW_{HK}\right. \\
& \left. + (KW_K - W)\right\} + u_{;\alpha\beta}\tilde{b}^{\alpha\beta}\left\{2HKW_{KK} + (2H^2 - K)W_{HK} - W_H\right\} \\
& + u\left\{W_{HH}(2H^2 - K)^2 + W_{KK}(2HK)^2 + 4HK(2H^2 - K)W_{HK} - 4H^3 W_H \right. \\
& \left. - 2(2H^2 + K)(KW_K - W)\right\} - 2\lambda\left\{\frac{1}{2}\Delta u - u(2H^2 + K)\right\} \\
& \left. + 4uH(G + p)\right]\Bigg\} da.
\end{aligned}
\tag{5.59}
$$

Since at equilibrium, Eqs. (5.7) and (5.8) are satisfied and $G_{,\gamma} = 0$, (as G = 0 is identically satisfied on all the material points on the surface), $\ddot{E}$ reduces to

$$\begin{aligned}
\ddot{E} = \int_\omega \Bigg\{ & -u^\alpha \Bigg\{ \frac{\partial W_H}{\partial \theta^\alpha} \left(u^\gamma H_{,\gamma} + \frac{1}{2}\Delta u + 2u(2H^2 - K) \right) + \frac{\partial W_K}{\partial \theta^\alpha} \Big(u^\gamma K_{,\gamma} \\
& + 4uHK + u_{;\gamma\beta}\tilde{b}^{\gamma\beta} \Big) \Bigg\} - u \Bigg\{ \frac{1}{2}\Delta \left(u^\gamma \frac{\partial W_H}{\partial \theta^\gamma} \right) + \tilde{b}^{\alpha\beta} \left(u^\gamma \frac{\partial W_K}{\partial \theta^\gamma} \right)_{;\alpha\beta} \Bigg\} \\
& + u \Bigg[\frac{1}{2} \Bigg\{ \Delta \left[W_{HH} \left(\frac{1}{2}\Delta u + u(2H^2 - K) \right) \right] + \Delta \left[W_{HK} \left(u_{;\alpha\beta}\tilde{b}^{\alpha\beta} + 2uHK \right) \right] \\
& + (W_H)_{,\lambda} \left((2uH)_{;\beta} a^{\beta\lambda} - 2u_{,\beta}\tilde{b}^{\beta\lambda} \right) \Bigg\} + \Bigg\{ W_{KH} \left[\frac{1}{2}\Delta u + u(2H^2 - K) \right] \\
& + W_{KK} \left[u_{;\alpha\beta}\tilde{b}^{\alpha\beta} + 2uHK \right] \Bigg\}_{;\alpha\beta} \tilde{b}^{\alpha\beta} + \varepsilon^{\alpha\lambda}\varepsilon^{\beta\gamma}(W_K)_{;\alpha\beta}(u_{;\lambda\gamma} - u b^\eta_\lambda b_{\eta\gamma}) \\
& - u(W_H)_{;\alpha\beta}\tilde{b}^{\alpha\beta} + (\Delta u) \Bigg\{ \frac{1}{2} W_{HH}(2H^2 - K) + HW_H + HKW_{HK} \\
& + (KW_K - W) \Bigg\} + u_{;\alpha\beta}\tilde{b}^{\alpha\beta} \Bigg\{ 2HKW_{KK} + (2H^2 - K)W_{HK} - W_H \Bigg\} \\
& + u \Bigg\{ W_{HH}(2H^2 - K)^2 + W_{KK}(2HK)^2 + 4HK(2H^2 - K)W_{HK} - 4H^3 W_H \\
& - 2(2H^2 + K)(KW_K - W) \Bigg\} - 2\lambda \Bigg\{ \frac{1}{2}\Delta u - u(2H^2 + K) \Bigg\} + 4uHp \Bigg] \Bigg\} \, da.
\end{aligned} \tag{5.60}$$

This is the generalized second variation of E at an equilibrium configuration. For a system to be stable, $\ddot{E} > 0$ subject to the incompressibility constraint

$$u^\alpha_{;\alpha} = 2uH, \tag{5.61}$$

and the volumetric constraint,

$$\int_\omega u \, da = 0. \tag{5.62}$$

We note here that although we have not restricted on the form of strain energy density, W, it has to satisfy the Legendre-Hadamard condition for stability, as derived in [123].

5.4 Comparison with other models

We specialize Eq. (5.60) for the Helfrich-Canham energy given by

$$W = k(H - C_0(\theta^\alpha))^2 + \bar{k}K. \tag{5.63}$$

Above, k is the local bending modulus of the membrane and $\bar{k}$ is the Gaussian moduli. $C_0(\theta^\alpha)$ is the spatially varying spontaneous curvature field which could potentially arise because of a heterogeneous composition of a bilayer or spatially varying interactions with membrane remodeling proteins. Substituting Eq. (5.63) in Eq. (5.60) and invoking the Gauss-Bonnet theorem yields

$$\begin{aligned}
\ddot{E} = \int_\omega \Bigg\{ & u^\alpha \left\{ 2k \frac{\partial C_0}{\partial \theta^\alpha} \left(u^\gamma H_{,\gamma} + \frac{1}{2}\Delta u + 2u(2H^2 - K) \right) \right\} + u \left\{ k\Delta \left(u^\gamma \frac{\partial C_0}{\partial \theta^\gamma} \right) \right\} \\
& - 2u_{;\alpha\beta} k \tilde{b}^{\alpha\beta}(H - C_0) + u \Bigg[\left\{ \Delta \left[k \left(\frac{1}{2}\Delta u + u(2H^2 - K) \right) \right] \right. \\
& + 2k(H - C_0)_{,\lambda} \left((2uH)_{;\beta} a^{\beta\lambda} - 2u_{,\beta} \tilde{b}^{\beta\lambda} \right) \Bigg\} + (\Delta u) \Big\{ k(2H^2 - K) \\
& + 2kH(H - C_0) - k(H - C_0)^2 - \lambda \Big\} + u \Big\{ k(2H^2 - K)^2 - 4kH^3(H - C_0) \\
& \left. + 2k(2H^2 + K)(H - C_0)^2 - 2k(H - C_0)_{;\alpha\beta} \tilde{b}^{\alpha\beta} + 2\lambda(2H^2 + K) + 4Hp \Big\} \Bigg] \Bigg\} \, da.
\end{aligned} \tag{5.64}$$

For a homogeneous membrane with a uniform preferred curvature C_0, Eq. (5.64) further reduces to

$$\begin{aligned}
\ddot{E} = \int_\omega \Bigg\{ & u \Bigg[\left\{ k\Delta \left[\left(\frac{1}{2}\Delta u + u(2H^2 - K) \right) \right] + kH_{,\lambda} \left((2uH)_{;\beta} a^{\beta\lambda} - 2u_{,\beta} \tilde{b}^{\beta\lambda} \right) \right\} \\
& + (\Delta u) \left\{ k(3H^2 - K) - \lambda - k(C_0)^2 \right\} - 2u_{;\alpha\beta} k \tilde{b}^{\alpha\beta}(H - C_0) + u \left\{ kK(K - 2H^2) \right. \\
& \left. + 2(2H^2 + K)(\lambda + kC_0^2) + 4Hp - 4kHKC_0 - kH_{;\alpha\beta} \tilde{b}^{\alpha\beta} \right\} \Bigg] \Bigg\} \, da.
\end{aligned} \tag{5.65}$$

For $C_0 = 0$ and $W = k(2H)^2$, the above equation reduces to the one derived by Guven and co-workers in [113]. As is expected, at equilibrium, the tangential vari-

ations do not play a role in the stability criterion for a homogeneous membrane. It is, however, important to note that for the cases with incompressibility constraint, the tangential perturbations are related to the normal perturbations through Eq. (5.61) (unless the surface at equilibrium is a minimal surface with H=0). As a consequence, Eq. (5.61) can be used to write the entire second variation in terms of the tangential variation and its derivates.

Chapter 6 Summary and Future Work

6.1 Summary

In this study, we derive the theory of lipid membranes to model the effect of orthotropic curvature-inducing proteins. The extended theory was used to investigate the individual roles of actin and BAR proteins in executing CME in high membrane tension environment. We presented a new snap-through instability driven remodeling mechanism that governs vesicle shape evolution. We showed how actin-BAR synergy imparts robustness to the endocytic machinery. Since actin dynamics plays an integral role in other endocytic pathways such as phagocytosis, macropinocytosis and caveolae-mediated endocytosis, it is probable that such an instability could be at play in these processes. Our study reveals that a presence of membrane tension and actin forces are reasons enough to induce an instability-driven shape transformation. In addition, since other cellular processes such as cellular division and locomotion are associated with large scale remodeling of cellular interfaces, it would not be surprising if protein-induced instabilities, regulated by interface tension, contribute to these processes as well. To this end, we have extended the theory of stability of lipid membranes to account for it's interactions with isotropic curvature inducing proteins.

6.2 Future Work

Going forward, there are two main directions that can be pursued to gain further mechanistic insights into CME. First, the derived stability conditions can be used to investigate the stability of membrane invaginations. The analysis can furnish the reason for the loss of stability at a critical geometry. Also, the analysis

can be used to predict the nature of the forces and the curvatures needed from the proteins to trigger the instability. In addition to CME, such an analysis can provide insights into the mechanics of other non-clathrin dependent endocytic pathways. Second, in the current study, the distribution of the key proteins (clathrin, actin and BAR) on the membrane is imposed a priori. A parametric analysis is then conducted to predict their effect on membrane remodeling. However, in order to get more fundamental insights into CME and in particular, tension-dependent adaptation in CME, it is important to model the self-assembly of these proteins on to the membrane. Such an analysis would reveal the relative extent to which the membrane stresses and the geometry regulate the self-assembly of the membrane remodeling proteins, which is a subject of much speculation in the literature. Motivated by our findings, we have extended the theory of stability of isotropic membranes to account for the inhomogeneous interactions with proteins.

References

[1] Margulis, L., Schwartz, K.V. (1988). *Five Kingdoms.* WH freeman.

[2] Stockenius, W. (1962). Structure of the Plasma Membrane An Electron-Microscope Study. *Circulation*, 26(5), 1066-1069.

[3] Vinson, P.K., Talmon, Y.E., Walter, A.N. (1989). Vesicle-micelle transition of phosphatidylcholine and octyl glucoside elucidated by cryo-transmission electron microscopy. *Biophysical journal*, 56(4), 669.

[4] Hille, B. (2001). *Ion channels of excitable membranes* (Vol. 507). Sunderland, MA: Sinauer.

[5] Phillips, R., Kondev, J., Theriot, J., Garcia, H. (2013). *Physical Biology of the cell.* Garland Science.

[6] Peterson, B.R. (2005). Synthetic mimics of mammalian cell surface receptors prosthetic molecules that augment living cells. *Organic & biomolecular chemistry*, 3(20), 3607-3612.

[7] Kukulski, W., Schorb, M., Kaksonen, M., Briggs, J.A.G. (2012). Plasma membrane reshaping during endocytosis is revealed by time-resolved electron tomography. *Cell* 150(3), 508-520.

[8] Kaksonen, M., Toret, C.P., Drubin, D.G. (2006). Harnessing actin dynamics for clathrin-mediated endocytosis. *Nature reviews Molecular cell biology*, 7(6), 404-414.

[9] Weinberg, J., Drubin, D.G. (2012). Clathrin-mediated endocytosis in budding yeast. *Trends in cell biology* 22(1), 1-13.

[10] Aghamohammadzadeh, S., Ayscough, K.R. (2009). Differential requirements for actin during yeast and mammalian endocytosis. *Nature cell biology*, 11(8), 1039-1042.

[11] Boulant, S., Kural, C., Zeeh, J.C., Ubelmann, F., Kirchhausen, T. (2011). Actin dynamics counteract membrane tension during clathrin-mediated endocytosis *Nature cell biology* 13(9), 1124-1131.

[12] Conner, S.D., Schmid, S.L. (2003). Regulated portals of entry into the cell *Nature* 422 (6927) : 37-44.

[13] Boettner, D.R., Chi, R.J., Lemmon, S.K. (2012). Lessons from yeast for clathrin-mediated endocytosis. *Nature cell biology* 14(1), 2-10.

[14] Kaksonen, M., Sun, Y., Drubin, D.G. (2003). A Pathway for Association of Receptors, Adaptors, and Actin during Endocytic Internalization *Cell* 115(4), 475-487.

[15] Ferguson, S.M., De Camilli, P. (2012). Dynamin, a membrane-remodelling GTPase. *Nature reviews Molecular cell biology*, 13(2), 75-88.

[16] Kishimoto, T., Sun, Y., Buser, C., Liu, J., Michelot, A., Drubin, D.G. (2011). Determinants of endocytic membrane geometry, stability, and scission. *Proceedings of the National Academy of Sciences* 108(44), E979-E988.

[17] Cosserat, E., Cosserat, F. (1909). Theorie des corps deformables. *Paris*.

[18] Jenkins, J.T. (1977). The equations of mechanical equilibrium of a model membrane. *SIAM Journal on Applied Mathematics* 32, no. 4: 755-764.

[19] Steigmann, D.J. (1999). Fluid films with curvature elasticity. *Arch. Rational Mech. Anal.* 150, 127-152.

[20] Rawicz, W., Olbrich, K.C., McIntosh, T., Needham, D., Evans, E. (2000). Effect of chain length and unsaturation on elasticity of lipid bilayers. *Biophysical Journal* 79, no. 1: 328-339.

[21] Steigmann, D.J. (1999). On the relationship between the Cosserat and Kirchhoff-Love theories of elastic shells. *Mathematics and Mechanics of Solids*, 4(3), 275-288.

[22] Canham, P.B. (1970). The minimum energy of bending as a possible explanation of the biconcave shape of the human red blood cell. *Journal of Theoretical Biology*, 26(1), 61-81.

[23] Helfrich, W. (1973). Elastic properties of lipid bilayers: theory and possible experiments. *Z. Naturforsch* C 28, 693.

[24] Frank, F.C. (1958). I. Liquid crystals. On the theory of liquid crystals. *Discussions of the Faraday Society*, 25, 19-28.

[25] Truesdell, C., Noll, W. (2004). *The non-linear field theories of mechanics.* Springer, (pp. 1-579) Berlin Heidelberg.

[26] Agrawal, A., Steigmann, D.J. (2009). Boundary-value problems in the theory of fluid films with curvature elasticity *Continuum Mechanics and Thermodynamics*, 21, 57-82.

[27] Steigmann, D.J., Baesu, E., Rudd, R.E., Belak, J., McElfresh, M. (2003). On the variational theory of cell-membrane equilibria. *Interfaces and Free Boundaries*, 5(4), 357-366.

[28] Agrawal, A., Steigmann, D.J. (2009). Modeling protein-mediated morphology in biomembranes. *Biomechanics and modeling in mechanobiology*, 8(5), 371-379.

[29] Boal, D., Boal, D.H. (2012). *Mechanics of the Cell.* Cambridge University Press.

[30] Alberts, B., Johnson, A., Lewis, J., Raff, M., Roberts, K., Walter, P. (2002). *Molecular biology of the cell*, 4th edn. Garland Science, New York.

[31] De Camilli, P., Farsad, K. (2003). Mechanisms of membrane deformation. *Current Opinion in Cell Biology* 15, 372-381.

[32] McMahon, H.T., Gallop, J.L. (2005). Membrane curvature and mechanisms of dynamic cell membrane remodelling. *Nature* 438 590-596.

[33] Zimmerberg, J., Kozlov, M. (2006). How proteins produce cellular membrane curvature. *Nature Reviews Molecular Cell Biology* 7, 9-19.

[34] Seifert, U., Berndl, K., Lipowsky, R. (1991). Shape transformations of vesicles: Phase diagram for spontaneous-curvature and bilayer-coupling models *Physical Review A* 44.2, 1182.

[35] Ou-Yang, Z.C., Liu, J.X., Xie, Y.Z. (1999). Geometric methods in the elastic theory of membranes in liquid crystal phases. *World Scientific* Singapore.

[36] Peter, B.J., Kent, H.M., Mills, I.G., Vallis, Y., Butler, P.J., Evans, P.R., McMahon, H.T. (2004). BAR domains as sensors of membrane curvature: the amphiphysin BAR structure. *Science* 303, no. 5657: 495-499.

[37] Frost, A., Perera, R., Roux, A., Spasov, K., Destaing, O., Egelman, E.H., De Camilli, P., Unger, V.M. (2008). Structural basis of membrane invagination by F-BAR domains. *Cell* 132, 807-817.

[38] Frost, A., Unger, V.M., De Camilli, P. (2009). The BAR domain superfamily: membrane-molding macromolecules. *Cell* 137, 191-196.

[39] Shimada, A., Niwa, H., Tsujita, K., Suetsugu, S., Nitta, K., Hanawa-Suetsugu, K., Akasaka, R., Nishino, Y., Toyama, M., Chen, L., Liu, Z.J. (2007). Curved

EFC/F-BAR-domain dimers are joined end to end into a filament for membrane invagination in endocytosis. *Cell* 129, no. 4 : 761-772.

[40] Helfrich, W., Prost, J. (1988). Intrinsic bending force in anisotropic membranes made of chiral molecules. *Phys Rev A* 38, 3065-3068.

[41] Iglic, V.K., Heinrich, V., Svetina, S., Zeks, V. (1999). Free energy of closed membrane with anisotropic inclusions. *Eur. Phys. J. B* 10, 5-8.

[42] Iglic, V.K., Remskar, M., Vidmar, G., Fosnaric, M., Iglic, A. (2002). Deviatoric elasticity as a possible physical mechanism explaining collapse of inorganic micro and nanotubes. *Physics Letters A* 296, 151-155.

[43] Fosnaric, M., Bohinc, K., Gauger, D.R., Iglic, A., Kralj-Iglic, V., May, S. (2005). The influence of anisotropic membrane inclusions on curvature elastic properties of lipid membranes. *Chem Inf. Model* 45, 1652-1661.

[44] Frank, J.R., Kardar, M. (2008). Defects in nematic membranes can buckle into pseudospheres. *Physical Review E* 77.4 : 041705.

[45] Kabaso, D., Gongadze, E., Elter, P., Van Rienen, U., Gimsa, J., Kralj-Iglic, V., Iglic, A. (2011). Attachment of rod-like (BAR) proteins and membrane shape. *Mini Reviews in Medicinal Chemistry* 11, no. 4: 272.

[46] Arkhipov, A., Yin, Y., Schulten, K. (2008). Four-scale description of membrane sculpting by BAR domains. *Biophysical journal* 95, no. 6: 2806-2821.

[47] Arkhipov, A., Yin, Y., Schulten, K. (2009). Membrane-bending mechanism of amphiphysin N-BAR domains. *Biophysical journal* 97, no. 10: 2727-2735.

[48] Yin, Y., Arkhipov, A., Schulten, K. (2009). Simulations of membrane tubulation by lattices of amphiphysin N-BAR domains. *Structure* 17(6), 882-892.

[49] Ayton, G.S., Lyman, E., Voth, G.A. (2010). Hierarchical coarse-graining strategy for protein-membrane systems to access mesoscopic scales. *Faraday discussions* 144: 347-357.

[50] Cui, H., Mim, C., Vazquez, F.X., Lyman, E., Unger, V.M., Voth, G.A. (2013). Understanding the Role of Amphipathic Helices in N-BAR Domain Driven Membrane Remodeling. *Biophysical journal* 104, no. 2: 404-411.

[51] Ayton, G.S., Blood, P.D., Voth, G.A. (2007). Membrane remodeling from N-BAR domain interactions: insights from multi-scale simulation. *Biophysical journal* 92, no. 10: 3595-3602.

[52] Ramakrishnan, N., Kumar, P.S., Ipsen, J.H. (2010). Monte Carlo simulations of fluid vesicles with in-plane orientational ordering. *Phys Rev E* 81, 041922.

[53] Ramakrishnan, N., Kumar, P.S., Ipsen, J.H. (2013). Membrane-Mediated Aggregation of Curvature-Inducing Nematogens and Membrane Tubulation. *Biophysical Journal* 104, 1018-1028.

[54] Bradley, R., Radhakrishnan, R. (2013). Coarse-Grained Models for Protein-Cell Membrane Interactions. *Polymers* 5, no. 3: 890-936.

[55] Baumgart, T., Capraro, B.R., Zhu, C., Das, S.L. (2011). Thermodynamics and mechanics of membrane curvature generation and sensing by proteins and lipids. *Annual review of physical chemistry*, 62, 483.

[56] Holzapfel, G.A. (2000). *Nonlinear solid mechanics: a continuum approach for engineering*.

[57] Zheng, Q.S. (1993). Two-dimensional tensor function representation for all kinds of material symmetry. *Proc. R. Soc. London A* 443, 127-138.

[58] Capovilla, R., Guven, J. (2004). Stress and geometry of lipid vesicles. *Journal of Physics: Condensed Matter* 16, no. 22: S2187.

[59] Capovilla, R., Guven, J., Santiago, J.A. (2002). Lipid membranes with an edge. *Physical Review E* 66, no. 2: 021607.

[60] Tu, Z.C., Ou-Yang, Z.C. (2003). Lipid membranes with free edges. *Physical Review E* 68, no. 6: 061915.

[61] Muller, M.M., Deserno, M., Guven, J. (2007). Balancing torques in membrane-mediated interactions: exact results and numerical illustrations. *Physical Review E* 76, no. 1: 011921.

[62] Hu, M., Briguglio, J.J., Deserno, M. (2012). Determining the Gaussian curvature modulus of lipid membranes in simulations. *Biophysical journal* 102, no. 6: 1403-1410.

[63] Das, S.L., Jenkins, J.T., Baumgart, T. (2009). Neck geometry and shape transitions in vesicles with co-existing fluid phases: Role of Gaussian curvature stiffness versus spontaneous curvature. *Europhysics Letters* 86, no. 4: 48003.

[64] Hyman, T., Shmuel, M., Altschuler, Y. (2006). Actin is required for endocytosis at the apical surface of Madin-Darby canine kidney cells where ARF6 and clathrin regulate the actin cytoskeleton. *Molecular biology of the cell* 17(1), 427-437.

[65] Rodal, A.A., Kozubowski, L., Goode, B.L., Drubin, D.G., Hartwig, J.H. (2005). Actin and septin ultrastructures at the budding yeast cell cortex. *Molecular biology of the cell* 16(1). 372-384.

[66] Fujimoto, L.M., Roth, R., Heuser, J.E., Schmid, S.L. (2000). Actin Assembly Plays a Variable, but not Obligatory Role in Receptor Mediated Endocytosis. *Traffic* 1(2), 161-171.

[67] Mooren, O.L., Galletta, B.J., Cooper, J.A. (2012). Roles for actin assembly in endocytosis. *Biochemistry* 81(1), 661.

[68] Girao, H., Geli, M.I., Idrissi, F.Z. (2008). Actin in the endocytic pathway: from yeast to mammals. *FEBS letters* 582(14), 2112-2119.

[69] Kaksonen, M., Toret, C.P., Drubin, D.G. (2005). A modular design for the clathrin-and actin-mediated endocytosis machinery. *Cell* 123(2), 305-320.

[70] Payne, G.S., Schekman, R. (1985). A test of clathrin function in protein secretion and cell growth. *Science* 230(4729), 1009-1014.

[71] Chu, D.S., Pishvaee, B., Payne, G.S. (1996). The light chain subunit is required for clathrin function in Saccharomyces Cerevisiae. *J. Biol. Chem* 271 , 33123Ð33130.

[72] Idrissi, F.Z., Grotsch, H., Fernandez-Golbano, I.M., Presciatto-Baschong, C., Riezman, H., Geli, M.I. (2008). Distinct acto/myosin-I structures associate with endocytic profiles at the plasma membrane. *The Journal of cell biology* 180 (6), 1219-1232.

[73] Bashkirov, P.V., Chekashkina, K.V., Akimov, S.A., Kuzmin, P.I., Frolov, V.A. (2011). Variation of lipid membrane composition caused by strong bending. *Biochemistry (Moscow) Supplement Series A: Membrane and Cell Biology* 5(2), 205-211.

[74] Frolov, V.A., Escalada, A., Akimov, S.A., Shnyrova, A.V. (2014). Geometry of membrane fission. *Chemistry and Physics of Lipids*.

[75] Noguchi, H. (2013). Structure formation in binary mixtures of lipids and detergents: Self-assembly and vesicle division. *The Journal of chemical physics* 138(2), 024907.

[76] Kozlovsky, Y., Kozlov, M.M. (2003). Membrane fission: model for intermediate structures. *Biophysical journal* 85(1), 85-96.

[77] Liu, J., Kaksonen, M., Drubin, D.G., Oster, G. (2006). Endocytic vesicle scission by lipid phase boundary forces. *Proceedings of the National Academy of Sciences* 103(27), 10277-10282.

[78] Liu, J., Sun, Y., Drubin, D.G., Oster, G.F. (2009). The mechanochemistry of endocytosis. *PLoS biology* 7(9), e1000204.

[79] Agrawal, N.J., Nukpezah, J., Radhakrishnan, R. (2010). Minimal mesoscale model for protein-mediated vesiculation in clathrin-dependent endocytosis. *PLoS computational biology* 6(9), e1000926.

[80] Duwe, H.P., Kaes, J., Sackmann, E. (1990). Bending elastic moduli of lipid bilayers: modulation by solutes. *Journal de Physique* 51(10), 945-961.

[81] Faucon, J.F., Mitov, M.D., Meleard, P., Bivas, I., Bothorel, P. (1989). Bending elasticity and thermal fluctuations of lipid membranes. Theoretical and experimental requirements. *Journal de Physique* 50(17), 2389-2414.

[82] Jin, A.J., Prasad, K., Smith, P.D., Lafer, E.M., Nossal, R. (2006). Measuring the elasticity of clathrin-coated vesicles via atomic force microscopy. *Biophysical journal* 90(9), 3333-3344.

[83] Bonifacino, J.S., Schwartz, J.L. (2003). Coat proteins: shaping membrane transport. *Nature Reviews Molecular Cell Biology* 4 (5), 409-414.

[84] Gustin, M.C., Zhou, X.L., Martinac, B., Kung, C. (1988). A Mechanosensitive Ion Channel in the Yeast Plasma Membrane. *Science* New Series, Vol. 242(4879), 762-765.

[85] Finer, J.T., Simmons, R.M., Spudich, J.A. (1994). Single myosin molecule mechanics: piconewton forces and nanometre steps. *Nature* 368 (6467), 113-119.

[86] Footer, M.J., Kerssemakers, J.W.J., Theriot, J.A., Dogterom, M. (2007). Direct measurement of force generation by actin filament polymerization using an optical trap. *Proceedings of the National Academy of Sciences* 104(7), 2181-2186.

[87] Kovar, D.R., Pollard, T.D. (2004). Insertional assembly of actin filament barbed ends in association with formins produces piconewton forces. *Proceedings of the National Academy of Sciences of the United States of America* 101(41), 14725-14730.

[88] Gallop, J.L., Jao, C.C., Kent, H.M., Butler, P.J., Evans, P.R., Langen, R., McMahon, H.T. (2006). Mechanism of endophilin N-BAR domain mediated membrane curvature. *The EMBO journal* 25(12), 2898-2910.

[89] Rangamani, P., Mandadapu, K.K., Oster, G. (2014). Protein-Induced Membrane Curvature Alters Local Membrane Tension. *Biophysical Journal* 107 (3), 751-762.

[90] Lipowsky, R. (1991). The conformation of membranes. *Nature* 349 (6309), 475-481.

[91] Gourlay, C.W., Dewar, H., Warren, D.T., Costa, R., Satish, N., Ayscough, K.R. (2003). An interaction between Sla1p and Sla2p plays a role in regulating actin dynamics and endocytosis in budding yeast. *Journal of cell science* 116(12) 2551-2564.

[92] Boettner, D.R., Friesen, H., Andrews, B., Lemmon, S.K. (2011). Clathrin light chain directs endocytosis by influencing the binding of the yeast Hip1R homologue, Sla2, to F-actin. *Molecular biology of the cell* 22(19), 3699-3714.

[93] Collins, A., Warrington, A., Taylor, K.A., Svitkina, T. (2011). Structural organization of the actin cytoskeleton at sites of clathrin-mediated endocytosis. *Current Biology* 21(14), 1167-1175.

[94] Iglic, V.K., Remskar, M., Vidmar, G., Fosnaric, M., Iglic, A. (2002). Deviatoric elasticity as a possible physical mechanism explaining collapse of inorganic micro and nanotubes. *Physics Letters A* 296, 151-155.

[95] Walani, N., Torres, J., Agrawal, A. (2014). Anisotropic spontaneous curvatures in lipid membranes. *Physical Review E* 89(6), 062715.

[96] Parker, S.P. (1984). *McGraw Hill concise encyclopedia of science and technology.*

[97] Derenyi, I., Julicher, F., Prost, J. (2002). Formation and interaction of membrane tubes. *Physical review letters* 88(23), 238101.

[98] Smith, A.S., Sackmann, E., Seifert, U. (2003). Effects of a pulling force on the shape of a bound vesicle. *Europhysics Leters*, 64(2), 281-287.

[99] Sun, Y., Carroll, S., Kaksonen, M., Toshima, J.Y., Drubin, D.G. (2007). PtdIns (4, 5) P2 turnover is required for multiple stages during clathrin-and actin-dependent endocytic internalization. *The Journal of cell biology* 177(2), 355-367.

[100] Sorre, B., Callan-Jones, A., Manzi, J., Goud, B., Prost, J., Bassereau, P., Roux, A. (2012). Nature of curvature coupling of amphiphysin with membranes depends on its bound density. *Proceedings of the National Academy of Sciences* 109(1), 173-178.

[101] Hochmuth, F.M., Shao, J.Y., Dai, J., Sheetz, M.P. (1996). Deformation and flow of membrane into tethers extracted from neuronal growth cones. *Biophysical journal* 70(1): 358-369.

[102] Dai, J., Sheetz, M.P., Wan, X., Morris, C.E. (1998). Membrane tension in swelling and shrinking molluscan neurons. *The Journal of neuroscience* 18(17), 6681-6692.

[103] Park, R.J., Shen, H., Liu, L., Liu, X., Ferguson, S.M., De Camilli, P. (2013). Dynamin triple knockout cells reveal off target effects of commonly used dynamin inhibitors. *Journal of cell science* 126(22), 5305-5312.

[104] Basu, R., Munteanu, E.L., Chang, F. (2014). Role of turgor pressure in endocytosis in fission yeast. *Molecular biology of the cell* 25(5), 679-687.

[105] Ramachandran, R., Schmid, S.L. (2008). Real time detection reveals that effectors couple dynamin's GTP dependent conformational changes to the membrane. *The EMBO journal* 27(1), 27-37.

[106] Campelo, F., Kozlov, M.M. (2014). Sensing Membrane Stresses by Protein Insertions. *PLoS computational biology* 10 (4), e1003556.

[107] Engqvist-Goldstein, A.E., Drubin, D.G. (2003). Actin assembly and endocytosis: from yeast to mammals. *Annual review of cell and developmental biology* 19(1), 287-332.

[108] Kas, J., Sackmann, E. (1991). Shape transitions and shape stability of giant phospholipid vesicles in pure water induced by area-to-volume changes. *Biophysical journal*, 60(4), 825.

[109] Evans, E.A., Skalak, R., Weinbaum, S. (1980). *Mechanics and thermodynamics of biomembranes.* Boca Raton, Florida.

[110] Kummrow, M., Helfrich, W. (1991). Deformation of giant lipid vesicles by electric fields. *Physical Review A* 44(12), 8356.

[111] Seifert, U. (1997). Configurations of fluid membranes and vesicles. *Advances in physics*, 46(1), 13-137.

[112] Zhong-Can, O.Y., Helfrich, W. (1989). Bending energy of vesicle membranes: General expressions for the first, second, and third variation of the shape energy and applications to spheres and cylinders. *Physical Review A*, 39(10), 5280.

[113] Capovilla, R., Guven, J., Santiago, J.A. (2003). Deformations of the geometry of lipid vesicles. *Journal of Physics A: Mathematical and General*, 36(23), 6281.

[114] Capovilla, R., Guven, J. (2004). Second variation of the HelfrichÐCanham Hamiltonian and reparametrization invariance. *Journal of Physics A: Mathematical and General*, 37(23), 5983.

[115] Yin, Y. (2005). Integral theorems based on a new gradient operator derived from biomembranes (part I): Fundamentals. *Tsinghua Science and Technology*, 10(3), 372-375.

[116] Yin, Y. (2005). Integral theorems based on a new gradient operator derived from biomembranes (Part II): Applications. *Tsinghua Science and Technology*, 10(3), 376-380.

[117] Nelson, P., Powers, T., Seifert, U. (1995). Dynamical theory of the pearling instability in cylindrical vesicles. *Physical review letters*, 74(17), 3384.

[118] Powers, T.R., Goldstein, R.E. (1997). Pearling and pinching: propagation of Rayleigh instabilities. *Physical review letters*, 78(13), 2555.

[119] Maleki, M., Fried, E. (2013). Stability of discoidal high-density lipoprotein particles. *Soft Matter*, 9(42), 9991-9998.

[120] Li, J., Zhang, H., Qiu, F., Shi, A.C. (2013). Emergence and stability of intermediate open vesicles in disk-to-vesicle transitions. *Physical Review E*, 88(1), 012719.

[121] Walani, N., Torres, J., Agrawal, A. (2015). Endocytic proteins drive vesicle growth via instability in high membrane tension environment. *Proceedings of the National Academy of Sciences*, 112(12), E1423-E1432.

[122] Tian, A., Capraro, B.R., Esposito, C., Baumgart, T. (2009). Bending stiffness depends on curvature of ternary lipid mixture tubular membranes. *Biophysical journal*, 97(6), 1636-1646.

[123] Agrawal, A., Steigmann, D.J. (2008). Coexistent fluid-phase equilibria in biomembranes with bending elasticity. *Journal of Elasticity*, 93(1), 63-80.

[124] Steigmann, D.J., Ogden, R.W. (1999). Elastic surface-substrate interactions. *Proceedings of the Royal Society of London. Series A: Mathematical, Physical and Engineering Sciences* 455, 437-474.

[125] Givli, S., Giang, H., Bhattacharya, K. (2012). Stability of multicomponent biological membranes. *SIAM Journal on Applied Mathematics*, 72(2), 489-511.

[126] Como, M., Grimaldi, A. (1995). *Theory of stability of continuous elastic structures* (Vol. 1). CRC Press.

[127] Naghdi, P.M. (1972). The theory of plates and shells. *Handbuch der Physik* vol. VIa/2, 425-640.